

PULSED INFRARED DESORPTION OF CO₂ GUEST MOLECULES
IN AMORPHOUS SOLID WATER

by

Oscar R. Rebolledo-Mayoral

A Dissertation Presented to the
FACULTY OF THE USC GRADUATE SCHOOL
UNIVERSITY OF SOUTHERN CALIFORNIA
In Partial Fulfillment of the
Requirements for the Degree
DOCTOR OF PHILOSOPHY
(CHEMISTRY (CHEMICAL PHYSICS))

August 2011

Copyright 2011

Oscar R. Rebolledo-Mayoral

Dedication

I dedicate this dissertation to my amazing parents. To my loving mother, Alma Rosa Mayoral Villavicencio, who has shown me the value of family unity and has been the driving force throughout my life. To my late father, Eliseo Rebolledo Guinto (1952 – 2008), who was always a role-model through his hard work and dedication, and inspired me to set high goals and have the confidence to achieve them.

Acknowledgements

The USC graduate program taught me many things, two of which stand out clear in my mind: first, to always think independently, and second, that when the laser is running, 16 hour days are pretty common. All the hard work would not have been possible without the guidance, support, trust, and patience from many people. Words cannot begin to describe the enormous gratitude I have for everyone, and it is an honor to single out a few who have been instrumental in shaping me the person I am today.

I am grateful to my advisors, Hanna Reisler and Curt Wittig. Their never-ending lists of ideas and visions for the project kept me reaching for the stars at times when I doubted myself. They challenged me every day, both in the lab and in life.

In addition to my advisors, I would also like to thank the members of my dissertation committee for extending their valuable time and giving me the opportunity to present my research: Stephen Cronin, Jim Haw, Vitaly Kresin, and Chi Mak. Much appreciation goes out to the professors around SSC whose elevator talk was insightful and motivating: Alexander Benderskii, Stephen Bradforth, Anna Krylov, Armand Tanguay Jr., and Andrey Vilesov. And also to Surya Prakash for guiding me through my time as President of the CGSO advising me to have fun in everything I do.

Seeing the camaraderie between the members of our department is a unique experience I will never forget. Dr. George Kumi and Dr. Sergey Malyk were my first mentors. I came onboard when George was tucked away in his office writing his own dissertation, but his brightness and charisma still resonates in the lab today. Sergey has

been my go-to friend since day one in the lab and I am grateful for his continued support. I will always remember how terrifying my first ride on the 10 freeway was with the pchem department's motorcycle gang Jordan Fine, Sergey, and William Schroeder (all while the chamber was baking). Victoria Piunova (my early morning L.A. Marathon running partner) and Russell Sliter were the first two faces I saw at orientation. They have since both become great friends and I will forever seek their advice and support.

These words are only a tiny fraction of how grateful I am that Stephanie McKean and Jaimie Stomberg joined the team and the amount of work they both have invested in the lab, my dissertation, and me. I apologize to Jaimie for putting her to work by soldering a connector instead of giving her a tour of the lab during visitation. And apologize to Stephanie for forgetting her completely during visitation. I owe a great deal to Lee-Ann Smith-Freeman who has always looked out for me, and alerted me the moment I could move out of the tiny windowless space and into this gigantic office with her. Our venting sessions have always been cherished and are sorely missed. Thanks to everyone in the Bradforth, Reisler, Vilesov, and Wittig groups, past and present, for all the valuable discussions, ideas, and lending of tools, whether they knew it or not.

Many headaches and moments of frustration were solved by the administrative staff, especially Michele Dea. Without her guidance, I would still been either printing a poster or fighting with the binding machine. My student service advisor Katie McKissick was always cheerful at answering questions, even the hundredth time I asked which course to register post-quals. Congratulations to Heather Connor for becoming a mommy and thanks to Danielle Hayes; both preceded Katie and were extremely helpful during the

time we overlapped at USC. I do not know how Valerie Childress does it, but her lively spirit brightens my day – and a big thanks for always informing me of the water and power outages that never seem to be resolved in our building. Many thanks to the entire department and machine shop staff who were more than happy to set time aside and lend a helping hand: Jaime Avila, Thuc Do, Bruno Herreros, Ross Lewis, Frank Niertit, Corey Schultz, Phillip Sliwoski, and Don Wiggins,

Further appreciation goes out to all of my friends who read dissertation and sat through countless talks about things that made absolutely no sense. In particular Alberto Moises, Katherine Moss, and Katie Yan who thankfully reminded me to eat, sleep, and never forget who I am.

Last but not least, I want to acknowledge my life treasures, my familia. I would not be here, and I would not be who I am without them. I appreciate all their love and encouragement. They mean everything to me and I owe my success to all of them. I owe a great deal to my amá, Alma Rosa Mayoral Villavicencio, and my mijo, the late Eliseo Rebolledo Guinto. My abuelita Pancha is the glue that holds the pieces together and my tias and tios, have been there every step of the way sharing in my laughs and tears. I thank my primos, with whom I grew up and shared many adventures. Love goes out to my sister Mayra Nicté Rebolledo, my brother-in-law Eduardo Jaramillo, and my dad's greatest joys, his two grandchildren, Leon and Bruno Jaramillo Rebolledo. I am glad they both were able to meet my dad and have fond memories of him. I am grateful we are all here, together. I am blessed to have each one of you in my life, and thank you for your continued support.

Table of Contents

Dedication	ii
Acknowledgements	iii
List of Tables	viii
List of Figures	ix
Abstract	xiv
Chapter 1: Introduction	1
1.1 Ablation of Solids	2
1.2 Solid Water Substrates	4
1.3 Properties of Amorphous Ices at 90 K and Ultra-High Vacuum (UHV)	5
1.3.1 Metastable ASW	5
1.3.2 Trapping and Thermal Desorption of Icy Mixtures	8
1.4 Irradiation of Water Ices	11
1.5 Chemistry in the Interstellar Medium (ISM)	13
1.6 Thesis Overview	15
1.7 Chapter References	16
Chapter 2: Experimental Details	23
2.1 UHV System	23
2.2 Top Tier	25
2.3 Middle Tier	30
2.4 Time-of-Flight Mass Spectrometry	33
2.5 Manipulator	35
2.6 Substrate Holder	38
2.7 Substrate Preparation	42
2.8 Sample Preparation	44
2.9 Temperature Calibration	45
2.10 Nd:YAG Laser Oscillator Cavity Alignment	46
2.11 Synchronization and Triggering	48
2.12 Chapter References	51

Chapter 3: Stimulated Raman Scattering and Time-of-Flight Mass Spectrometry	53
3.1 Introduction	53
3.2 Experimental	60
3.2.1 Pulsed IR Ablation	60
3.2.2 The Raman Cell	63
3.2.3 Thin Films of ASW	65
3.3 Results and Discussion	66
3.4 Chapter References	77
Chapter 4: Amorphous Solid Water (ASW): Pulsed Ablation of ASW/CO ₂ Thin Films	79
4.1 Introduction	79
4.2 Experimental	83
4.3 Results	89
4.4 Discussion	95
4.4.1 Overview	95
4.4.2 Segregation	99
4.4.3 Material Removal	101
4.5 Summary	105
4.6 Chapter References	107
Chapter 5: Future Experiments	110
5.1 Picosecond Energy Transfer	111
5.1.1 Resonant Ablation of ASW	111
5.1.2 Vibrational Excitation of Guest Molecules	113
5.2 Experimental Strategy	117
5.3 Conclusion	122
5.4 Chapter References	124
Bibliography	126

List of Tables

Table 2.1	Peak desorption temperatures of water and guest molecules deposited at 90 K on MgO(100).	46
Table 3.1	Wavelengths and frequencies for stimulated Raman scattering of 1064 nm in D ₂ . n-order Stokes (S _n) and n-order anti-Stokes (AS _n).	62
Table 3.2	Optical properties of common window materials.	63
Table 5.1	Parameters and values used for the calculation of the threshold energy for a transient state.	113

List of Figures

- Figure 2.1 A schematic of the UHV chamber and manipulator. The manipulator and top tier are separated from tiers B and C by a gate valve. The manipulator allows for x , y , and z translation of the sample inside the chamber. 24
- Figure 2.2 Top view of tier A, equipped with an SRS RGA 300 for TPD and CaF_2 windows for transmission FTIR. The RGA cone is 7.6 cm long and can be adjusted to come within 1 mm of the substrate. 27
- Figure 2.3 Schematic drawing of tier A and FTIR setup. Plexiglass boxes house the optics outside the Nicolet Protégé 460 unit. The boxes and the unit are all purged to remove atmospheric N_2 , CO_2 , and H_2O . 28
- Figure 2.4 Tier B of the UHV chamber. The TOF mass spectrometer is offset from the center to accommodate the substrate. The desorbing molecules are ejected in the y -direction upon radiation from an incoming IR beam and enter the ionizing region. 32
- Figure 2.5 Linear time-of-flight (TOF) mass spectrometer designed by Jordan TOF Products Inc. with a 6" conflat flange. The dual plate MCP detector has an 18 mm detecting element. 34
- Figure 2.6 A schematic of the manipulator assembly and x , y and z translational stages. The hollow stainless steel rod is used as a liquid nitrogen reservoir and a copper block is silver-brazed at the end to attach the sample holder assembly. 37
- Figure 2.7 Complete sample holder assembly and heater. The assembly consists of two main copper pieces labeled A and B attached to the copper block on the manipulator. The homemade resistive heater C is cemented to the back of the copper plate D. The substrate is mounted on the copper plate, which is attached to B using a pair of screws. 40

Figure 2.8	a) A schematic representation of the oscillator cavity in a Continuum NY81C laser and the optics required for alignment of the Pockel's Cell (PC). The holder for the total reflecting mirror M1 has a diode mount on the back which the HeNe can enter and be aligned through the exit couple, M2. The polarizer, analyzer, lens paper, and white screen <u>MUST</u> be removed before Q-switching the laser. b) Maltese cross-like figure observed through the PC on the white screen.	47
Figure 2.9	Three SRS DG535 Digital Delay/Pulse Generators sharing a common 10.0 MHz timebase to drive and synchronize the 100 kHz TOF, the 100 Hz chopper wheel, and the 10 Hz Nd:YAG laser.	50
Figure 3.1	Energy level diagram for stimulated Raman scattering (SRS). Stokes (ω_S) and anti-Stokes (ω_{AS}) frequencies are generated with an initial pump (ω_p) source.	55
Figure 3.2	Geometry of TOF mass spectrometer showing the ionization, s , accelerating, d , and drift regions, D . Molecules with an initial velocity v_A and position $s = s_0 \pm \delta s_0$ cross each other at some distance along D and are detected by an MCP detector.	57
Figure 3.3	Experimental setup for stimulated Raman scattering including Raman cell and TOF-MS. 1064 nm mirrors are M1 – 2, and gold mirrors are M3 – 5 for the second Stokes (S_2 , 3424 cm^{-1}) radiation. L1 – 5 are focusing and collimating lenses. The resulting Stokes and anti-Stokes frequencies are separated by a CaF_2 prism, repetition reduced to 1 Hz by an optical chopper and ultimately the pulse is guided into the UHV chamber and aligned through the ion optics of the TOF.	60
Figure 3.4	SRS conversion efficiency of 1064 nm pulse to S_2 radiation in 61.2 atm of D_2 .	66
Figure 3.5	H_2O^+ ablation signal with 9 consecutive pulses of S_2 radiation at the same spatial location. Infrared pulse energies of 1.7 mJ (circles) and 0.7 mJ (triangles); each energy irradiates an independent area on the film. The ASW film thickness is 300 ML ($\sim 100 \text{ nm}$) at $T = 100 \text{ K}$.	68

Figure 3.6	Parameters of a plano-convex lens with focusing length f of an incoming collimated Gaussian pulse with a $(1/e)$ diameter w_i . The diameter increases to $w(z)$.	70
Figure 3.7	Temporal envelope of desorbed plume from a 400 ML ASW film irradiated with 2.3 mJ of IR energy. The major peaks are the H_2O^+ from each extraction at 100 kHz resulting in a mass spectrum every 10 μs for the duration of the plume. Spectra show the changes in the envelope after varying the distance between the substrate and a 50 cm CaF_2 focusing lens. Assuming that larger energy fluences result in molecules desorbing at earlier times, b) shows the optimum focusing distance at $47.90 + \sigma / \text{cm}$ with a) -0.15, b) 0.00, c) 0.25, and d) 0.75.	71
Figure 3.8	$(\text{H}_2\text{O})_n\text{H}^+$ cluster formation during the optimization of the focal point of S_2 radiation. Similar conditions as in Figure 3.7 but taken with $\times 4$ magnification. The larger peaks corresponding to H_2O^+ monomers are off-scale, while the smaller peaks are due to protonated water clusters showing $n = 2 - 4$ d) This spectrum shows the largest cluster intensity observed through the 3 rd extraction. Focusing distance at $47.90 + \sigma / \text{cm}$ with a) -3.00, b) -2.00, c) -0.25, d) 0.00, and e) 0.50.	73
Figure 3.9	Transformation of the temporal profile shown in Figure 3.7b to the velocity domain. The water desorption signal is from pulse 1 on a 400 ML ASW film at $T \sim 100$ K. The solid black line represents the fit with a combination of three Maxwell-Boltzmann distributions at $T = 600$ K (purple), 150 K (green), and 40 K (blue).	74
Figure 4.1	The UHV chamber is equipped with TOF-MS, FTIR, Auger, and TPD diagnostics. The TOF-MS arrangement is indicated schematically. The second Stokes line from stimulated Raman scattering in high-pressure D_2 gas (3424 cm^{-1}) excites the sample at normal incidence causing material to enter the gas phase. The electron beam (black dot) of the TOF-MS is brought to a focus 12 mm from the surface. It operates at repetition rates up to 200 kHz. Samples are irradiated in the nine areas indicated on the upper left (white squares) in order to achieve signal averaging while maintaining single-pulse conditions.	85

Figure 4.2	The TOF-MS is operating at 100 kHz, <i>i.e.</i> , spectra are recorded every 10 μ s (see Figs. 4 and 5 for individual spectra). (a) 500 ML (20% CO ₂), 1.0 mJ: The first laser pulse liberates much more CO ₂ than H ₂ O. The second laser pulse liberates comparable amounts of CO ₂ and H ₂ O. Pulse 7 liberates more H ₂ O than CO ₂ . Keep in mind that the H ₂ O:CO ₂ ratio for deposited material is 4:1. (b) 400 ML (25% CO ₂), 1.2 mJ: The same general trend as in (a) is observed, though less dramatic. (c) 400 ML of H ₂ O (<i>i.e.</i> , no CO ₂), 1.2 mJ.	91
Figure 4.3	Mass spectra obtained under single-pulse conditions (400 ML, 25% CO ₂) are presented for different IR energies. Peaks that derive from CO ₂ , monomer H ₂ O, and H ₂ O clusters are color-coded (red, blue, and black, respectively). Though some of the blue signal undoubtedly arises from H ₂ O clusters, these contributions are small. The single-pulse data shown here were obtained by summing contributions from the first three extractions (<i>i.e.</i> , mass spectra) for each of the squares indicated in Figure 4.1.	92
Figure 4.4	This spectrum highlights the presence of protonated water cluster ions. Note that the H ₂ O ⁺ and CO ₂ ⁺ peaks are off-scale. Conditions: 400 ML (25% CO ₂), 2.4 mJ, average of 9 spots, 3 extractions for each spot.	94
Figure 4.5	On rare occasions, large cluster signals are observed, <i>e.g.</i> , compare this single-shot spectrum to the one in Figure 4.4. The sample is 400 ML of ASW (<i>i.e.</i> , no CO ₂). The IR energy is 1.7 mJ.	100
Figure 4.6	The data from Figure 4.2b, pulse 1 were converted from the time domain to the (on axis) velocity domain using the standard time-to-velocity Jacobian. Ablated CO ₂ clearly travels more slowly than H ₂ O.	104
Figure 5.1	Experimental diagram of mode-locked Nd:YAG system for stimulated Raman scattering and second harmonic generation. For complete details of the optics for SRS refer to Figure 3.3 in Chapter 3. The fundamental is guided to a high-pressure Raman cell filled with D ₂ . Resulting Stokes and anti-Stokes are separated to isolate	118

S_2 (3424 cm^{-1}) and reduce its repetition rate to. Similarly, the frequency doubled pulse is guided to the optical chopper and its repetition reduced. S_2 and 532 nm at 1 Hz repetition rate are guided into the UHV chamber.

Figure 5.2 Representation of ASW doped with CO_2 (red dots) and NO_2 (yellow triangles) on a $\text{MgO}(100)$ substrate for the study of a) fast heat transfer with picosecond pulsed laser ablation with matrix-resonant second Stokes, S_2 ($\nu = 3424\text{ cm}^{-1}$), and guest-resonant visible (532 nm) pulses; b) segregation of guest molecules and “lift-off” of planar C_6H_6 on top of ASW film through induced phase explosions; c) depth-profiling and diffusion of C_6H_6 across the surface with consecutive pulses. Black arrows are used to denote uncertainty as to which method of ablation is best for the task.

120

Abstract

The trapping and release of CO₂ from thin films of amorphous solid water (ASW), < 500 monolayers (ML), were investigated by irradiating vapor-deposited ASW/CO₂ mixtures with pulsed 3424 cm⁻¹ infrared radiation and detecting the ejected molecules using time-of-flight mass spectrometry (TOF-MS). The studies were concerned with the preferential removal of CO₂ over H₂O after consecutive low energy radiation pulses (< 1.2 mJ/pulse), and the ejection of water aggregates with high energy pulses (> 1.2 mJ/pulse) which were ionized to protonated water clusters of the form (H₂O)_nH⁺ with $n = 1 - 6$.

Amorphous solid mixtures of ASW/CO₂ with typical composition ratios of 3:1 or 4:1 (H₂O:CO₂) were prepared by co-depositing CO₂ during ASW formation on a MgO(100) substrate. Porous ASW was formed by dosing the MgO substrate with gaseous H₂O at 90 K under ultra-high vacuum conditions. CO₂ multilayers that formed atop the ASW/CO₂ film were removed by annealing the film to ~ 112 K and returning it to 90 K. Ablation was achieved through vibrational excitation of the asymmetric stretch of H₂O molecules in the ice film. The 3424 cm⁻¹ light was generated by optimizing the second Stokes component in the stimulated Raman scattering (SRS) of 1064 nm radiation from a Nd:YAG laser (10 ns pulses) in D₂ ($\nu = 2987$ cm⁻¹). The overall quantum Raman conversion efficiency of ~ 4% was obtained.

Single-pulse irradiation of ASW and H₂O/CO₂ amorphous mixtures resulted in the ejection of both species with high translational energies. The rapid temperature

increase after irradiation facilitates CO₂ removal via evaporation prior to segregation of CO₂. The high thermal conductivity of the crystalline substrate quenches the heterogeneous nucleation of cavities that take place near the substrate. The presence of small protonated water clusters is interpreted as evidence for trivial fragmentation occurring near the surface of the film.

Despite the significant energy transfer to the substrate, near complete removal of CO₂ has been measured through consecutive pulses incident on the same location at the film's surface. CO₂ removal occurred in as few as 6 pulses, whereas only 10 – 20 ML of H₂O were removed per pulse. The ability of the ice to trap CO₂ changes after each pulse. Whereas the first pulse irradiates an amorphous film, consecutive irradiation of film can induce irreversible changes to the morphology of the irradiated volume thereby inducing partial crystallization.

Future experiments are aimed at exploring guest-host interactions after irradiation, where energy deposition occurs in less time than the characteristic time for thermal transfer to the substrate. Studies where transport and segregation of dopants play a pivotal role in the enhancement of phase explosions and where the energetic release of aggregates through morphology changes is exploited to achieve lift-off of large surface-bound species are also outlined.

Chapter 1: Introduction

The characteristics of material ablation and desorption studied by the application of intense, pulsed electromagnetic radiation are relevant various fields of chemistry, physics, astrophysics, and medicine [1-4]. Explanations for the disintegration of condensed matter are complex, often involving mechanical phenomena as well as thermodynamic processes of phase transitions. The principle behind interactions of photons with an amorphous solid water matrix to induce the release of trapped gaseous molecules is the subject of this thesis. The primary motivation for this work has been to understand desorption processes in nanometer-sized “thin” films of water ice, primarily those doped with CO₂, after irradiating them with infrared radiation derived from a pulsed laser source and resonant with the ice absorption. A comparison is made with previously known results from the photo-desorption of micrometer-sized “thick” films of water ice [5-7].

To put the chemistry and physics studies in context, it is important to introduce several concepts of material ablation that are relevant to this work. Following this, a history of the applications of material removal through thermal desorption processes, and the contributions of these studies to understanding the desorption mechanisms is presented. Then an overview of the studied systems and methods will be put forth. Though we are not astronomers, astrophysicists, or belonging to the new emerging breed of astrochemists, a concise description of the relevance of this work to events taking place in outer space and the Interstellar Medium (ISM) will be included as well.

1.1 Ablation of Solids

Material removal through the ablation of solids with intense radiation has been studied to a great extent experimentally [8-10] and theoretically [11-16]. Much work has been devoted to silicon because of its applications in the materials and technology sector. Medicine and analytical chemistry have had their share of investigations in material removal because of its applications in the controlled removal of tissue [3] and mass spectrometry of large organic molecules that would otherwise decompose upon evaporation [2].

With the introduction of ultra-violet matrix-assisted laser desorption ionization (UV-MALDI) by Karas and Hillenkamp [17-19] in the 1980s, a dramatic increase in the available mass range and possible resolution of mass spectrometry has been achieved [20]. Despite the developments in the last few decades of UV-MALDI, the mechanism for desorption and ionization is still a subject of debate [19, 21, 22]. In the 1990s Overberg *et al.* reported the first results of desorption of ionized molecules by using an infrared laser source rather than the more common UV source in MALDI experiments (IR-MALDI) [23]. This method uses laser irradiation tuned to a vibrational frequency of the host matrix, often tuned the OH vibration band at $\sim 3 \mu\text{m}$ for matrices such as glycerol, organic acids, and water [24-26]. More recently, a derivative of IR-MALDI, resonant-infrared matrix-assisted pulsed laser evaporation (RIR-MAPLE) for thin-film production of organic and polymeric materials, has been developed [27]. The excitation from the infrared pulse is followed by decomposition of the solid target and ejection of material. With the absence of a UV photon, the chemical and physical

structures of the molecules are preserved and the ejection of molecules follows a thermal pathway as opposed to non-thermal electronic excitations. IR-MALDI is generally regarded as a softer desorption method that leads to a low degree of ion fragmentation. Hence, bigger molecules can be analyzed.

Models that describe the underlying processes of the ejection of molecules from solid surfaces through the gas-solid interface have highlighted the effect of laser fluence and pulse width on desorption; secondary effects such as collisions and thermal relaxation are often mentioned, but only briefly discussed [13, 16, 19, 21, 22]. Zhigilei and Garrison have predicted the existence of laser fluence thresholds for the onset of desorption and ablation of organic solids irradiated by a 150 ps laser pulse at 337 nm by using molecular dynamic simulations [28, 29]. At low energy fluences, monomers desorb and the yield of ejected molecules has an Arrhenius-type dependence on the laser fluence. Energy deposited at high fluences goes into the internal energy of the molecules, the translational energy of the ejected plume, and the energy of the pressure wave that propagates into the sample. This pressure wave eventually leads to the ejection of large fragments of material [29, 30]. In this case, ablation occurs in an explosive vaporization of the overheated material.

Similarly, ablation experiments of silicon materials by Yoo *et al.* with high irradiance ($> 10^{10}$ W cm⁻²) showed the existence of a fluence threshold [31]. Modifications to Zhigilei's model had to be made due to a change in the optical properties of silicon upon melting. The liquid becomes almost transparent to the incident radiation when heated just below its critical state. Yet another example of a fluence

threshold is seen with ionic crystals such as CaF_2 when irradiated by a 248 nm laser pulse with 14 ns width [32]. The fluence threshold was observed to be 2 – 4 times greater than the well-defined value of 10 J cm^{-2} for the onset of plasma formation for this polished crystal. The rise in absorbed energy was attributed to a large level of defects favoring melting at the upper edges of the surface steps over ablation.

All of the mentioned studies above exhibit a laser fluence threshold regardless of their material composition. These studies suggest that the fundamental physical processes underlying the ablation phenomena are dependent on the amount of stress on the system induced by the deposition and removal of energy. To further understand these processes, we turn to another system: amorphous solid water (ASW).

1.2 Solid Water Substrates

Water is the most important compound for the sustainability of life as we know it. The ability to form hydrogen bond networks makes water the exception to almost every trend and its interactions with other molecules are complex. Properties that depend on a hydrogen bond network include unusually high viscosity, high boiling and melting points, etc. [33]. It also displays multiple phases and morphologies, and the transformations between them are not well understood. With water being the most studied molecule in science, there are still many questions to be answered. Even simple everyday processes such as the freezing of water prove to be rather complex, as molecular dynamic simulations have shown [34, 35]. Properties of condensed phases of water, such as density, have been attributed not only to hydrogen bonding, but have also

been connected to the spatial arrangement of the molecules [36]. Since the discovery of the polymorphism of crystalline ice by Tammann in 1900 [37, 38] and the beginnings of its theoretical modeling in 1969 by Barker *et al.* [39], at least 15 crystalline forms of solid water have become known, as well as several amorphous ones.

Amorphous solid water (ASW) has gained particular interest as an important model system for heterogeneous interactions in the atmosphere and the Universe [40-45]. For example, the formation of cage-like structures, also known as clathrates, leads to confinement of small molecules and is a major source of entrapment for greenhouse gasses [46, 47]. Observations show that ASW is the most abundant type of ice in the interstellar medium (ISM) [48]. It is a major constituent of comets, interstellar clouds, planetary rings, and dust grains [49-51]. Examining interactions between ASW and an adsorbate, such as the adsorption and desorption of molecules trapped in ASW, can shed light on building a more quantitative model of macroscopic processes. Photochemistry of mixed ices of H₂O and CO, CH₃OH, HCOOH, CH₄, H₂CO, or CO₂ [52-55] using high energy particles (from UV photons to MeV particles) leads to chemical reactions and the ejection of the synthesized molecules. This encompasses only a fraction of the applications of ASW as a host.

1.3 Properties of Amorphous Ices at 90 K and Ultra-High Vacuum (UHV)

1.3.1 Metastable ASW

The amorphous forms of solid water appear to have some extraordinary properties. They are highly dependent on the conditions under which they were grown.

The structure is mainly sensitive to temperature and pressure during formation, and also to the methods used for sample preparation [56-58]. Amorphous materials do not possess long range order with respect to the position of their constituents, and surface diffusion of ASW that can lead to a more ordered state is small on the experimental timescale. The solid resembles a snapshot in time of the liquid structure. For these reasons, ASW has been used as a model for liquid water and supercooled liquids [41, 59, 60].

All amorphous materials are metastable. ASW is metastable with respect to its crystalline phase because it is not the most thermodynamically stable phase under the same conditions [40, 61]. Under ultra-high vacuum (UHV) conditions of 10^{-10} Torr growth of three phases of water are observed: ASW, cubic ice (CI), and hexagonal ice (HI) [62]. HI arises from the cooling of liquid water whereas CI is produced by heating ASW to ~ 160 K. Focus is kept in this thesis on vapor-deposited ASW, with some discussion concerning CI.

In 1935, Burton *et al.* first identified vapor-deposited ASW at a temperature of ~ 100 K [56]. The term ASW does not encompass the complexity of this form of this molecular solid and, therefore, an expanded nomenclature is used. Therefore, an expanded nomenclature is used. Physical properties of ASW, such as density and porosity, vary tremendously with preparation method and have proven useful in classifying the type of ice present. For example: high pressure amorphization of crystalline ice forms a high density amorphous (HDA) solid water [63]; heating HDA to 130 K produces a low density amorphous (LDA) solid water [44, 64]; liquid water droplets having been quenched at high rates ($\sim 10^6$ K s^{-1}) to 77 K form hyperquenched

glassy water (HGW) [60]; further amorphization of HDA forms very high density amorphous (VHDA) solid water [65]. Neutron diffraction studies by Finney *et al.* show that the density of VHDA is 1.25 g cm^{-3} , in comparison to 1.17 g cm^{-3} for HDA and 0.93 g cm^{-3} for LDA [66]. Ayotte *et al.* show that the degree of porosity of a vapor-deposited ASW increases with decreasing deposition temperature [64]. Vapor-deposition below 20 K forms a porous ASW (p-ASW) whereas in the range of 80 – 120 K, such as Burton's ASW, a compact ASW (c-ASW) is formed. The term ASW will be used for vapor-deposited water as the method of preparation.

The heating of p-ASW irreversibly transforms it into c-ASW in the temperature range 30 – 80 K, when forming p-ASW at temperatures below 38 K. c-ASW eventually undergoes an exothermic transition into CI at $T \sim 140 \text{ K}$ with negligible density change. Diffraction patterns of CI show a diamond-type cubic structure, suggesting higher stability than both p-ASW and c-ASW. Although CI displays a single phase, it is still metastable compared to the more thermodynamically stable HI [62].

Crystallization of ASW has been experimentally observed to occur between 140 and 170 K when heating ASW slowly at a typical rate of 2 K s^{-1} [57, 59, 67-69]. The transition occurs through homogeneous nucleation of crystallites, though the nature and rate of grain growth is unclear [57, 70, 71]. The activation energy for crystallization of ASW has been reported to vary from 44 kJ mol^{-1} [72] to 70 kJ mol^{-1} [70, 71], with variations attributed to substrate effects [71, 73] or preparation methods [74]. The crystallization rate has been observed to increase when ASW films are grown on a crystalline substrate [71, 73]. It was concluded that the substrate acted as a nucleation

site for crystal growth through observation of decreasing crystallization rate with increasing distance from the substrate.

Thermal dissipation through ASW can also affect the rate of crystallization. The structural disorder of the amorphous phase affects thermal conductivity, which in turn affects crystal growth. Thermal conduction is the propagation of low frequency vibrations, i.e. phonon scattering. The porosity of the amorphous material changes the mean free path for phonon scattering and hence thermal conductivity. The conductivity of p-ASW is reported to be smaller by a factor of 10 than that of c-ASW, where phonon scattering in c-ASW displays crystal-like behavior [75]. Nanometer thick ASW films grown at 90 K have shown to have sufficient porosity to trap material and thin enough to reduce long range effects on its thermal conductivity [76, 77].

1.3.2 Trapping and Thermal Desorption of Icy Mixtures

The ability of ASW to adsorb and trap a variety of volatile compounds has been attributed to its porosity [58, 76, 77]. McMillan and Los observed that ASW is relatively porous and exothermically anneals upon heating [78]. A description of the cavities has been given by Kimmel *et al.* who proposed that the cavities are linked together and open to the outer surface of the solid, allowing volatile compounds to enter the solid and eventually get trapped [58]. The incidence angle of the molecular-beam deposition of water on a cold substrate under UHV conditions was varied to study its effects on the morphology of the film. In this study, the degree of porosity of ASW was increased from a low-porosity solid at normal incidence to highly-porous at large angle of incidence of

the molecular beam. In the background deposition technique, used to form p-ASW and c-ASW as discussed earlier, the porosity increased as the deposition temperature decreased [79]. It was found that porous films are able to adsorb between 20 and 50 times more volatile compounds than compact films [64]. With the understanding that the adsorption of gasses in ice films is dramatically affected by their structure, it is clear that when different amorphous structures are generated, their ability to trap volatile compounds would depend upon their morphology.

Many volatile species are able to fill the cavities in the film formed through vapor-deposition techniques. The residence time for physisorbed molecules depends on the van der Waals interaction with the hydroxyl groups of the cavity walls. Desorption of trapped species has been measured by temperature programmed desorption (TPD), which provides a direct measure of desorption energies and can be used to describe the film's composition and gas-ASW interactions. The general consensus is that gas not liberated from ASW upon annealing is locked in the ice until its transition into cubic ice [64, 76, 77, 79, 80]. During this fast and exothermic transition the ice matrix becomes temporarily loose and abruptly releases a major fraction of the trapped gas. This fast release is referred to as a "molecular volcano." However, a small fraction of the gas remains trapped. The liberation of this remaining gas is delayed until the temperature reaches a point where the ice co-desorbs with any remaining gas still trapped in the host matrix.

Thermal desorption experiments have established general trends in the sublimation of icy mixtures. The release of O₂ trapped in ASW at 77 K was observed by

Ghormley to occur at approximately 95 K, 160 K, and 214 K [81]. Less than two decades later, Bar-Nun *et al.* studied the desorption of various molecules trapped at 24 – 100 K [82, 83]. It was observed that molecules such as HCN, NH₃, CO₂, and CH₄ are trapped more efficiently than CO, Ar, Kr, and Xe and that the trapping efficiency of each gas drops exponentially with increasing temperature. Gas release was found to occur within several temperature ranges, which indicates the presence of distinct adsorption sites [83]. Yet two decades later, Collins *et al.* used ASW on silicon grains at approximately 30 K to mimic astrophysical environments which showed similar desorption mechanisms for N₂, O₂, and CO [84]. The lack of a molecular volcano peak for NH₃, CH₃OH, and HCOOH in this study suggests that these molecules are unable to diffuse through the fractures and so resided on the surface or remained trapped in the solid as gas or co-crystals until their co-desorption.

Ayotte *et al.* suggested that guest-molecules not ejected through the ASW-CI transition might be trapped in clathrate-hydrate cages [64]. Greenhouse gasses trapped in clathrates are more commonly studied by the atmospheric community [85-87]. Devlin *et al.* reported a theoretical study on the formation of clathrates at low temperatures, 100 – 150 K, in contrast to “normal” clathrate formation temperatures of >200 K [88]. Unlike normal clathrates, in which the trapped molecule has minimal interaction with the surrounding cage, this study focused on guest molecules capable of hydrogen bonding. Clathrate formation under UHV conditions for other non-hydrogen-bonding guest molecules were reported by Bar-Nun *et al.* where ~ 5 μm thick films were slowly deposited over 7 hours [89]. To effectively trap an individual guest in a cage, the

concentration of the guest was kept low, and slow dosing allowed for its enclosure.

Although clathrate formation under these conditions is unlikely the idea is not dismissed.

1.4 Irradiation of Water Ices

Processes that occur in and on ices such as desorption, surface and bulk diffusion, segregation of adsorbed species, and phase changes can be related to the relaxation and heat transport properties of the ice [41, 62, 90, 91]. These processes in water ices can be studied by rapid heat transfer using pulsed irradiation. Photon-driven studies of these processes in water ices typically rely on desorption following UV radiation (mainly Lyman- α 121.6 nm) [53-55]. They have shown that the dissociation of water molecules, results in desorption of H, O, and OH, and also recombination products, such as H₂, H₂O, HO₂, and H₂O₂. A complementary strategy for energy desorption is the specific targeting of vibrational excitations of water ice with infrared radiation. The vibrational excitation turns into heat on a picosecond time-scale and promotes desorption of water molecules and trapped guest molecules [92, 93].

The desorption yield for crystalline ice films was measured by George's group following irradiation in the wavelength range of 2.8 – 3.4 μm [5]. The method was called "laser resonant desorption" (LRD) and a maximum desorption at $\lambda \sim 3 \mu\text{m}$ was found. Depth-profiling and diffusion measurements were carried out to determine the amount of material removed by a focused laser pulse and to determine the rates of molecular motion on and through the ice [5-7]. LRD studies of micrometer sized films carried out by Livingston *et al.* using an Er:YAG laser, $\lambda = 2.94 \mu\text{m}$, showed a well defined depth-

profile of $\sim 0.5 \mu\text{m}$ per pulse using consecutive laser pulses [6]. Further investigations used LRD to study the surface and bulk diffusion of Na, HCl, NH_3 , CH_3OH , SO_2 , C_4H_{10} [7, 94, 95]. To study surface diffusion of a guest molecule across the host film, prepare-refill-probe experiments with the guest molecules on top of the film were conducted. In these experiments, LRD releases molecules from a region on top the film and guest molecules diffuse across the surface to refill the region. After a time delay, a second pulse probes the same location. For bulk diffusion, $\text{H}_2\text{O}:\text{guest}:\text{H}_2\text{O}$ sandwich structures were prepared and, together with depth-profiling analysis by LRD, the guest molecule diffusion was measured using consecutive laser pulses. Results showed LRD to be an efficient tool for the study of these processes on ice surfaces.

Understanding the desorption mechanisms initiated by the irradiation of ices with infrared radiation adds a level of detail not found in earlier desorption studies with TPD and opens up investigations regarding morphological changes and molecular transport across complex interfaces. Typical issues are: How does the disruption of the hydrogen bond network caused by infrared laser heating affect the morphology of ASW? What are the pathways for energy transfer and how do they affect desorption? What is the composition of the desorbed material? How is molecular transport affected in a metastable solid with trapped molecules? Material desorption depends on laser fluence, pulse length, and matrix composition as has been seen with metallic and ionic solids [1]. These are different than ice but the findings and models can give an insight for a better understanding of the desorption of ASW.

1.5 Chemistry in the Interstellar Medium (ISM)

The chemistry community has made significant contributions to the astrophysics and astronomy fields. Recent observations of molecules in astrophysical environments find them in the gas phase, as molecular ices, or trapped in these ices [4, 51, 96-102]. These ices are also subjected to impact of energetic photons and particles that may induce chemical reactions leading to the formation more complex molecules. Planets and stars have been estimated to occupy no more than $\sim 10^{-8}$ % of the total volume in the Milky Way galaxy [4, 51, 96]. The region in between these bodies is called the Interstellar Medium (ISM) and it contains a mixture of dust grains and gas clouds rich in atomic and molecular species. These dust grain nanoparticles make up ~ 1 % of the total mass of the ISM and the maximum density of the densest of molecular clouds is only $\sim 10^9 \text{ m}^{-3}$. It is in the ISM where stars are born and where material returns at the end of a star's life.

To date, over 140 molecules have been detected in the ISM with more than half being composed of only 4 atoms or less [103]. The most prevalent molecule is H_2 , at abundances up to 10^4 with respect to the next most abundant molecule, H_2O . Conditions are sufficiently harsh that possible reactions are limited. For example, in a region near the start of star formation, the temperature can rise in excess of 100 K. Lower density regions, i.e. diffuse clouds, have a density of $\sim 3 \times 10^7 \text{ m}^{-3}$ and typical temperatures in the range of 80 – 100 K [51]. Lower temperatures of 10 – 50 K are found in higher density molecular clouds. Reactions at surfaces, simulating processes in interstellar dust grains, have been the primary target for laboratory investigations aimed at understanding the origin of molecules observed in the ISM [52, 55, 97, 104].

In 1930, Trumpler was credited for the identification of dust in the ISM through his observations of dark regions, leading to the conclusion that light emanating from stars was being absorbed or scattered by matter [105]. In H, C, N and O-rich areas, surface reactions generate a coat on these grains, mainly made of H₂O ice (~ 68 %) [51]. During the growth phase of the ice, other species are formed through surface reactions and these coat the grain or become trapped in the ice. The molecules include CO₂, CH₄, NH₃, CO, and CH₃OH [106-109]. The grain mantles are subject to photon and particle bombardment throughout their evolution. UV radiation and proton bombardment of ices and their mixtures can lead to the formation of new species through molecular dissociation. Heat generated in regions of star formation can lead to further surface chemistry and sublimation of ices and their products through changes in morphology.

There is great interest in trying to understand the formation of the larger, more complex molecules observed in molecular clouds of the ISM that may have been synthesized through photon irradiation [45, 52, 104, 110, 111]. Aside from mechanism of synthesis, some fundamental questions are: How are these larger molecules transferred into the gas phase? How is heat transfer through the ice involved in the mobility and eventually the ejection of gas molecules? The study of these molecules, their formation and evolution under interstellar conditions, along with their involvement in processes such as star formation, forms the basis of the relatively new field of astrochemistry.

1.6 Thesis Overview

The research in this thesis describes the incorporation of an IR radiation source and a time-of-flight (TOF) mass spectrometer to the previously existing experimental setup. The experiments described here are aimed at investigating the desorption of CO₂ from nanometer-sized thin films of ASW in order to:

- (1) define the desorption processes of guest and host molecules from thin icy surfaces using focused infrared radiation pulses;
- (2) assess the effectiveness of CO₂ as a probe for ice morphology;
- (3) set the stage for future experiments that will to explore energy flow between guest-host and host-substrate interfaces through direct excitation of the guest molecule resulting in fast energy deposition.

In Chapter 2, the experimental methods and procedures are described. Chapter 3 will explore the method for the generation of 3424 cm⁻¹ radiation to induce resonant-mediated ablation, along with the implementation of a time-of-flight mass spectrometer as a detection device for ablated material. The experimental results for desorption from thin films of ASW doped with CO₂ are discussed in Chapter 4. Chapter 5 explores the use of fast energy deposition as the basis for future work.

1.7 Chapter References

1. C. R. Phipps, *Laser Ablation and its Applications*: Springer Science+Business Media LLC (2007).
2. *Methods and Mechanisms for Producing Ions from Large Molecules*. NATO ASI Series, ed. K.G. Standing and W. Ens. Vol. 269. New York: Plenum Press (1991).
3. *Proceedings of Laser-Tissue Interaction VIII*, ed. S.L. Jacques. Vol. 2975: SPIE Proceedings Series (1997).
4. A. G. G. M. Tielens, *The Physics and Chemistry of the Interstellar Medium*. 1st ed. The Graduate Series in Astronomy. Cambridge: Cambridge University Press (2001).
5. A. Krasnopoler and S. M. George, *Journal of Physical Chemistry B*. 102, 788-794 (1998).
6. F. E. Livingston, J. A. Smith, and S. M. George, *Analytical Chemistry*. 72, 5590-5599 (2000).
7. F. E. Livingston, J. A. Smith, and S. M. George, *Journal of Physical Chemistry A*. 106, 6309-6318 (2002).
8. A. Cavalleri, K. Sokolowski-Tinten, J. Bialkowski, M. Schreiner, *et al.*, *Journal of Applied Physics*. 85, 3301-3309 (1999).
9. K. Sokolowski-Tinten, J. Bialkowski, A. Cavalleri, and D. von der Linde, *Ultrafast Phenomena Xi*. 63, 316-318 (1998).
10. D. von der Linde and K. Sokolowski-Tinten, *Applied Surface Science*. 154, 1-10 (2000).
11. D. S. Ivanov and L. V. Zhigilei, *Physical Review Letters*. 91, 105701 (2003).
12. L. J. Lewis and D. Perez, *Applied Surface Science*. 255, 5101-5106 (2009).
13. P. Lorazo, L. J. Lewis, and M. Meunier, *Physical Review B*. 73, 134108 (2006).
14. D. Perez and L. J. Lewis, *Physical Review Letters*. 89, 255504 (2002).
15. D. Perez, L. J. Lewis, P. Lorazo, and M. Meunier, *Applied Physics Letters*. 89, 141907 (2006).

16. L. V. Zhigilei, *Applied Physics a-Materials Science & Processing*. 76, 339-350 (2003).
17. M. Karas, D. Bachmann, U. Bahr, and F. Hillenkamp, *International Journal of Mass Spectrometry and Ion Processes*. 78, 53-68 (1987).
18. M. Karas, D. Bachmann, and F. Hillenkamp, *Analytical Chemistry*. 57, 2935-2939 (1985).
19. M. Karas and R. Kruger, *Chemical Reviews*. 103, 427-439 (2003).
20. M. Karas, *Fundamental Processes in Sputtering of Atoms and Molecules (SPUT 92)*, ed. P. Sigmund. Vol. p 623. Copenhagen: Det Kongelige Danske Videnskabernes Selskab (1993).
21. K. Dreisewerd, *Chemical Reviews*. 103, 395-425 (2003).
22. R. Knochenmuss and R. Zenobi, *Chemical Reviews*. 103, 441-452 (2003).
23. E. Nordhoff, A. Ingendoh, R. Cramer, A. Overberg, *et al.*, *Rapid Communications in Mass Spectrometry*. 6, 771-776 (1992).
24. S. Berkenkamp, M. Karas, and F. Hillenkamp, *Proceedings of the National Academy of Sciences of the United States of America*. 93, 7003-7007 (1996).
25. C. Menzel, K. Dreisewerd, S. Berkenkamp, and F. Hillenkamp, *International Journal of Mass Spectrometry*. 207, 73-96 (2001).
26. R. W. Nelson, R. M. Thomas, and P. Williams, *Rapid Communications in Mass Spectrometry*. 4, 348-351 (1990).
27. B. Toftmann, M. R. Papantonakis, R. C. Y. Auyeung, W. Kim, *et al.*, *Thin Solid Films*. 453-54, 177-181 (2004).
28. L. V. Zhigilei and B. J. Garrison, *Applied Physics Letters*. 74, 1341-1343 (1999).
29. L. V. Zhigilei, P. B. S. Kodali, and B. J. Garrison, *Journal of Physical Chemistry B*. 102, 2845-2853 (1998).
30. C. Mihesan, M. Ziskind, B. Chazallon, C. Focsa, *et al.*, *Applied Surface Science*. 248, 238-242 (2005).
31. J. H. Yoo, S. H. Jeong, R. Greif, and R. E. Russo, *Journal of Applied Physics*. 88, 1638-1649 (2000).

32. S. Gogoll, E. Stenzel, M. Reichling, H. Johansen, *et al.*, *Applied Surface Science*. 96-8, 332-340 (1996).
33. M. Chaplin. *Water Structure and Science*. 2011; Available from: <http://www.lsbu.ac.uk/water/>.
34. V. Buch and J. P. Devlin, Introduction, In *Water in Confining Geometries*, V. Buch and J.P. Devlin, Eds.; Springer: Berlin (2003).
35. M. Matsumoto, S. Saito, and I. Ohmine, *Nature*. 416, 409–413 (2002).
36. K. Rottger, A. Endriss, J. Ihringer, S. Doyle, *et al.*, *Acta Crystallographica Section B-Structural Science*. 50, 644-648 (1994).
37. G. Tammann, *Annalen Der Physik*. 3, 161-194 (1900).
38. G. Tammann, *Annalen Der Physik*. 2, 1-31 (1900).
39. J. A. Barker and R. O. Watts, *Chemical Physics Letters*. 3, 144-145 (1969).
40. C. A. Angell, *Science*. 267, 1924-1935 (1995).
41. C. A. Angell, *Annual Review of Physical Chemistry*. 55, 559-583 (2004).
42. L. J. Allamandola, S. A. Sandford, A. G. G. M. Tielens, and T. M. Herbst, *Astrophysical Journal*. 399, 134-146 (1992).
43. S. A. Sandford and L. J. Allamandola, *Journal of Astrophysics*. 355, 357-372 (1990).
44. K. P. Stevenson, G. A. Kimmel, Z. Dohnalek, R. S. Smith, *et al.*, *Science*. 283, 1505-1507 (1999).
45. L. J. Allamandola, S. A. Sandford, and G. J. Valero, *Icarus*. 76, 225-252 (1988).
46. P. Dornan, S. Alavi, and T. K. Woo, *The Journal of Chemical Physics*. 127, 124510 (2007).
47. E. D. Sloan, *Nature*. 426, 353-359 (2003).
48. E. F. van Dishoeck, *Annual Review of Astronomy & Astrophysics*. 42, 119-167 (2004).

49. P. Jenniskens and D. F. Blake, *Science*. 265, 753 (1994).
50. R. Smoluchowski, *Science*. 201, 809-811 (1978).
51. *Dust and Chemistry in Astronomy*. The Graduate Series in Astronomy, ed. T.J. Millar and D.A. Williams. Bristol: Institute of Physics Publishing (1993).
52. K. I. Oberg, R. T. Garrod, E. F. van Dishoeck, and H. Linnartz, *Astronomy & Astrophysics*. 504, 891-U828 (2009).
53. K. I. Oberg, H. Linnartz, R. Visser, and E. F. van Dishoeck, *Astrophysical Journal*. 693, 1209-1218 (2009).
54. K. I. Oberg, E. F. van Dishoeck, and H. Linnartz, *Astronomy & Astrophysics*. 496, 281-293 (2009).
55. M. S. Westley, R. A. Baragiola, R. E. Johnson, and G. A. Baratta, *Nature*. 373, 405-407 (1995).
56. E. F. Burton and W. F. Oliver, *Proceedings Royal Society*. A153, 166-172 (1935).
57. P. Jenniskens, S. F. Banham, D. F. Blake, and M. R. S. McCoustra, *Journal of Chemical Physics*. 107, 1232-1241 (1997).
58. G. A. Kimmel, N. G. Petrik, Z. Dohnalek, and B. D. Kay, *Physical Review Letters*. 95, 166102 (2005).
59. C. A. Angell, *Annual Review of Physical Chemistry*. 34, 593-630 (1983).
60. G. P. Johari, A. Hallbrucker, and E. Mayer, *Nature*. 330, 552-553 (1987).
61. M. G. Seats and S. A. Rice, *Amorphous Solid Water and Its Relationship to Liquid Water: A Random Network Model for Water*, In *Water: A comprehensive treatise*, F. Franks, Ed.; Plenum Press: New York (1982).
62. P. V. Hobbs, *Ice Physics*. Oxford: Clarendon Press (1974).
63. G. P. Johari and O. Andersson, *Thermochimica Acta*. 461, 14-43 (2007).
64. P. Ayotte, R. S. Smith, K. P. Stevenson, Z. Dohnalek, *et al.*, *Journal of Geophysical Research-Planets*. 106, 33387-33392 (2001).
65. N. Giovambattista, H. E. Stanley, and F. Sciortino, *Physical Review E*. 72, 031510 (2005).

66. J. L. Finney, A. Hallbrucker, I. Kohl, A. K. Soper, *et al.*, *Physical Review Letters*. 88, 225503 (2002).
67. D. Laufer, E. Kochavi, and A. Barnun, *Physical Review B*. 36, 9219-9227 (1987).
68. R. A. Baragiola, Microporous Amorphous Water Ice Thin Films: Properties and Their Astronomical Implications, In *Water in Confining Geometries*, V. Buch and J.P. Devlin, Eds.; Springer: Berlin (2003).
69. C. Manca, C. Martin, and P. Roubin, *Chemical Physics*. 300, 53-62 (2004).
70. R. S. Smith, C. Huang, E. K. L. Wong, and B. D. Kay, *Surface Science*. 367, L13-L18 (1996).
71. Z. Dohnalek, G. A. Kimmel, R. L. Ciolli, K. P. Stevenson, *et al.*, *Journal of Chemical Physics*. 112, 5932-5941 (2000).
72. N. J. Sack and R. A. Baragiola, *Physical Review B*. 48, 9973-9978 (1993).
73. Z. Dohnalek, R. L. Ciolli, G. A. Kimmel, K. P. Stevenson, *et al.*, *Journal of Chemical Physics*. 110, 5489-5492 (1999).
74. R. S. Smith, Z. Dohnalek, G. A. Kimmel, G. Teeter, *et al.*, *Molecular Beam Studies of Nanoscale Films of Amorphous Solid Water*, In *Water in Confining Geometries*, V. Buch and J.P. Devlin, Eds.; Springer: Berlin (2003).
75. O. Andersson and H. Suga, *Physical Review B*. 65, 140201 (2002).
76. G. Kumi, S. Malyk, S. Hawkins, H. Reisler, *et al.*, *Journal of Physical Chemistry A*. 110, 2097-2105 (2006).
77. S. Malyk, G. Kumi, H. Reisler, and C. Wittig, *Journal of Physical Chemistry A*. 111, 13365-13370 (2007).
78. J. A. Mcmillan and S. C. Los, *Nature*. 206, 806 (1965).
79. G. A. Kimmel, K. P. Stevenson, Z. Dohnalek, R. S. Smith, *et al.*, *Journal of Chemical Physics*. 114, 5284 (2001).
80. J. D. Thrower, M. P. Collings, F. J. M. Rutten, and M. R. S. McCoustra, *Journal of Chemical Physics*. 131, 244711 (2009).
81. J. A. Ghormley, *Journal of Chemical Physics*. 46, 1321 (1967).

82. A. Bar-Nun, I. Kleinfeld, and E. Kochavi, *Physical Review B*. 38, 7749-7754 (1988).
83. A. Bar-Nun, G. Herman, D. Laufer, and M. L. Rappaport, *Icarus*. 63, 317-332 (1985).
84. M. P. Collings, M. A. Anderson, R. Chen, J. W. Dever, *et al.*, *Monthly Notices of the Royal Astronomical Society*. 354, 1133-1140 (2004).
85. H. Herzog, B. Eliasson, and O. Kaarstad, *Scientific American*. 282, 72-79 (2000).
86. T. Ikeda-Fukazawa, K. Fukumizu, K. Kawamura, S. Aoki, *et al.*, *Earth and Planetary Science Letters*. 229, 183-192 (2005).
87. Y. Park, D. Y. Kim, J. W. Lee, D. G. Huh, *et al.*, *Proceedings of the National Academy of Sciences of the United States of America*. 103, 12690-12694 (2006).
88. V. Buch, J. P. Devlin, I. A. Monreal, B. Jagoda-Cwiklik, *et al.*, *Physical Chemistry Chemical Physics*. 11, 10245-10265 (2009).
89. G. Natesco and A. Bar-Nun, *Icarus*. 175, 546-550 (2005).
90. R. Zallen, *The Physics of Amorphous Solids*. New York: John Wiley and Sons, Inc. (1983).
91. K. I. Oberg, E. C. Fayolle, H. M. Cuppen, E. F. van Dishoeck, *et al.*, *Astronomy & Astrophysics*. 496, 281-293 (2009).
92. J. J. Loparo, S. T. Roberts, and A. Tokmakoff, *Journal of Chemical Physics*. 125, 194521 (2006).
93. S. Woutersen, U. Emmerichs, H. K. Nienhuys, and H. J. Bakker, *Physical Review Letters*. 81, 1106-1109 (1998).
94. F. E. Livingston and S. M. George, *Journal of Physical Chemistry A*. 105, 5155-5164 (2001).
95. F. E. Livingston and S. M. George, *Journal of Physical Chemistry A*. 106, 5114-5119 (2002).
96. A. M. Shaw, *Astrochemistry: From Astronomy to Astrobiology*. 1st ed. Chichester: Wiley (2005).

97. D. J. Burke and W. A. Brown, *Physical Chemistry Chemical Physics*. 12, 5947-5969 (2010).
98. Q. Chang, H. M. Cuppen, and E. Herbst, *Astronomy & Astrophysics*. 458, 497-505 (2006).
99. K. M. Menten, C. M. Walmsley, C. Henkel, T. L. Wilson, *et al.*, *Astronomy & Astrophysics*. 169, 271-280 (1986).
100. C. Knez, M. Moore, S. Travis, R. Ferrante, *et al.*, *Iau: Organic Matter in Space*. 4, 47-48 (2008).
101. A. C. A. Boogert, K. M. Pontoppidan, C. Knez, F. Lahuis, *et al.*, *Astrophysical Journal*. 678, 985-1004 (2008).
102. K. M. Pontoppidan, A. C. A. Boogert, H. J. Fraser, E. F. van Dishoeck, *et al.*, *Astrophysical Journal*. 678, 1005-1031 (2008).
103. J. Woodall, M. Agundez, A. J. Markwick-Kemper, and T. J. Millar, *Astronomy & Astrophysics*. 466, 1197-U1203 (2007).
104. J. D. Thrower, D. J. Burke, M. P. Collings, A. Dawes, *et al.*, *Astrophysical Journal*. 673, 1233-1239 (2008).
105. R. J. Trumpler, *Publications of the Astronomical Society of the Pacific*. 42, 214-227 (1930).
106. K. I. R. Oberg, E. F. van Dishoeck, H. Linnartz, and S. Andersson, *Astrophysical Journal*. 718, 832-840 (2010).
107. L. B. Dhendecourt, L. J. Allamandola, and J. M. Greenberg, *Astronomy & Astrophysics*. 152, 130-150 (1985).
108. A. G. G. M. Tielens, A. T. Tokunaga, T. R. Geballe, and F. Baas, *Astrophysical Journal*. 381, 181-199 (1991).
109. A. C. A. Boogert, T. L. Huard, A. M. Cook, J. E. Chiar, *et al.*, *Astrophysical Journal*. 729, 92 (2011).
110. M. S. Gudipati, J. P. Dworkin, X. D. F. Chillier, and L. J. Allamandola, *Astrophysical Journal*. 583, 514-523 (2003).
111. V. Wakelam, I. W. M. Smith, E. Herbst, J. Troe, *et al.*, *Space Science Reviews*. 156, 13-72 (2010).

Chapter 2: Experimental Details

Vibrational excitations of the ν_3 asymmetric band of H₂O and time-of-flight (TOF) mass spectroscopy in an ultra-high vacuum (UHV) chamber were used for the studies described in this dissertation. A thorough description of these methods will be discussed here and surface diagnostic techniques, described previously [1-3], will be briefly outlined. During the course of these experiments, the parts of the experimental arrangement that were modified and details of these modifications are described as well.

2.1 UHV System

The UHV system has three tiers, as shown in Figure 2.1. The sample manipulator is attached to the uppermost and smallest tier, labeled A. This was designed for Fourier transform infrared spectroscopy (FTIR) and temperature programmed desorption (TPD) analysis. The largest part of the chamber contains two tiers, labeled B and C, where tier B is designed for surface analysis (laser desorption and time-of-flight spectroscopy) and the bottom-most tier, tier C, is for molecular beam scattering experiments used during previous experiments [4]. The numerous ports on tiers B and C can be used for different experimental arrangements and techniques (e. g. Low Energy Electron Diffraction, High Resolution Electron Energy Loss Spectroscopy and Auger Electron Spectroscopy). The chamber is equipped with a turbomolecular pump (Leybold TurboVac 600 l/s) and backed by a mechanical pump

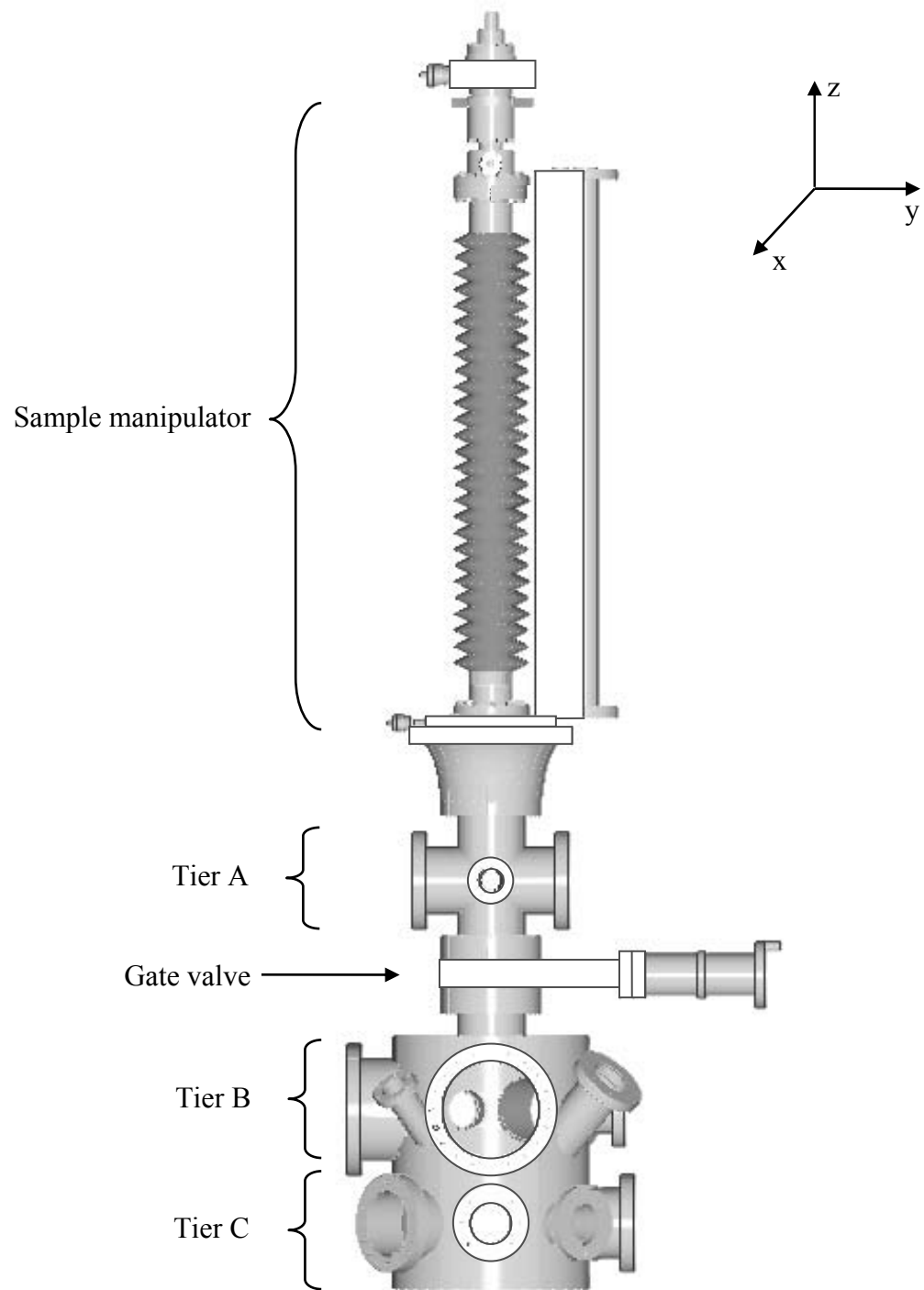


Figure 2.1 A schematic of the UHV chamber and manipulator. The manipulator and top tier are separated from tiers B and C by a gate valve. The manipulator allows for x , y , and z translation of the sample inside the chamber.

(Welch Model 1397). Pressures of $\sim 2 \times 10^{-10}$ Torr are typically attained after heating the chamber for 2 – 3 days to temperatures between 120 and 130 °C.

Heating the chamber is required after venting to atmosphere, because water deposits onto the chamber walls. To remove residual water the chamber is heated evenly, commonly referred to as “baking of the chamber.” This is done by wrapping the chamber with resistive heating tapes controlled individually with variable transformers (Staco-Variac 3PN1010). Failure to evenly heat the chamber causes thermal gradients and could result in cold spots where water aggregates. Desorption rates from these cold spots is relatively small compared to warmer parts of the chamber and can produce “virtual leaks,” limiting the minimum pressure achievable in the chamber. Insulated K-type thermocouples are attached at various points on the chamber to ensure that there is an even heating. Additionally, an internal lamp (Osram 650 W, Model 64535) attached to a timer is used routinely for ~ 6 hours to do a “soft bake” of the chamber to reach base pressure after a series of experiments are conducted.

2.2 Top Tier

The top tier of the UHV chamber is configured for FTIR and TPD surface diagnostic experiments; for full and detailed descriptions of the setup and experiments refer to [1, 2]. The surface manipulator is connected to the top port of this tier and a gate valve (MDC GV-4000M) separates tier A from tiers B and C (see Figure 2.1). The FTIR chamber was designed with a small path length for infrared radiation to improve the signal-to-noise ratio. The compact design enables TPD experiments to be conducted

immediately after an FTIR experiment to minimize any changes in the sample due to molecular mobility at low temperatures (> 100 K).

Four ports have a common focal point where the substrate is located, as shown in Figure 2.2. The IR beam is aligned in the y -direction. A residual gas analyzer (Stanford Research Systems, RGA 300), for temperature programmed desorption (TPD) experiments, and the leak valves (MDC ULV-075), used to introduce the gas into the chamber, are along the x -direction. A pair of calcium fluoride (CaF_2) windows allows IR radiation to enter and exit the FTIR chamber. The RGA, described later in this section, has been modified from its commercial version to accommodate analysis of molecules desorbing from the substrate itself, not from molecules desorbing from other parts of the chamber or from the substrate holder. At the port opposite to the RGA, the two high precision leak valves are connected to a tee and are used to introduce H_2O and CO_2 into the chamber independently from each other.

FTIR and TPD were employed to calibrate any temperature differences between the sample and the reading from a K-type thermocouple. These surface diagnostic techniques will be briefly discussed here. A collimated IR beam from a modified FTIR spectrometer (Nicolet Protégé 460) is directed into the FTIR chamber and focused onto the substrate as shown in Figure 2.3. The spectrometer bench contains a glowbar [5] to produce an IR beam whose spectral output approximates that of a blackbody, which is then directed to the Michelson interferometer [6, 7]. As the collimated IR interference beam exits the spectrometer, it enters a black plexiglass box containing the steering optics. The beam is turned 90° by a plane mirror and directed towards a focusing

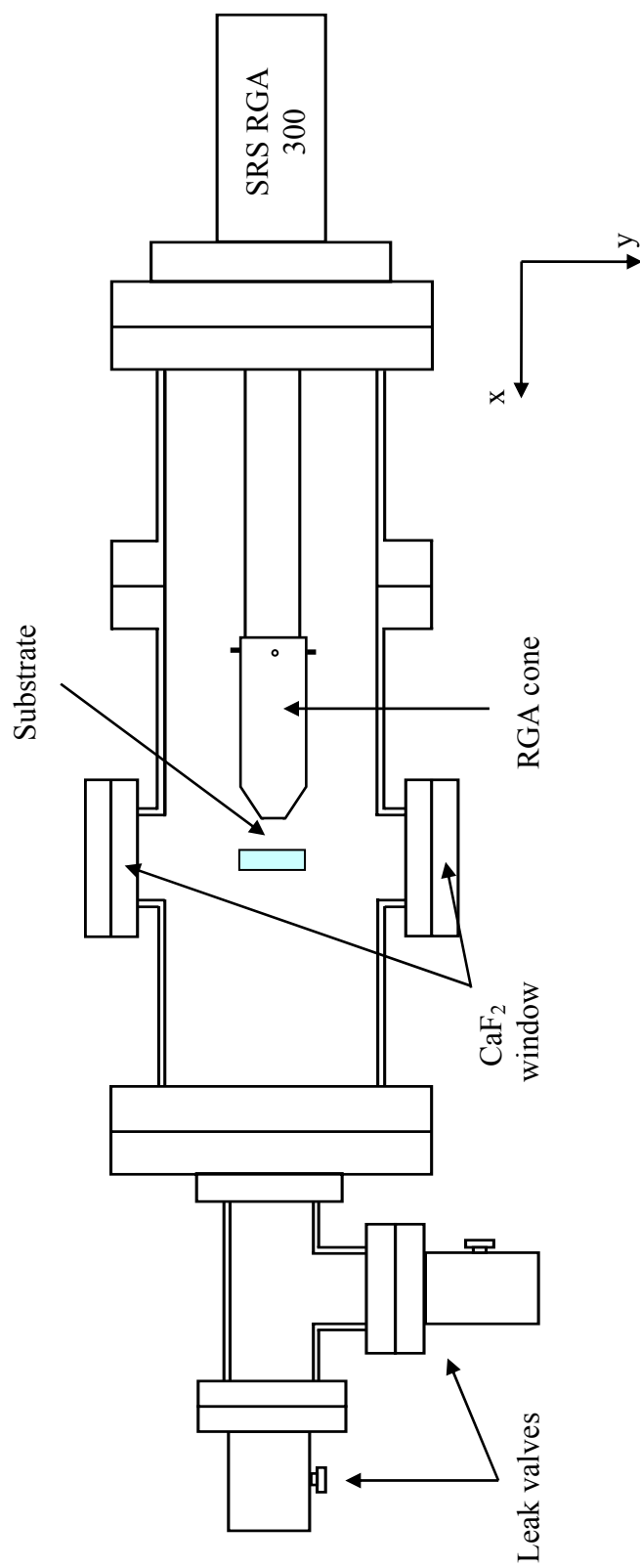


Figure 2.2 Top view of tier A, equipped with an SRS RGA 300 for TPD and CaF₂ windows for transmission FTIR. The RGA cone is 7.6 cm long and can be adjusted to come within 1 mm of the substrate.

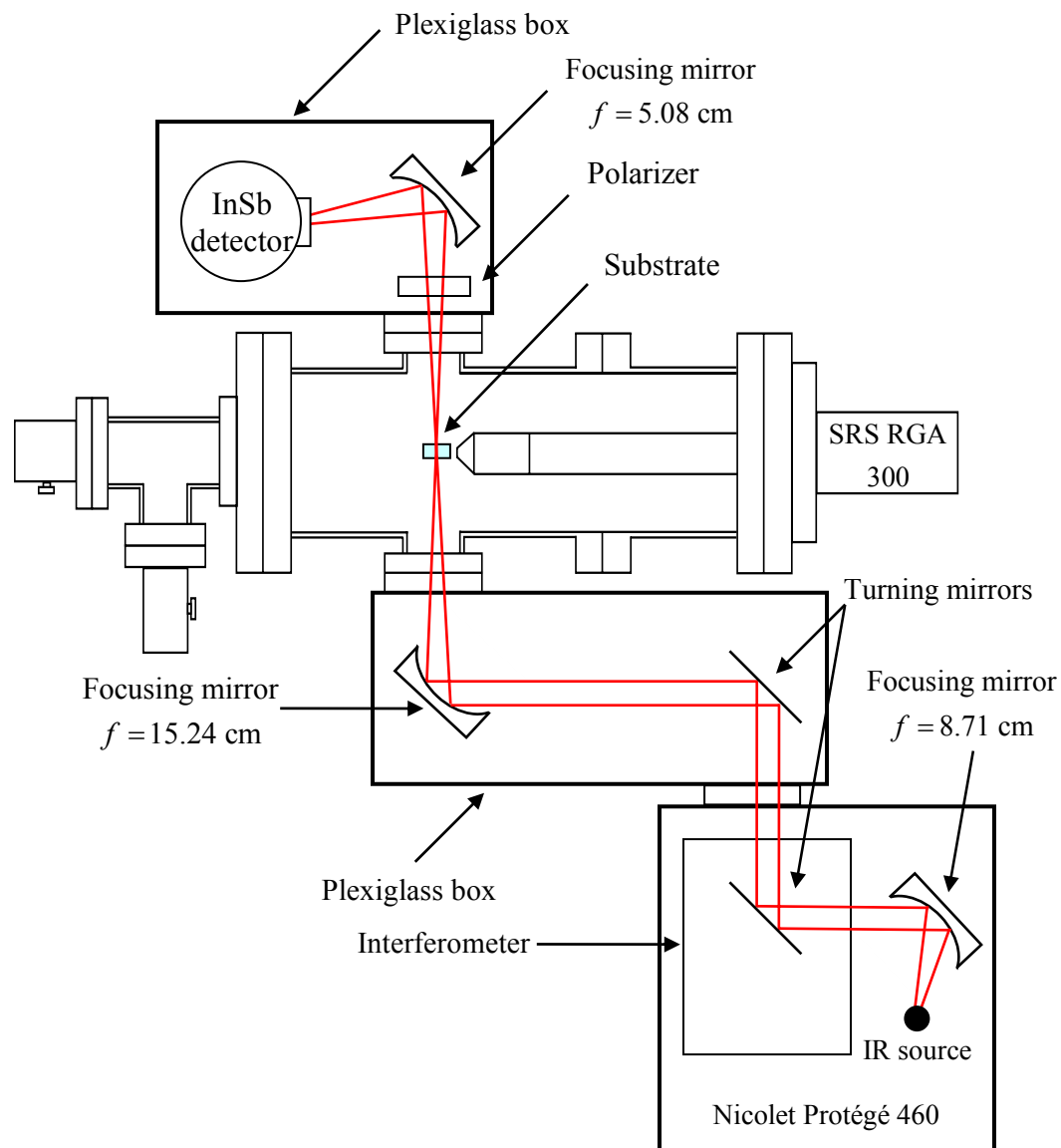


Figure 2.3 Schematic drawing of tier A and FTIR setup. Plexiglass boxes house the optics outside the Nicolet Protégé 460 unit. The boxes and the unit are all purged to remove atmospheric N_2 , CO_2 , and H_2O .

mirror (15.24 cm focal length) to focus the beam onto the sample inside the FTIR chamber to a diameter of ~ 9 mm.

The beam passes through the sample and exits the chamber, entering a second opaque plexiglass box. A second focusing mirror (5.08 cm focal length) focuses the exiting IR beam onto a $2\text{ mm} \times 2\text{ mm}$ indium antimonide (InSb) detecting element. The liquid nitrogen cooled InSb element is highly sensitive ($\sim 10^{-4}$) in the mid-IR wavelength range at cryogenic temperatures ($\sim 80\text{ K}$). Low temperatures are required to reduce noise from thermally induced transitions in close-lying energy levels of the InSb element. To attenuate the incoming IR beam, a wire-grid polarizer (Molelectron, 93 – 98% purity) was placed in the IR beam path. The polarizer consists of an array of parallel aluminum wires on a barium fluoride (BaF_2) surface. When placed perpendicular to the beam path, the polarizer transmits only the light that has its electric field component parallel to the wires; otherwise it is reflected [8].

The FTIR bench and plexiglass boxes containing the optics and InSb detector are all purged, reducing any background contamination due to H_2O and CO_2 , to increase the signal-to-noise ratio in the spectral region of $2000 - 4000\text{ cm}^{-1}$. Purging is done by a dry air gas generator (Whatman, FT-IR 75-62) that filters out H_2O and CO_2 from an in-house compressed air line. This eliminates any variation in humidity and contamination in ambient air.

Surface diagnostics using TPD can provide more detailed information on the overall temperature of the substrate. Temperature gradients generally occur because of poor thermal contacts. TPD has been previously used [9-11] to measure the desorption

temperatures of molecules in a sample of amorphous solid water (ASW). The signal intensity in these measurements is directly correlated to the amount of desorbed material. Therefore, they can be used to diagnose any variations in the actual temperature of the substrate by monitoring desorption signals as a function of temperature.

The RGA quadrupole mass spectrometer (QMS) records ion signals from species desorbing from a sample while a thermocouple, directly attached to the sample, simultaneously records the temperature. If the temperature reading is different than the known desorption temperature of the molecules when the molecules desorb, then the real temperature of the sample is not the same as indicated by the thermocouple. A cone, designed to fit around the RGA set up, has a small aperture (~ 8 mm) at the end near the sample. A screen was spot welded to the aperture to prevent any stray electrons from the RGA ionizer and cause secondary effects by ionizing molecules on the surface. The RGA cone is positioned to provide clearance for the surface manipulator and close enough to the sample to move in the x -direction (Figure 2.2). The sample can come within 1 mm of the cone opening to eliminate background noise or signals originating from molecules desorbing from surfaces other than the sample.

2.3 Middle Tier

Tier B houses the equipment for the principal experiments described in this dissertation. This tier of the UHV chamber was designed for surface analysis [3] and now is used for desorption studies with an infrared pulsed laser. A schematic representation of the experimental setup for IR laser desorption and detection via time-of-

flight (TOF) mass spectrometry is shown in Figure 2.4. A custom-made TOF mass spectrometer (R. M. Jordan), hereinafter referred to as the TOF-MS, is attached to the chamber through a custom-made 8" → 6" reducing flange (USC machine shop). The flange offsets the TOF-MS along the x-axis by ~ 2.5 cm from the center of the chamber to allow for sufficient clearance of the substrate sample holder and a thermocouple attached to the substrate.

A focused pulse of 3424 cm^{-1} radiation enters the chamber through a CaF_2 window and is aligned with its \mathbf{k} -vector normal to the sample. The infrared pulse is generated by Raman shifting the 1064 nm radiation from a Nd:YAG (10 Hz, 10 ns) laser using a 1.1 m long deuterium-filled Raman cell to 61.2 atm pressure and reducing the repetition rate of the laser to 1 Hz with a chopper wheel (ThorLabs MC1000). Details of this laser system are described in Chapter 3. The laser beam passes through a 50 cm CaF_2 focusing lens placed outside the chamber and is aligned in between the extractor and repeller plates of the ionizing region of the TOF-MS – orthogonal to the flight path of the ionized molecules. The sample is centered at the focal point of the laser beam ~ 3 cm away from the TOF-MS assembly.

To monitor the pressure of the UHV chamber, the primary ion gauge is situated on one of the ports in this tier and a secondary ion gauge is located on a port on the bottommost tier. It was not possible to have the ion gauge and the TOF-MS on simultaneously because the repeller and extractor plates become charged and did not function properly with the ion gauge on. Therefore, the ion gauge was turned off immediately before turning on the TOF-MS and conducting an experiment.

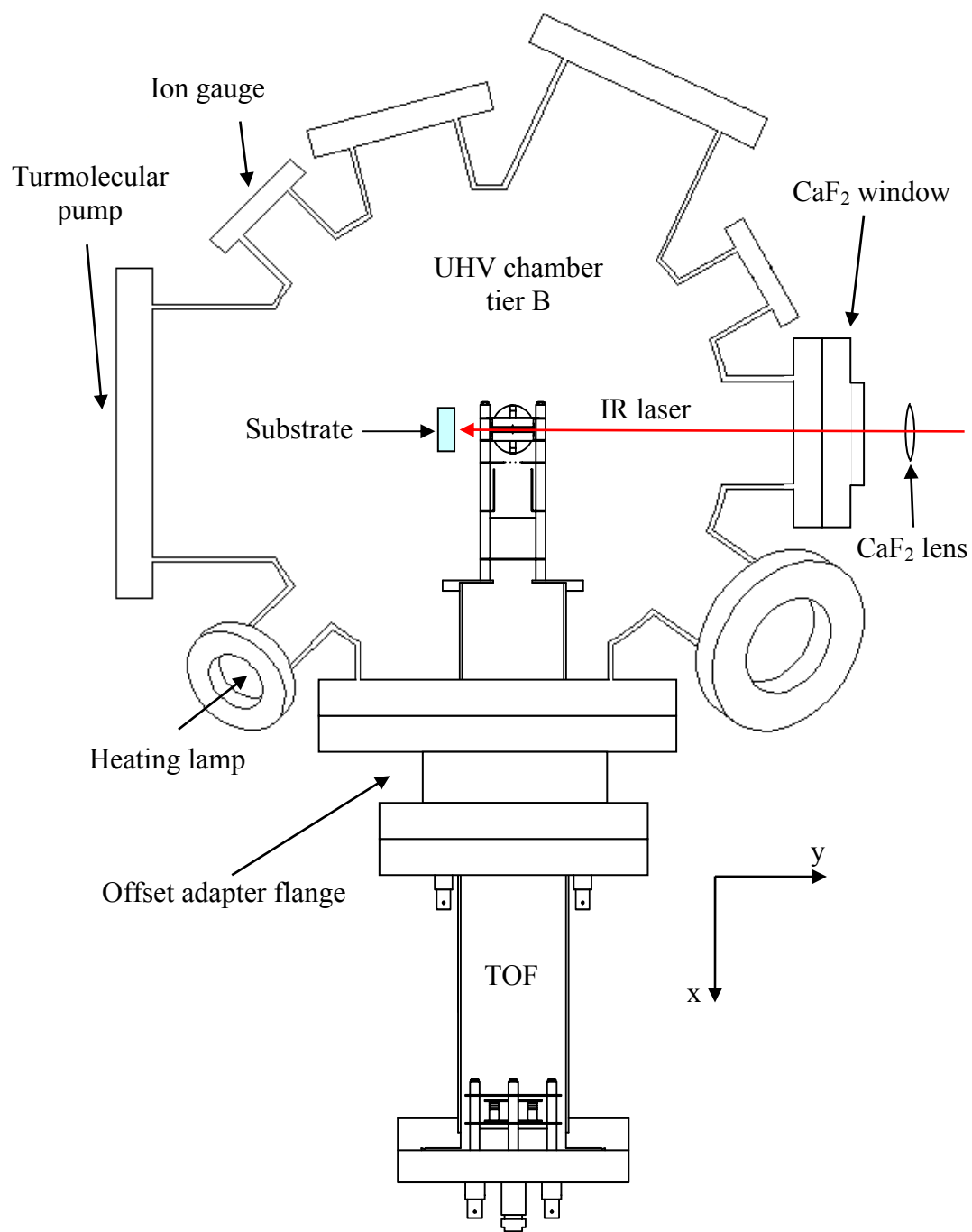


Figure 2.4 Tier B of the UHV chamber. The TOF mass spectrometer is offset from the center to accommodate the substrate. The desorbing molecules are ejected in the y -direction upon radiation from an incoming IR beam and enter the ionizing region.

Resuming operation of the ion gauge after an experiment showed that no appreciable change in background pressure occurred.

2.4 Time-of-Flight Mass Spectrometry

The TOF mass spectrometer is a fairly simple instrument that can yield a wealth of information. The Wiley-McLaren type [12] TOF design is composed of an electron beam (*e*-beam), a set of ion optics (repeller, accelerating, and steering plates), a field-free drift region (42 cm), and a dual stacked microchannel plate (MCP) ion detector. The design shown in Figure 2.5 was customized by Paul Jordan at Jordan TOF-MS Products, Inc. to accommodate our experimental setup.

Upon irradiation of the sample, a plume of neutral molecules desorbs and travels toward the ionization region located in between the repeller and extractor plates. Electron bombardment then creates positive ions in the interaction region. Extraction of the ions towards the flight tube is achieved by creating a potential difference between the extractor and repeller plates in a pulsed mode (up to 200 kHz). The resulting Coulombic force causes the ions to accelerate to an energy of $q \cdot V_{21}$, where q is the ion charge and V_{21} is potential difference. Considering that the same kinetic energy is imparted to all of the ions – assuming that only +1 ions are created – and realizing that the velocity of each ion is inversely proportional to the square root of the mass, lighter ions will collide with the detector sooner than the heavier ions. The resulting mass spectrum is displayed as a measure of drift time through the field-free region. A single pulsed extraction generates a full mass spectrum of the ionized molecules in the plume.

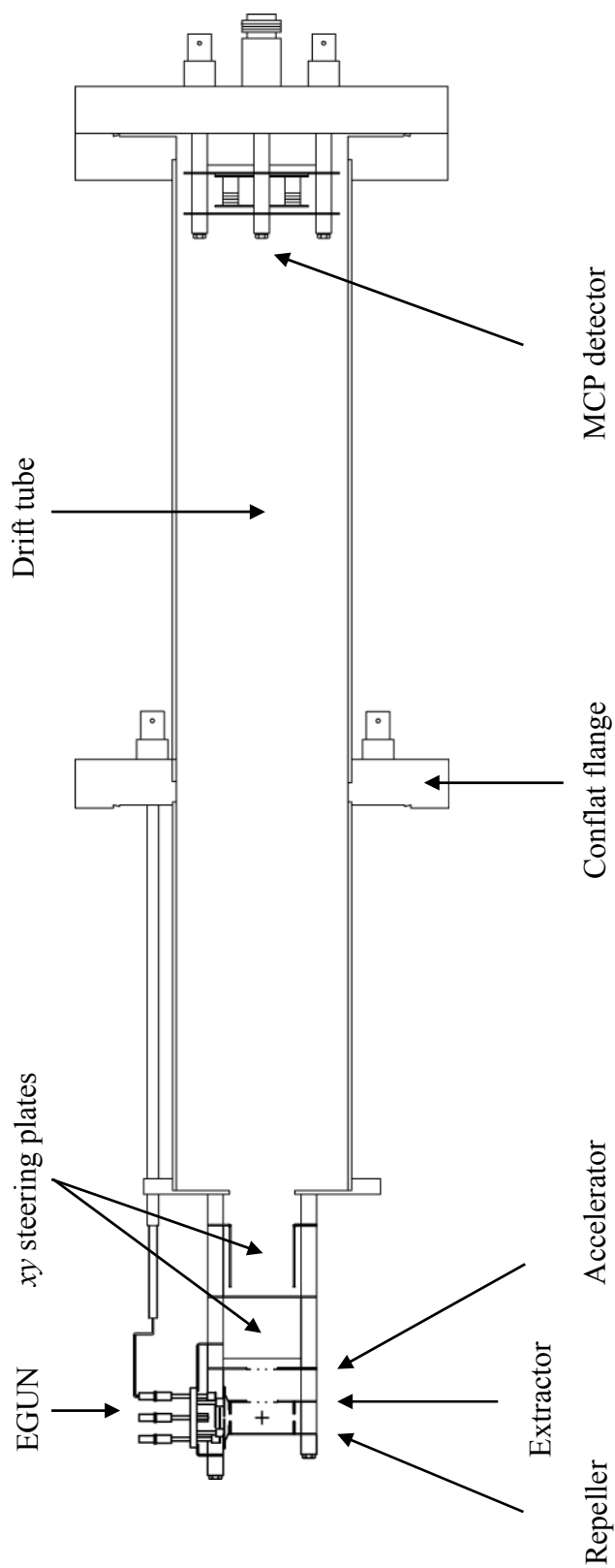


Figure 2.5 Linear time-of-flight (TOF) mass spectrometer designed by Jordan TOF Products Inc. with a 6" conflat flange. The dual plate MCP detector has an 18 mm detecting element.

The repeller and extractor plates are set initially to 1800 V and 1550 V, respectively. A pulse of 250 V equalizes both plates at 1800 V when the neutral molecules are injected into the ionization region. The molecules are ionized by the continuous stream of focused electrons. After $\sim 4 \mu\text{s}$, the extraction plate returns to its original voltage, thereby applying an accelerating force on the ions. The voltages were optimized for a mass resolution around $m/q = 18$.

The output signal from the MCP is a low impedance signal which is connected to a fast amplifier (SRS DC-300 MHz) through a short cable (5 cm) provided by Jordan TOF Products, Inc. to minimize the electrical noise observed with the original 2 m cable. The amplifier is a 4-channel amplifier with an amplification of $\times 5/\text{channel}$. The output of the amplifier is connected to the input of an analog-to-digital converter PCI board (Gage CS8500, 8 bit, 512 kSamples). The signal acquisition rate is 500 MSamples/s providing a temporal resolution of 2 ns and signals are typically recorded for up to 300 μs . At a TOF-MS operating rate of 200 kHz, the TOF-MS completes 60 extractions in 300 μs . This provides the temporal profile of the desorbing plume as it passes through the waist of the e -beam in the ionization region. Data acquisition and processing is achieved with homemade LabView (National Instruments) programs.

2.5 Manipulator

The sample's location and cooling inside the UHV chamber is controlled by a custom built manipulator designed and built by Kurt J. Lesker from Vacuum Generator and modified by MacAllister Technical Services [4]. The manipulator is attached to the

top tier, tier A, and allows cooling of the sample to cryogenic temperatures and translation in along the x , y , and z coordinates as shown in Figure 2.6. The manipulator is able to move 600 mm in the z direction (VG Omniax Translator, z slide module), and 25 mm in each of the x and y directions (VG Omniax Translator, xy stage module). It can also rotate 360° around the z axis through a differentially pumped feedthrough system (VG Rotary Feedthrough, DPRF 25H).

The original design of the manipulator did not provide adequate cooling and was redesigned by replacing the closed cycle refrigeration system (Cryotiger) and cooling rod with the current system described by Suchan [4]. A hollow stainless steel rod housed in the pumped feedthrough serves as a cryostat. One side of the rod is open to atmosphere and the other is silver-brazed to a copper block with mounting points for the sample holder. Liquid nitrogen is poured into the open end of the hollow rod and makes direct contact with the copper block, also known as the cold finger.

Lower temperatures are achieved by bubbling helium gas through the liquid nitrogen. A plastic hose is connected to a helium gas tank (Gilmore, 99.99%) and routed into the hollow rod containing liquid nitrogen. Upon cooling to its minimum temperature, the rod shortens by ~ 3 mm along the z -direction. Returning the assembly to room temperature is achieved by either allowing the liquid nitrogen to vaporize or inserting a tube attached to a dry air or nitrogen gas source, which aids in the vaporization and is the preferred method. Blowing gas into the reservoir also removes traces of condensed water left at the bottom of the rod. Doing so prevents water from

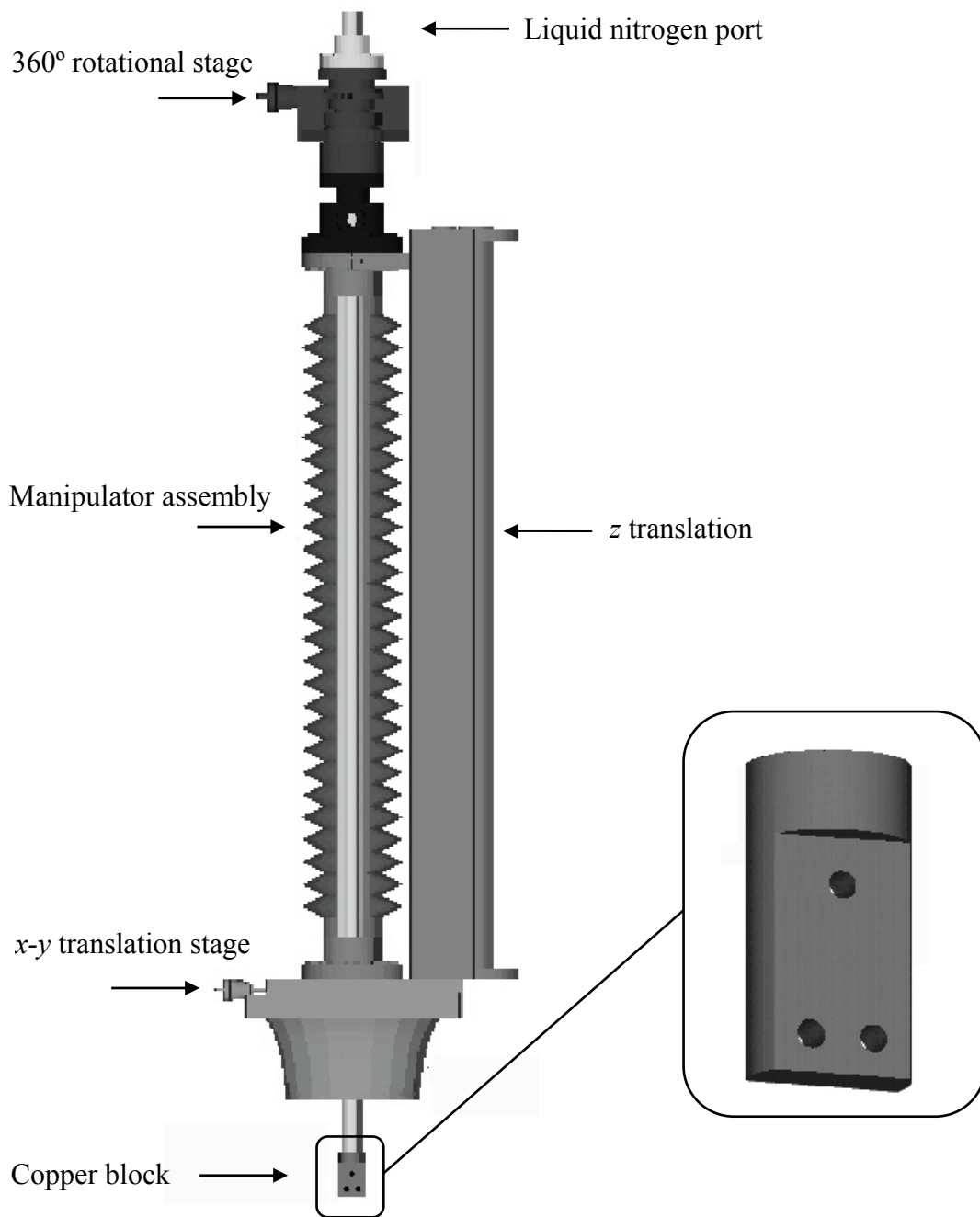


Figure 2.6 A schematic of the manipulator assembly and x , y and z translational stages. The hollow stainless steel rod is used as a liquid nitrogen reservoir and a copper block is silver-brazed at the end to attach the sample holder assembly.

solidifying when the rod is cooled down creating an insulating “ice plug” and limiting the cooling capability.

2.6 Substrate Holder

The substrate holder is a copper housing composed of two electrically isolated pieces and a plate where the substrate is mounted and the thin film is grown. The holder is attached to the cold finger at the end of the cooling rod (Figure 2.6). The substrate holder design is as important as the design of the cooling rod for efficient cooling. For experiments in this dissertation, the holder must allow the substrate to reach temperatures below 120 K to form amorphous solid water (ASW) and above 500 K for annealing and removal of contaminants. Furthermore, the holder must reach temperatures of 90 K in order to physisorb CO₂ on H₂O and must allow the transmission of IR radiation for either FTIR or laser desorption experiments. Both of these experiments, as well as TPD, have similar temperature demands, with laser desorption experiments being the most sensitive to temperature gradients across the substrate. Laser desorption is able to access different areas within a single sample. On the other hand, FTIR and TPD probe the entire sample in a single experiment. Therefore, it is crucial to reduce any temperature gradients across the substrate, and each area probed by laser desorption experiments must be consistent with all others. In addition, the substrate holder must allow for the sample to be placed as close as possible (within 1 mm) to the aperture of the QMS or the ionizing region of the TOF-MS. Previous versions of the surface holder and their limitations are detailed by Malyk and Kumi [1, 2]. These designs are suitable for FTIR and TPD, but not for laser

desorption. Calibration tests will be described in a later section. The only design discussed here is the one used for the experiments in this dissertation (Figure 2.7), which greatly reduces temperature gradients, and can be used with all surface analysis techniques.

The holder is composed of two independent copper pieces (labeled A and B on Figure 2.7) that are separated by a ceramic spacer (McAllister Technical Services) placed at a groove on the top for electrical isolation. The substrate is mounted on a specially designed copper plate (Figure 2.7D) with a heater (Figure 2.7C) cemented to the back of the plate and attached to copper piece B. Parts A and B are attached to the cold finger at the end of the liquid nitrogen-cooled manipulator rod by using three sets of nuts and bolts that are electrically isolated from the copper parts and the cold finger by using a set of ceramic hat washers (McAllister Technical Services). A flat sapphire disc (Esco Products G110040) – diameter 25 mm, thickness 1 mm – is inserted between the sample holder and the cold finger to be used as an electrical isolator and a thermal switch. The thermal conductivity for sapphire is high at low temperatures ($\sim 10 \text{ W}\cdot\text{cm}^{-1}\cdot\text{K}^{-1}$ at 80 K) and low at high temperatures ($\sim 0.3 \text{ W cm}^{-1} \text{ K}^{-1}$ at 400 K) [13]. Thus, the sapphire disc ensures that at low temperatures both the cold finger and the holder remain at similar temperatures and that very little heat is transferred during substrate annealing. This maintains the low temperature of the cold finger while the sample is heated, preventing any molecules adsorbed onto the liquid nitrogen reservoir from desorbing, as well as allowing the sample to be heated and cooled quickly.

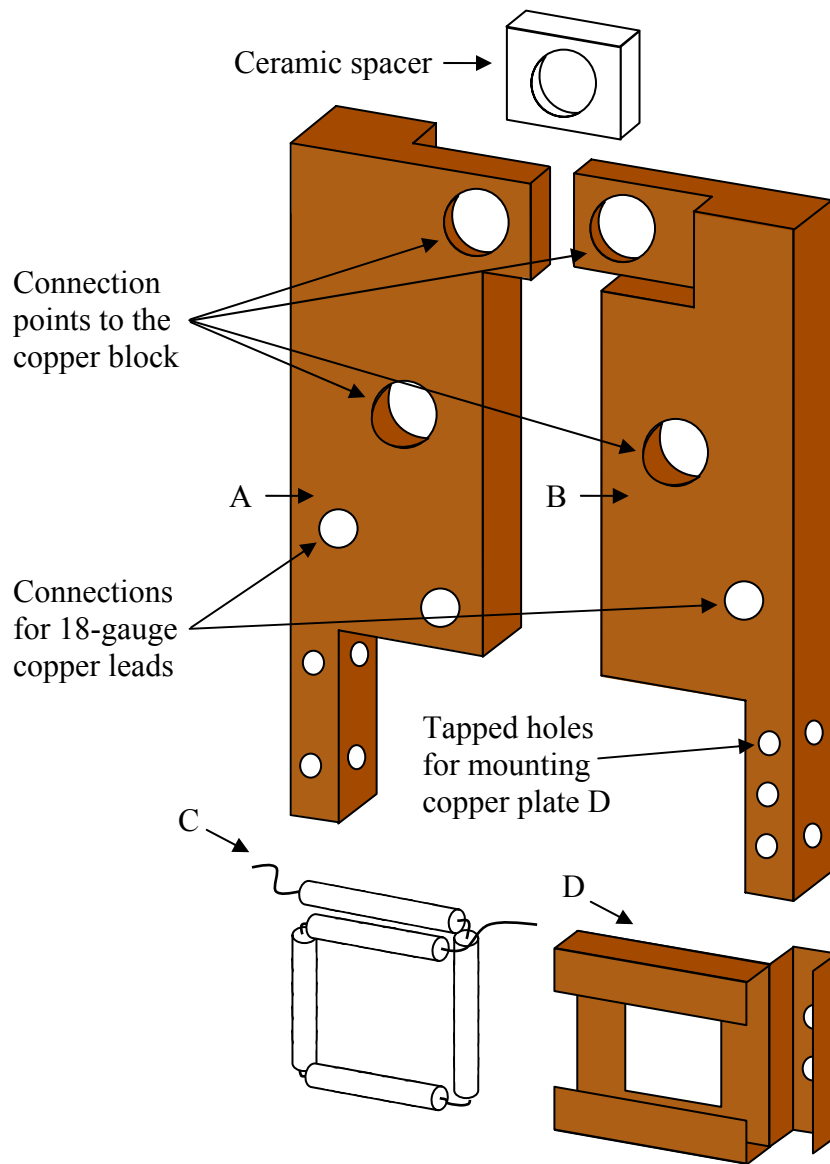


Figure 2.7 Complete sample holder assembly and heater. The assembly consists of two main copper pieces labeled A and B attached to the copper block on the manipulator. The homemade resistive heater C is cemented to the back of the copper plate D. The substrate is mounted on the copper plate, which is attached to B using a pair of screws.

The substrate is placed on a thin copper plate (14 mm × 10 mm × ~ 0.3 mm) and is secured by folding over it the two opposite edges of the plate (Figure 2.7D). In this modified design, the protruding arm that attaches to the copper piece B spans the entire height of the substrate housing. We will refer to the side with the protruding arm as the “cold side” and the other, which is a few degrees Kelvin higher, as the “hot side.” The cold side is attached to copper piece B using a pair of stainless steel screws. Care must be taken to ensure maximum contact between the copper plate and copper piece B. A square opening (5 mm × 5 mm) centered on the substrate housing allows for the transmission of infrared radiation. This was reduced from the original 6 mm × 6 mm. These modifications did not compromise the cooling and heating capabilities required for FTIR and TPD, but it eliminated the slight temperature gradient observed in the diagnostic tests, such that currently $T_{\text{cold side}} \approx T_{\text{hot side}}$.

To heat the substrate, a homemade resistive heater was cemented (Aremco 835M) to the opposite side of the copper plate. The resistive heater is made from tantalum wire (0.38 mm) coiled around the window opening on the copper plate as seen in Figure 2.7C. The wire is isolated by a single hole, round, ceramic insulator rod (Omega ORX-020132). When the heater is cemented onto the plate, the two ends are inserted into copper pieces A and B of the sample holder and secured with stainless steel screws. An electric current is applied through the heater by a pair of 18-gauge copper leads that attach to each of the two electrically isolated copper pieces of the sample holder. The leads enter the chamber through a feedthrough on the surface manipulator (Insulator Seal, 1000 V, 15 A) and are connected to an external power supply (Hewlett-Packard 6259B). A current of ~ 8 A

through the resistive heater provides a heating rate of $\sim 2 \text{ K s}^{-1}$ when heating from 90 K to 400 K.

With this setup, the sample reaches temperatures of $\sim 100 \text{ K}$ by filling the rod with liquid nitrogen. Temperatures of $\sim 90 \text{ K}$ required when dosing CO_2 are achieved by bubbling He gas through the liquid nitrogen reservoir. Once the substrate is cooled down to $\sim 100 \text{ K}$, bubbling of He starts with the gas line tip submerged in the liquid nitrogen in the reservoir. It requires $\sim 100 \text{ ml}$ of liquid nitrogen to submerge the gas line and maintain the low temperature. Any more liquid nitrogen in the reservoir and the temperature will be closer to that with nitrogen alone. The liquid vaporizes at a rate of $\sim 10 \text{ ml min}^{-1}$, therefore continuous monitoring of the nitrogen level is advised.

2.7 Substrate Preparation

A single-crystal MgO substrate was used in the studies in this dissertation (MTI Corporation). The method for obtaining a defect free substrate is crucial for the success of experiments. Different types and concentrations of defects, mainly oxygen vacancies and step defects, have been previously discussed [3] and they vary with different substrate cleaving methods. The method for producing a MgO(100) facet with minimal defects is outlined here.

The proper substrate for these studies should satisfy the main condition that it is transparent to infrared radiation in the region of $\sim 2000 - 4000 \text{ cm}^{-1}$. MgO is transparent ($> 90\%$) over the entire range of $2000 - 33000 \text{ cm}^{-1}$, and can be easily prepared and cleaned *in situ* [14]. The MgO(100), herein referred to as the substrate, is prepared by

cleaving an MgO crystal on both sides in a dry nitrogen atmosphere exposing two clean (100) surfaces ($\sim 1 \text{ mm} \times 10 \text{ mm} \times 10 \text{ mm}$). MgO has a face-centered cubic lattice structure with a lattice constant of 2.98 \AA [15]; the (100), (010), and (001) surfaces are identical and thermally stable. Cleaving and mounting of the substrate on the substrate holder is all done in a plexiglass box purged with dry nitrogen that is designed for this task. After the substrate is mounted on the copper plate, a K-type thermocouple is cemented to the “hot side” edge of the crystal and left under dry nitrogen to cure for ~ 30 mins. Upon curing, the heater is cemented to the opposite side of the plate and again cures for ~ 30 mins. Then, the plate is attached and the heater is connected to the copper pieces. Once complete, the entire assembly is removed from dry conditions and installed immediately on the cold finger inside the UHV chamber. Installation process and closing of the UHV chamber takes ~ 30 min total.

Oxygen vacancies can be filled by annealing the substrate in an oxygen atmosphere. When the UHV chamber is closed and evacuated, the baking procedure described in Section 2.1 is followed for 2 – 3 days. Once the chamber cools down and reaches base pressure of $\sim 2 \times 10^{-10}$ Torr, the MgO(100) substrate is annealed to 600 K for 1 hour in 10^{-7} Torr of oxygen. This process fills any oxygen vacancies and removes carbon contaminants from the surface; it has been shown to produce a clean, defect-free MgO(100) substrate [14].

2.8 Sample Preparation

Layers of amorphous solid water can be grown by background vapor deposition onto an MgO(100) substrate held at temperatures below 120 K [11]. A temperature of ~ 100 K is used for studies involving ASW only films and ~ 90 K for mixed films. Precision leak valves (Varian Model 951-5106) are used to independently introduce gases into the UHV chamber. A pair of leak valves installed on the FTIR tier (Figure 2.2) introduce water vapor and gaseous CO₂, while a third leak valve can be used to introduce a third substance, is installed on tier B. The water and third leak valves are connected to a mechanical pump by 1/4" Swagelok fittings and stainless steel tubing, and are baked to 120 °C to remove contaminants. The leak valve designated for CO₂ dosing is held under constant pressure, connected to a cryogenic sorption pump with 1/2" fittings and tubing. Liquid samples are housed in a homemade glass contained and degassed by several freeze-pump-thaw cycles. The CO₂ cylinder (Gilmore, 99.99%) is connected directly to the leak valve.

The concentration of the gases during deposition is monitored by the nude ion gauge and the purity of the gases is monitored with the RGA mass spectrometer. Background deposition of mixed or layered films is done by first cooling the MgO(100) substrate to ~ 90 K. Next, the substrate is heated to ~ 200 K to remove any material that might have condensed onto the substrate, and then cooled back to 90 K. The leak valves are opened, and the entire chamber is filled with the desired mixture until the desired film thickness is reached. Assuming that the sticking coefficient of the molecules at 90 K is unity and that $\sim 10^{14}$ molecules create one monolayer (ML) by a ratio of the substrate's

area and the molecular dimensions, we estimated that a monolayer coverage is achieved at adsorption rate of $\sim 10 \text{ ML min}^{-1}$ at a background dosing pressure of $\sim 1 \times 10^{-7}$ Torr. The valves are then closed and the remaining background gas is pumped out, returning the chamber to base pressure.

2.9 Temperature Calibration

Substrate temperature is crucial for the growth of amorphous or crystalline films and trapping of guest-molecules. The trapping efficiency of guest-molecules by ASW can be affected by a substrate temperature change of as few as $\sim 3 \text{ K}$. Characterizations of the temperature of desorption for dopant-molecules and water, and the spectral characteristics in the IR of amorphous and crystalline water films grown on a MgO(100) substrate have been previously reported [10, 11]. Distinct temperatures of desorption have been observed for molecules bound to the top of the water film, multilayers, or trapped within the ice film. The peak desorption temperatures and desorption origins for water and CO_2 molecules deposited at 90 K on MgO(100) are tabulated in Table 2.1. A shift of these desorption temperatures and or broadening of desorption peaks could suggest that the ceramic glue on the thermocouple or heater might have broken and separated from the substrate, or there is an uneven contact between the substrate and the copper plate or any of the copper pieces.

FTIR can also be used to characterize the film. The ν_3 asymmetric stretch of solid H_2O centered at $\nu \sim 3250 \text{ cm}^{-1}$ shows distinct spectral features for ASW and the crystalline phase of water ice [11]. ASW displays a broad and structureless band, while

the band for crystalline ice has more structural features and a narrower central peak.

Also, the intensity of a small peak due to the CO₂ ν_3 band at 2275 cm⁻¹ is proportional to the trapped CO₂. The absence of this peak for films deposited at 90 K suggests that there is an inefficient trapping of the CO₂ in the ice.

	<i>T</i> /K	Origin
Multilayer CO ₂	105	Bound to surface H ₂ O
CO ₂ “volcano peak”	165	ASW → crystalline ice phase transition
CO ₂ /H ₂ O codesorption	185	Codesorption with H ₂ O
H ₂ O desorption	185	$\Delta H_{des} = 0.5$ eV from H-bonding
Monolayer H ₂ O	240	$\Delta H_{des} = 0.8$ eV to MgO(100)

Table 2.1 Peak desorption temperatures of water and guest molecules deposited at 90 K on MgO(100).

2.10 Nd:YAG Laser Oscillator Cavity Alignment

The procedure for alignment of the oscillator cavity of the Q-switched Nd:YAG laser (Continuum, NY81C) provided in the service manual is insufficient [16]. An addendum to the oscillator alignment optimization procedure is outlined here. This is assuming that an alignment of the other laser components according to the service manual has determined a need for cavity alignment; this is generally shown by an uneven burn pattern right outside the cavity. The details described herein are for this particular model, although similar components are found in several of Continuum’s Powerlite models.

Figure 2.8a shows a schematic representation of the oscillator cavity, its optics, and the placement of the alignment laser and polarizers. The oscillator cavity is

composed of a total reflecting mirror (M1), the Pockel's cell (PC), the laser rod, and an output coupler (M2). Not shown in Figure 2.8a are a plate polarizer and $\lambda/4$ wave plates which can be removed before the alignment process. A helium-neon (HeNe) laser is steered through the back of M1. The M1 assembly has been modified to accommodate a diode, presumably a pulse counter. It is not necessary to remove the entire M1 assembly to remove the diode; this can be done by pulling on the diode's connecting cable. With the PC removed, the HeNe beam is aligned through the laser rod and out through M2. Then a white piece of paper with a pinhole is placed in between the rod and M2 coupler where the HeNe beam can go through. The rod is a parallelogram with a 2° angle. The reflection from the rod should be be at a 3 o'clock relative to M1. If the laser rod has not

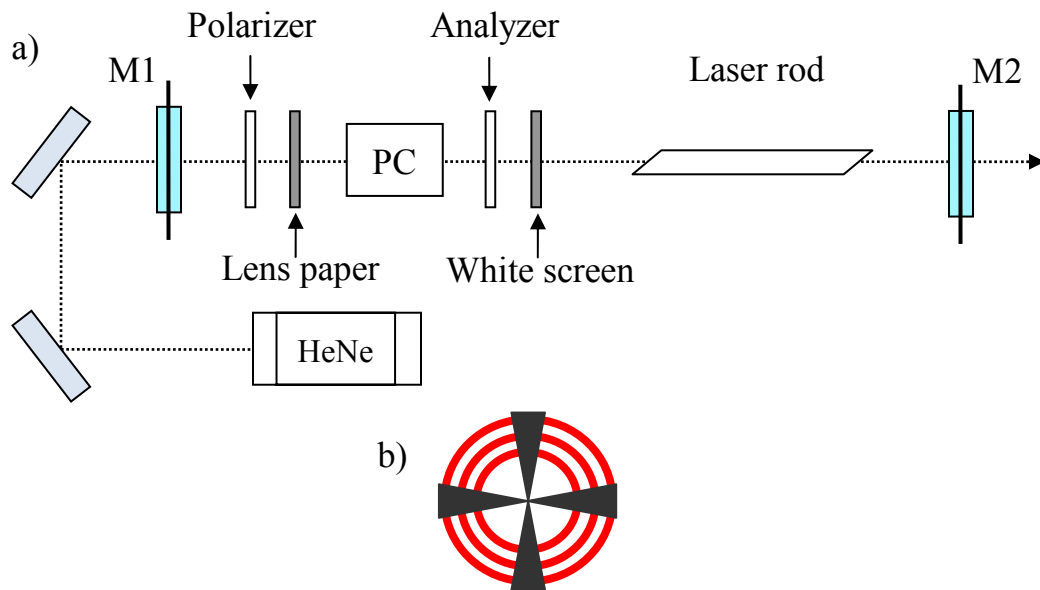


Figure 2.8 a) A schematic representation of the oscillator cavity in a Continuum NY81C laser and the optics required for alignment of the Pockel's Cell (PC). The holder for the total reflecting mirror M1 has a diode mount on the back which the HeNe can enter and be aligned through the exit coupler, M2. The polarizer, analyzer, lens paper, and white screen MUST be removed before Q-switching the laser. b) Maltese cross-like figure observed through the PC on the white screen.

been removed, no adjustments are necessary. If it has, then the rod must be rotated so that the reflection is in this position.

A PC uses a high electric field to change the phase and polarization of the light passing through it. By illuminating the PC with a diffuse light and placing it in between a pair of cross polarizers an optical figure, called Maltese cross, is formed (Figure 2.8b). Alignment of the PC's z -axis is best done by centering the Maltese cross along the cavity's optical axis [17]. With no voltage applied, the PC is placed such that the k -vector of the HeNe beam is normal to the surface of the PC. Two crossed polarized films are placed before and after the PC, referred to as the polarizer and analyzer. A piece of lens tissue is placed in between the polarizer and the PC to provide divergent scattered light from the incoming HeNe beam. At this point the Maltese cross-like figure is displayed on a white screen placed after the second polarizer (Figure 2.8b). The scattered light displays the cross while a portion of the intensity is transmitted. The PC is adjusted to center the pattern on the optical axis of the cavity.

2.11 Synchronization and Triggering

Temporal overlap of the instruments' triggering pulses is essential to i) reduce the rate of the 10 Hz incoming laser beam down to 1 Hz repetition rate; ii) operate the ionization and pulsed extraction voltages of the TOF-MS; and iii) record data such as the ion flight time is relative to $\tau = 0$, the time the laser pulse is fired. A set of three digital delay/pulse generators (Stanford Research Systems, DG535) are used to coordinate the temporal overlap of square pulses used to trigger the Q-switch, the chopper wheel, the

TOF-MS, and the Gage card (see Figure 2.9). The DG-535 can provide precisely timed transistor-transistor logic (TTL) pulses required to externally trigger the electronics. The low jitter (50 ps rms) and high precision (5 ps) allow for a synchronization of triggering pulses at different repetition rates. Each pulser can provide up to 9 pulses at a single repetition rate. The DG535s are daisy chained off of the 10.0 MHz reference clock of the DG535 that triggers the TOF-MS. A TTL pulse (4 V, 10 μ s) is set at rates up to 200 kHz to trigger the TOF-MS, 100 Hz to operate the chopper wheel, and 10 Hz to operate the Nd:YAG laser and the Gage card. The overlap and time delays of all the pulses are monitored by a Tektronix 754D 4-channel digital oscilloscope.

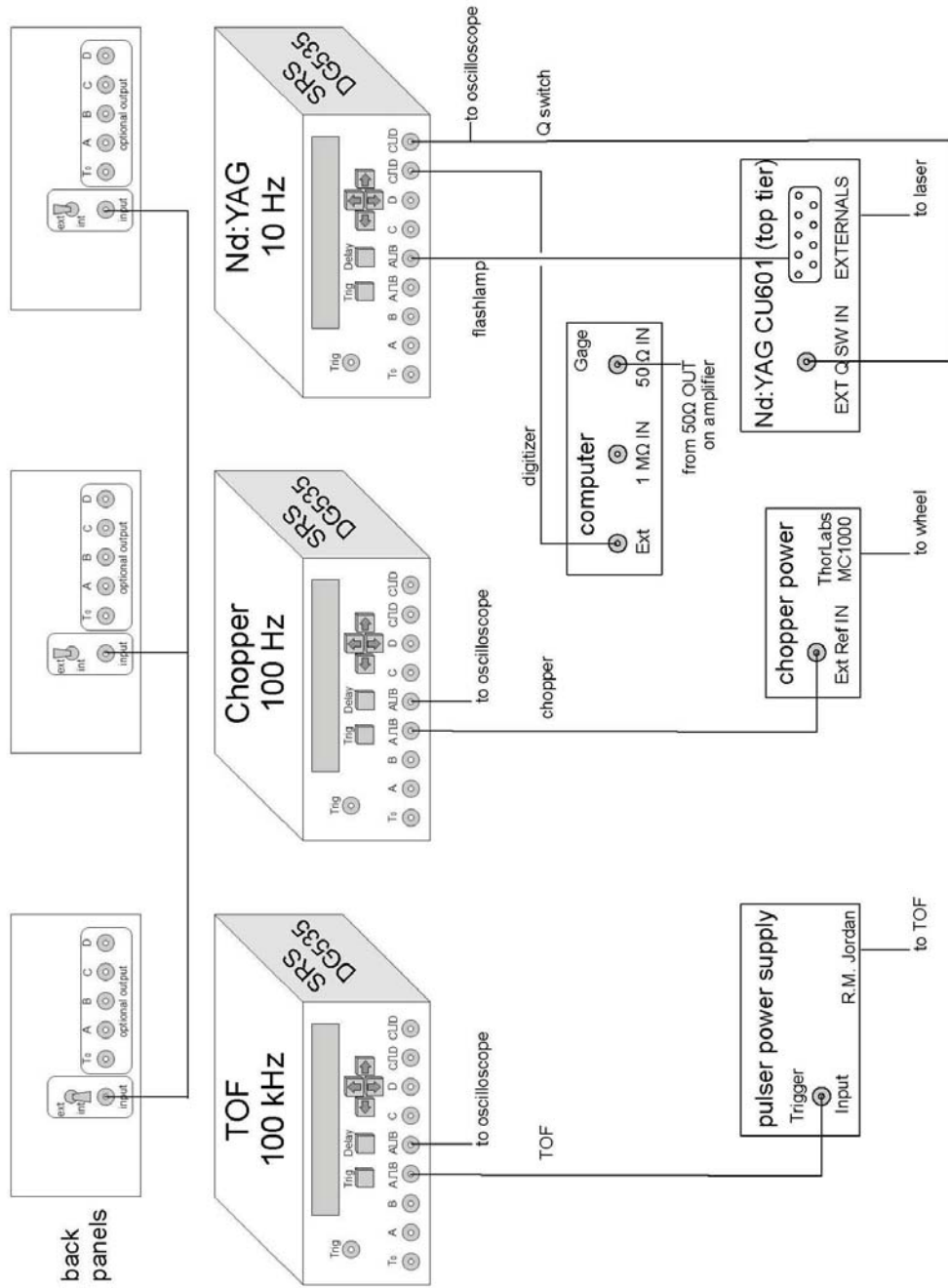


Figure 2.9 Three SRS DG535 Digital Delay/Pulse Generators sharing a common 10.0 MHz timebase to drive and synchronize the 100 kHz TOF, the 100 Hz chopper wheel, and the 10 Hz Nd:YAG laser.

2.12 Chapter References

1. S. Malyk, *Transform and guest-host interactions in amorphous and crystalline ice*. Department of Chemistry. Los Angeles: University of Southern California (2009).
2. G. Kumi, *Fourier transform infrared studies of guest-host interactions in ice*. Department of Chemistry. Los Angeles: University of Southern California (2007).
3. S. A. Hawkins, *Fourier transform infrared spectroscopy and temperature programmed desorption of water thin films on the MgO (100) surface*. Department of Chemistry. Los Angeles: University of Southern California (2004).
4. M. M. Suchan, *Molecules-surface interactions in HCl/MgO and Water/MgO Systems*. Department of Chemistry. Los Angeles: University of Southern California (2001).
5. D. A. Skoog and J. L. Leary, *Principles of Instrumental Analysis*. Fort Worth: Harcourt Brace College Publishers (1992).
6. P. Griffiths and J. A. De Haseth, *Fourier Transform Infrared Spectrometry*. New York: John Wiley and Sons, Inc. (1986).
7. B. C. Smith, *Fourier Transform Infrared Spectroscopy*. Boca Raton: CRC Press (1996).
8. X. J. Yu and H. S. Kwok, *Journal of Applied Physics*. 93, 4407-4412 (2003).
9. S. Hawkins, G. Kumi, S. Malyk, H. Reisler, *et al.*, *Chemical Physics Letters*. 404, 19-24 (2005).
10. G. Kumi, S. Malyk, S. Hawkins, H. Reisler, *et al.*, *Journal of Physical Chemistry A*. 110, 2097-2105 (2006).
11. S. Malyk, G. Kumi, H. Reisler, and C. Wittig, *Journal of Physical Chemistry A*. 111, 13365-13370 (2007).
12. W. C. Wiley and I. H. McLaren, *Review of Scientific Instruments*. 26, 1150-1157 (1955).
13. Sheikh, II and P. D. Townsend, *Journal of Physics E-Scientific Instruments*. 6, 1170-1170 (1973).

14. L. K. Hodgson, *Photodissociation, molecule-surface collision-induced dissociation and direct adsorbate photolysis of nitrous molecules*. Department of Chemistry. Los Angeles: University of Southern California (1993).
15. K. H. Rieder, *Surface Science*. 118, 57-65 (1982).
16. *Operation and Maintenance Manual for the NY80 Series Laser*. Santa Clara: Continuum (1991).
17. W. Koechner, *Solid-State Laser Engineering*. New York: Springer (2006).

Chapter 3: Stimulated Raman Scattering and Time-of-Flight Mass Spectrometry

Experimental techniques for the removal and detection of materials from surfaces such as laser ablation coupled with a mass spectrometer have been developed throughout the years. Studies for controlled and efficient material removal continues to be of great importance due to the continued need to push the frontiers of technology, especially with regards to the lithography and semiconductor industries [1, 2]. The two primary methods discussed in this chapter include the generation of a 3424 cm^{-1} radiation source *via* stimulated Raman scattering (SRS) in D_2 and time-of-flight mass spectrometry (TOF-MS). These methods are used for ablation of thin films of amorphous solid water (ASW) and for detection and identification of the ablated material.

3.1 Introduction

The fundamental OH stretch of water exhibits a broad absorption of $\sim 400\text{ cm}^{-1}$ (FWHM). This signal has a maximum at $\sim 3400\text{ cm}^{-1}$ and $\sim 3250\text{ cm}^{-1}$ for liquid water and ice water respectively. The excitation of this band invites promising desorption studies using a number of radiation sources, such as Er:YAG [3, 4], optical parametric oscillators (OPO) [5], and free-electron lasers [6]. These radiation sources have all shown that maximum desorption of thick, micrometer-sized films of polycrystalline ice and amorphous solid water (ASW) occurs at a wavelength of $\sim 3\text{ }\mu\text{m}$, which is close to the absorbance of liquid water. Er:YAG lasers are predominantly used because of their fundamental $2.94\text{ }\mu\text{m}$ output.

The focus of previous desorption studies has mainly centered on films whose thickness is a few times larger than the penetration depth of a 2.94 μm photon, and are several times thicker than the ones used in these studies. The penetration depth is given by $p = \lambda/4\pi k$ where the wavelength and the refractive index k for liquid water yields $p \sim 0.8 \mu\text{m}$ [7]. An alternative to using the ErYAG laser involves scattering the beam of a high power pump laser in a high pressure cell containing a carefully chosen gas in order to generate the desired wavelength at $\sim 3 \mu\text{m}$. The latter method, based on stimulated Raman scattering (SRS), is the one implemented in these experiments.

The SRS process has been an important spectroscopic tool since the 1920s [8-10]. Raman-scattered radiation is an attractive light source because of the potential for the conversion of laser radiation to different frequencies. The down and up-conversion shifts of the pump beam frequency are referred to as Stokes and anti-Stokes, respectively. To produce these frequency shifts, a high-power laser is focused into a high-pressure gas cell, thereby exciting the molecules to a virtual energy level. Relaxation to a higher vibrational state produces Stokes (ω_S) radiation. The pump energy can further vibrationally excite the molecule in a higher energy level from which it relaxes to the ground state, generating anti-Stokes (ω_{AS}) radiation as seen in Figure 3.1.

The frequency of the Stokes and anti-Stokes light is given by

$$\omega_S = \omega_p \mp n\omega_g \quad (3.1)$$

where the pump frequency, ω_p , is shifted by n -orders of the vibrational frequency of the gaseous medium, ω_g .

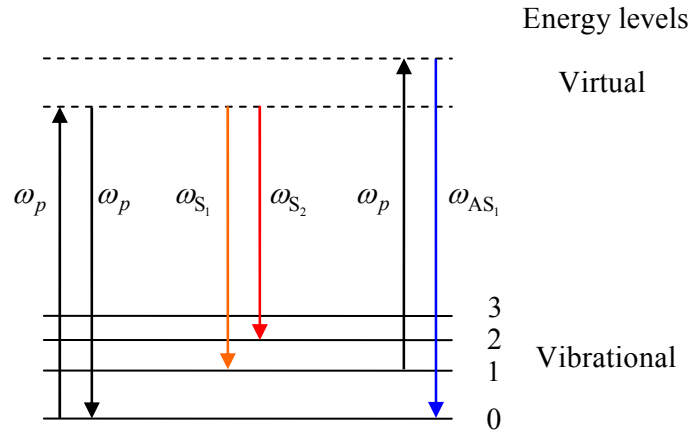


Figure 3.1 Energy level diagram for stimulated Raman scattering (SRS). Stokes (ω_S) and anti-Stokes (ω_{AS}) frequencies are generated with an initial pump (ω_p) source.

The pump-Stokes conversion efficiency, or Raman gain, depends strongly on the wavelength and intensity of the pump beam. The intensity amplification for the Stokes beam as a function of distance, z , from the focal point in a gaseous media is given by

$$I_S(z) = I_S(0)e^{\alpha z} \quad (3.2)$$

where $I_S(z)$ is the exponentially amplified Stokes light intensity from the initial intensity, $I_S(0)$ – produced by stimulated Raman scattering – with a plain-wave gain coefficient α and a distance z along the Raman cell [11, 12]. The gain coefficient is given by

$$\alpha = \frac{\rho \cdot I_p}{\lambda_S (\lambda_S + \lambda_p) \Gamma_R} \quad (3.3)$$

where ρ is the molecules' number density, I_p is the pump beam intensity, λ_S and λ_p are the Stokes and pump wavelengths, and Γ_R is the FWHM Raman linewidth. Equation 3.3 describes the non-linear process for generating higher order Stokes beams. The $1/\lambda_S^2$ dependence on the Raman gain shows the rapid decay on the gain and subsequently on the intensity of higher order Stokes light.

The groups of Chu *et al.* and Schoulepnikoff *et al.* have studied the Raman conversion of 532 nm and 266 nm in H₂, D₂, and CH₄ with vibrational frequencies of 4155 cm⁻¹, 2987 cm⁻¹, and 2917 cm⁻¹, respectively [13, 14]. They have reported up to 30% conversion efficiency for the second Stokes in H₂ using these lower wavelengths with 150 mJ pump energy.

A higher number density for the gas and a narrow Raman linewidth are preferred in general. Studies of the Raman linewidth show that its broadening is roughly proportional to the pressure of the gas for pressures greater than 10 atm [15, 16]. The conversion of the 10 ns fundamental beam of a Nd:YAG operating at 10 Hz has been successfully achieved in our group using a D₂ cell filled to ~ 61 atm. Such a system has yielded a ~ 4% conversion efficiency to the second Stokes (S₂, 3424 cm⁻¹) [17] and has proven advantageous due to its straightforward operation and minimal maintenance as compared to other laser systems operating near the mid-infrared. Additionally, this system offers a tunable range of Raman scattering by changing to different gases and/or pumping frequencies.

Analysis of ablated material using a Wiley-McLaren type TOF mass spectrometer (TOF-MS) allows for fast detection and processing, yielding a wealth of information. TOF-MS is a sophisticated yet simple apparatus designed to measure the translational energy distribution of ions using a set of voltage plates, a pulse generator to drive the plates, a drift tube, and a detector. A detailed description of TOF mass spectrometry was given in Chapter 2; thus, this chapter will only provide a general review of this detection technique.

Typically, the ablated material expands radially, traveling orthogonal to the extraction path of the TOF-MS with an initial velocity v_A , as shown in Figure 3.2. In principle, ablated material enters the ionizing region where ions are formed either with an electron beam or an ionizing laser. The ionizing region is held at a constant electric field for the duration of the ionization process until a pulse on the extracting plate changes the field and the ions travel to the accelerating region.

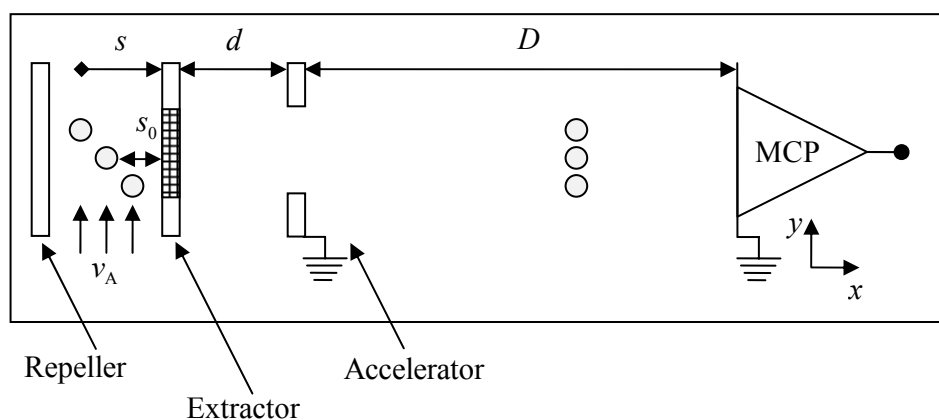


Figure 3.2 Geometry of TOF mass spectrometer showing the ionization, s , accelerating, d , and drift regions, D . Molecules with an initial velocity v_A and position $s = s_0 \pm \delta s_0$ cross each other at some distance along D and are detected by an MCP detector.

All ions experience the same total energy, U_{tot} independent of mass, given by

$$U_{tot} = U_0 + qsE_s + qdE_d \quad (3.4)$$

and are accelerated towards the field-free drift region, ultimately reaching the detector [18]. The total energy acquired by an ion is dependent on its initial energy U_0 , its charge q , and the intensity and duration of the applied electric fields in the ionizing and accelerating regions, s and d respectively. Ultimately, the flight time for an ion to reach

the detector is given by

$$T(U_0, s) = T_s + T_d + T_D \quad (3.5)$$

where D represents the field-free region of the TOF-MS. Here, separation of the ions takes place according to their different mass-to-charge ratios (m/q). Broadening of the signal generated from identical ions is minimized by optimizing the space resolution of the instrument by focusing the ions along the drift tube. Space focusing refers to the fact that some molecules in the ionizing region are closer to the detector than others, as seen in Figure 3.2. Closer molecules acquire less energy and eventually the more energetic molecules cross them along the drift region, ultimately producing a shift in their arrival times. The applied fields are optimized experimentally for the mass of H_2O ($m = 18$ amu) to enhance the resolution of the instrument.

The TOF-MS has the advantage that it can extract and accelerate ions at rates up to 200 kHz, collecting a mass spectrum every 5 μs . The recorded mass spectra represents the composition of a point on the desorption plume as it reaches the ionizer. With a continuous ionizing source, a series of extracting pulses can monitor the ablated plume as it passes through the ionizing region. This generates a temporal profile composed of many individual mass spectra, thereby producing the TOF distribution, $f(t)$.

Given the configuration of the apparatus and ionization source, only those molecules traveling along the surface normal, y axis, can be detected. $f(t)$ can be analyzed for the initial velocities of ablated molecules upon ablation, after it is converted to the velocity domain. The velocity distribution, $P(v_y)$, is found the following relation

$$f(t)dt = P(v_y)dv_y \quad (3.6)$$

$$P(v_y) \propto t^2 f(t) \quad (3.7)$$

where the derived time-to-velocity Jacobian is proportional to t^2 . Ablation studies of thick films have commonly reported that the velocity distribution, for collision-free molecules, can be described by a thermal Maxwell-Boltzmann distribution expression [19, 20]

$$P(v_y)dv \sim v_y^2 \exp\left[\frac{-m(v_y - u)^2}{2k_B T}\right] \quad (3.8)$$

where v_y represents the molecule's velocity in the y direction, u is the stream velocity, k_B is Boltzmann's constant, and T is the plume temperature. However, it is often found that the temperatures obtained are difficult to correlate to any physical meaning and the cooling effect of the substrate for material close to the surface is neglected [19, 21, 22].

In this chapter thin films of ASW have been ablated with infrared laser radiation. The focusing conditions of the infrared radiation on the sample are optimized experimentally with minimal adjustments made to the TOF-MS space resolution parameters. The expansion of desorbed material is analyzed using Maxwell-Boltzmann distributions. The term "thin films" is reserved for those films thinner than the penetration depth of the 3424 cm^{-1} photon, $< 0.8 \text{ }\mu\text{m}$.

3.2 Experimental

3.2.1 Pulsed IR Ablation

A schematic of the experimental setup for the generation of a single infrared pulse is shown in Figure 3.3. IR radiation is generated by stimulated Raman scattering (SRS) the fundamental laser line of a Q-switched Nd:YAG laser (1064 nm, Continuum NY81C) in D_2 ($\nu = 2987 \text{ cm}^{-1}$). The laser is optimized to provide a 10 ns pulse at a 10 Hz repetition rate and with a pulse energy of up to 800 mJ/pulse. Alignment of the oscillator cavity to achieve these parameters was described in Chapter 2. Circularly polarized Nd:YAG laser radiation is steered by two dielectric mirrors, M1 and M2 (Thorlabs NB1-J14, $\lambda = 1047\text{-}1064 \text{ nm}$, 45° AOI) and is linearly polarized by a $\lambda/4$ plate (CVI QWPO-1064-05-4, 1064 nm). The incoming pulse is focused into a 1.1 m long Raman cell, filled with D_2 to a pressure of 61.2 atm, by a 1 m focal length BK7 lens, L1 (CVI PLCX-25.4-515.1-C-1064, AR 1064 nm). The light that exits the Raman cell is collimated by a 75 cm focal length CaF_2 lens, L2 (Thorlabs LA5956) and refocused with a 1 m focal length CaF_2 lens, L3 (Thorlabs LA5835) through a 60° CaF_2 prism. The prism is used to separate the various wavelengths generated by the SRS process (Table 3.1). The incident linearly polarized beam is aligned to the Brewster angle (55°) relative to the normal of the CaF_2 prism ($n_{\text{CaF}_2} = 1.418$) for greatest light transmission. Any reflected light is collected by either a beam block or a fast liquid nitrogen cooled MCT detector (Cincinnati Electronics SDD-7854-S1-05M, 16 MHz) connected to a 500 MHz digital oscilloscope (Tektronix 754D).

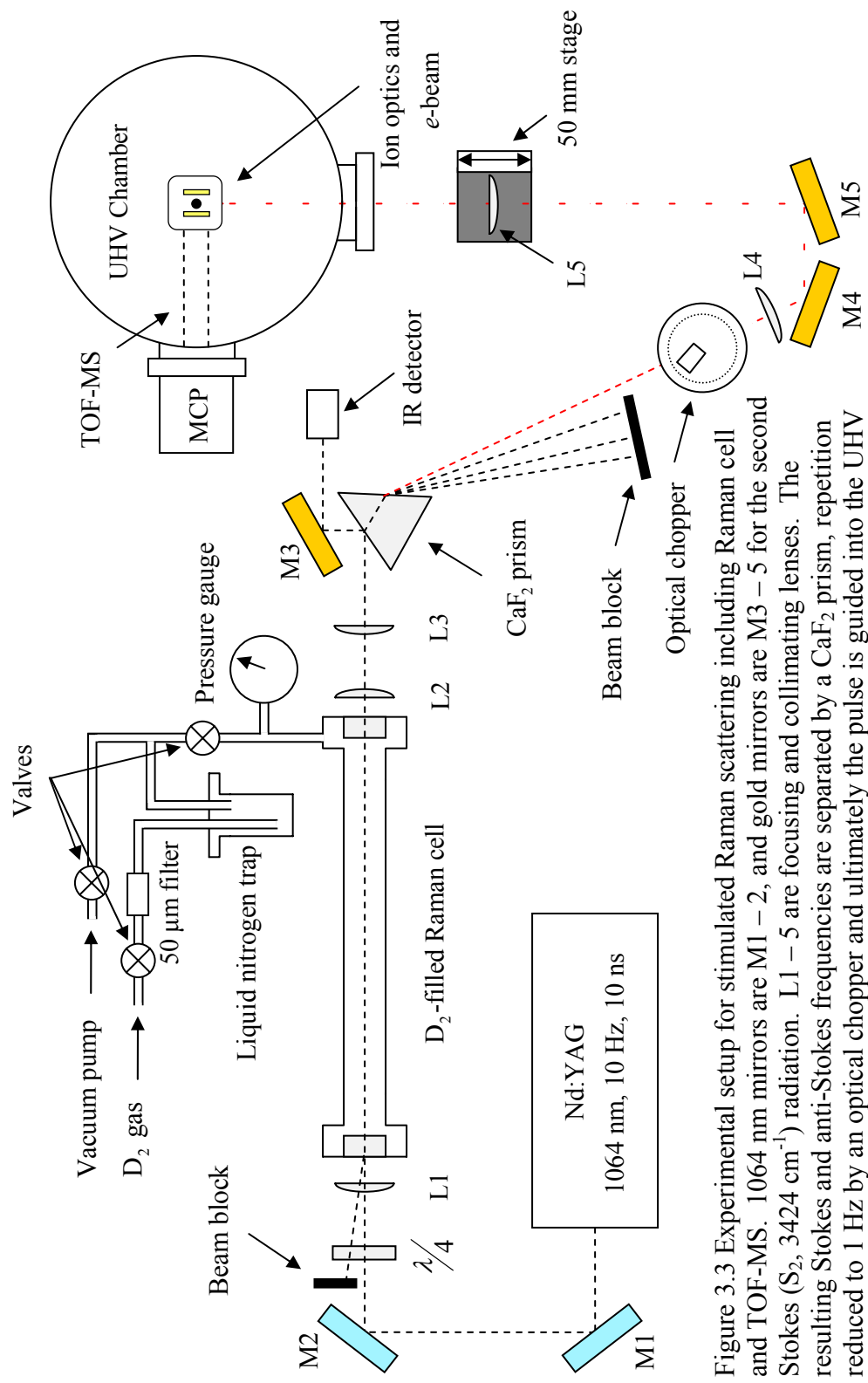


Figure 3.3 Experimental setup for stimulated Raman scattering including Raman cell and TOF-MS. 1064 nm mirrors are M1 – 2, and gold mirrors are M3 – 5 for the second Stokes (S_2 , 3424 cm^{-1}) radiation. L1 – 5 are focusing and collimating lenses. The resulting Stokes and anti-Stokes frequencies are separated by a CaF₂ prism, repetition reduced to 1 Hz by an optical chopper and ultimately the pulse is guided into the UHV chamber and aligned through the ion optics of the TOF.

The second Stokes radiation (S_2 , 3424 cm^{-1}) is isolated and its energy is attenuated with a set of microscope slides (Corning Inc.). Single-pulse experiments are achieved by reducing the S_2 repetition rate from 10 Hz to 1 Hz using a chopper wheel (ThorLabs MC1000) with a custom-built blade. The single pulse is steered by a set of gold mirrors, M4 and M5 (ThorLabs PF10-03-M01) towards the CaF_2 window on the UHV chamber. The pulse is focused onto the sample by a 50 cm focal length CaF_2 lens, L5 (unknown manufacturer), mounted on a translational stage (Newport Model 430) to facilitate focusing adjustments.

	ν/cm^{-1}	λ/nm
ν_{D_2}	2987	3348
S_2	3424	2920
S_1	6411	1560
Fundamental	9398	1064
AS_1	12385	807
AS_2	15372	650

Table 3.1 Wavelengths and frequencies for stimulated Raman scattering of 1064 nm in D_2 . n-order Stokes (S_n) and n-order anti-Stokes (AS_n).

The custom-built TOF-MS (Jordan TOF Products, Inc.) has an electron impact ionizing beam (e -beam) and a dually stacked microchannel plate (MCP) ion detector. The e -beam is aligned along the z -direction, orthogonal to the incoming radiation pulse. The extracting and accelerating regions in the TOF-MS are each 2.54 cm in length and the grounded field-free drift region is 42 cm to the MCP.

3.2.2 The Raman cell

The 1.1 m long Raman cell has a 2.54 cm inner diameter constructed out of stainless steel. Windows are mounted at the ends of the Raman cell with Viton o-rings and are secured with a stainless steel plate using a Teflon gasket and 6 mounting screws. The cell pressure is maintained at 61.2 atm, but was designed to withstand internal pressures up to 82 atm. The minimum window thickness required to withstand an applied pressure is determined by

$$W_{\min} = \sqrt{\frac{1.1PD^2}{MR}} \quad (3.9)$$

where the minimum window thickness, W_{\min} , depends on the desired pressure P , the diameter of the unsupported portion of the window D , and the strength of the material, the modulus of rupture MR . For an internal pressure of 82 atm and a window opening of 21 mm, the minimum thickness required for a fused silica window with an MR of 476.2 atm is 9 mm (Table 3.2).

Window material	Transmission range /nm	Index of refraction	Modulus of rupture /atm
BK7	330 – 2100	1.507 @ 1064 nm	163.3
Fused silica	185 – 2500	1.450 @ 1064 nm	476.2
Sapphire	180 – 4500	1.714 @ 2940 nm	4421.8
CaF ₂	170 – 7800	1.418 @ 2940 nm	360.5
MgF ₂	120 – 7000	1.361 @ 2940 nm	489.8

Table 3.2 Optical properties of common window materials [23].

The 1064 nm pulse enters through a fused silica window (CVI PW-1550-UV, $d = 38$ mm) with a 13 mm thickness. The entrance and exit ports of the cell are tilted $\sim 2^\circ$ to prevent any back reflection from damaging the laser optics. The resulting wavelengths exit through a 13 mm thick CaF_2 window (ISP Optics CF-W-38-13, $d = 38$ mm). CaF_2 transmits $\sim 90\%$ of the radiation between 200 and 7600 nm.

The Raman cell requires ~ 200 L of D_2 (Advanced Specialty Gases, 99.999%) to fill it to 61.2 atm at STP conditions. It is necessary for the gas to be of high purity to ensure maximum conversion efficiency [17]. The D_2 is introduced into the cell through a port at the exit flange also used to monitor pressure and evacuate the cell. A 68.1 atm pressure gauge (Swagelok) and a liquid nitrogen cooled trap are connected through 1/2" tubing; a 0.5 μm pore filter (Swagelok SS-4F-05) is connected to the trap with 1/4" tubing. The trap is filled with 3 mm borosilicate glass beads (Sigma-Aldrich Z143928) to increase the surface area of the cold trap and further purify the incoming gas by removing any remaining condensable contaminants.

The cell, trap, and connections are designed to withstand baking temperatures of ~ 120 °C under vacuum generated by a mechanical pump (Edwards E2M-18). The cell is baked for 2 days if it is vented to atmosphere; the connections must always be baked before refilling the cell with D_2 . Once at room temperature, the trap is cooled with liquid nitrogen and gas is introduced into the cell in ~ 4 atm intervals until the desired pressure is reached to prevent over-pressurizing the cell. This arrangement has achieved $\sim 4\%$ conversion efficiency with maximum pump energy of 190 mJ/pulse. This upper limit on

the pump energy is to prevent thermal gas breakdown and window damage on the Raman cell by the focused beam.

3.2.3 Thin Films of ASW

Thin films of ASW are deposited on a MgO(100) single crystal substrate in an ultra high vacuum (UHV) chamber with a base pressure of $\sim 2 \times 10^{-10}$ Torr according to the procedures described in Chapter 2. A brief description is included here.

The MgO(100) single crystal substrate ($\sim 1 \text{ mm} \times 10 \text{ mm} \times 10 \text{ mm}$) is held in place by a thin copper plate and mounted on a copper block. The copper block is attached at the end of a liquid nitrogen cryostat inside the chamber capable of x , y , and z translation and 360° rotation. Substrate temperatures of 100 K are achieved by filling the cryostat with liquid nitrogen. A K-type thermocouple is cemented to one edge of the crystal and a resistive heater is cemented to the back of the substrate holder. The heater is composed of a tantalum wire loop isolated by a ceramic rod.

Water vapor forms an amorphous solid when deposited onto a substrate at temperatures $< 120 \text{ K}$. Liquid water is held in a glass container and it is degassed by several freeze-pump-thaw cycles. The vapor is introduced through a high-precision leak valve and deposited onto the substrate by background filling the chamber. The chamber pressure is monitored by an ion gauge situated on a port at the same level as the substrate and TOF-MS. Thin films of ASW of 300 – 400 monolayers (ML) that are 100 – 120 nm are reported in these experiments.

3.3 Results and Discussion

The quantum conversion efficiency for the generation of n^{th} Stokes by the stimulated Raman scattering process, Y_{S_n} , is given by

$$Y_{S_n} = \frac{E_{S_n} \lambda_{S_n}}{E_p \lambda_p} \quad (3.10)$$

where E_{S_n} and λ_{S_n} refer to the energy and wavelength of the n^{th} Stokes beam, respectively. Similarly, E_p and λ_p refer to the pump energy and wavelength, respectively. The conversion efficiency of the pump 1064 nm pulse to the second Stokes (S_2 , 3424 cm^{-1}) in the Raman cell with 61.2 atm of D_2 is shown in Figure 3.4. The energy of the S_2 , E_{S_2} , is measured before the chopper wheel and after the CaF_2 prism (Figure 3.3). Energies of approximately 20% lower are measured at the chamber CaF_2 window due to absorption and reflectivity from the optics.

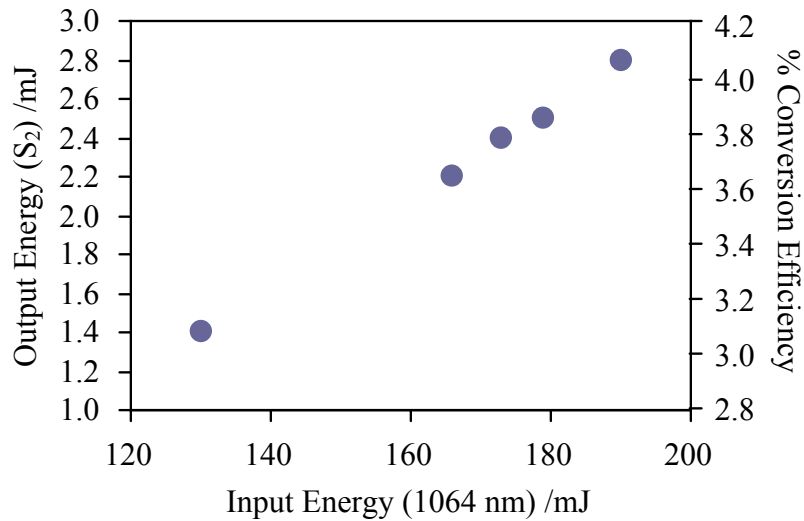


Figure 3.4 SRS conversion efficiency of 1064 nm pulse to S_2 radiation in 61.2 atm of D_2 .

Desorption of H₂O from the ablation of ASW with S₂ is measured. A 300 ML ASW film (~ 100 nm) is deposited at T = 100 K and irradiated with $E_{S_2} = 1.7$ mJ/pulse. Neutral molecules travel towards the ionizing region of the TOF-MS where the *e*-beam ionizes them with a mean energy of 70 eV. The repeller and extracting plates are initially set at 1800 V and 1550 V, respectively. A voltage of 250 V is applied for ~ 4 μs to equalize the plates during the ionization period. At the end of this period, the plates return to their original voltages and ions translate into the accelerating region at a rate of 100 kHz.

The accelerated molecules enter the field-free drift region and are detected by the MCP detector set at -2600 V. The resulting H₂O⁺ ion signal from the TOF-MS is monitored through consecutive pulses of S₂ radiation at the same spatial location on the ice film. The signal is integrated to its FWHM and its decay over consecutive pulses is observed to occur in less than 9 pulses (Figure 3.5). The signal reaches a minimum by pulse 5 and then remains at a low intensity for subsequent pulses. $E_{S_2} = 0.7$ mJ shows no immediate decay, but instead shows a low intensity throughout the irradiation with 9 pulses comparable to the later pulses for $E_{S_2} = 1.7$ mJ.

Irradiation with different energies is done on a new area within the same sample ~ 1 mm from each other. Spatial isolation of the desorption areas is achieved because the efficient thermal transfer to the substrate. The film thickness is orders of magnitude smaller than the beam width that heat is deposited vertically with negligible lateral heating. H₂O molecules are ejected from irradiated column region that subsequent pulses probe down the same column.

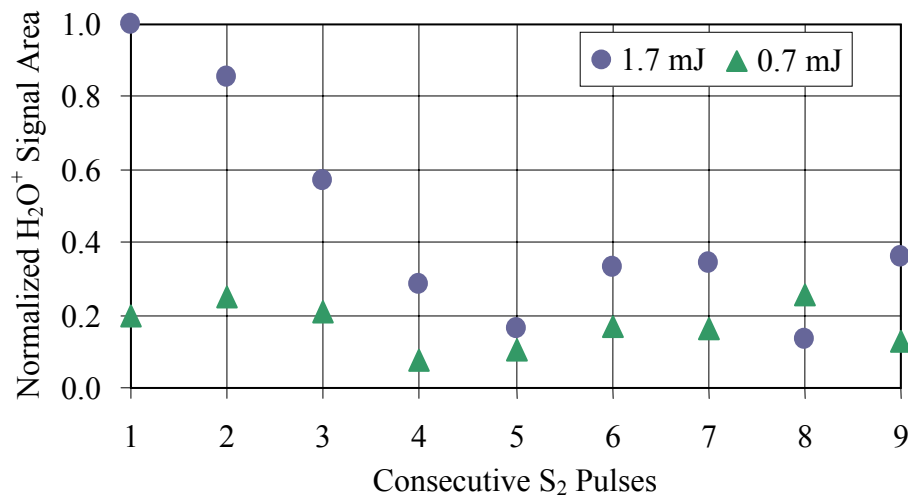


Figure 3.5 H₂O⁺ ablation signal with 9 consecutive pulses of S₂ radiation at the same spatial location. Infrared pulse energies of 1.7 mJ (circles) and 0.7 mJ (triangles); each energy irradiates an independent area on the film. The ASW film thickness is 300 ML (~ 100 nm) at T = 100 K.

Depth-profiling by Livingston *et al.* showed that a 2.94 μm pulse with energy of 0.65 mJ/pulse is able to remove ~ 0.5 μm of ice from a 5 μm thick crystalline film [7]. In this experiment, the first 10 pulses showed a constant yield, while the following 20, showed an exponential decay. As one nears the substrate, the heat is essentially deposited directly into the substrate desorbing a minimal amount of the ice layers remaining on the substrate. It is estimated that pulse 1 removes an upper limit of ~ 30 ML when irradiated with this higher energy, based on a conservative estimate that ~ 50% of the ASW film in Figure 3.5 is removed through the first 9 pulses of 1.7 mJ radiation and that no significant amount of ice is removed due to efficient heat transfer into the substrate. The yield decreases rapidly, such that by pulse 3 and onwards, a trend similar to irradiating with a lower energy is observed where these estimates show desorption of < 10 ML/pulse.

To improve removal of water under these conditions, we increase the laser fluence (*energy/area*) by optimizing the focusing conditions of the radiation. A 50 cm CaF₂ focusing lens is used to focus the pulsed S₂ radiation onto the center of the sample. The pulse is aligned and centered through the ionizing region of the TOF-MS and at a normal incidence to the sample. The substrate is positioned ~ 12 mm away from the TOF-MS assembly to avoid any connections. Outside of the chamber, the lens is mounted on a unidirectional translational stage and parallel to the direction of the beam.

The optical properties of a focusing lens are shown in Figure 3.6 which displays parameters to achieve a minimal waist diameter for the focused beam. A focusing lens with curvature R_i , focuses a collimated Gaussian pulse with an initial diameter ($1/e$) of w_i down to a waist of w_f at the focal point f . The propagation of the Gaussian beam can be simply described by

$$w^2(z) = w_f^2 \left[1 + \left(\frac{\lambda z}{\pi w_f^2} \right)^2 \right] \quad (3.10)$$

which shows that the beam diameter will increase slowly near the waist and eventually increase proportionally to z allowing for a margin of error near the focal point. The radiation spot diameter was experimentally determined to be ~ 0.5 mm at the focal point. As the laser fluence increases along these ranges of energies, the amount of material removed increases as well by varying the energy (Figure 3.5). The effect of increasing the fluence by optimizing the lens' focal point can be seen from the single-pulse desorption, shown in Figure 3.7, after a 400 ML ASW film was irradiated with an energy of 2.3 mJ/pulse. Each spectrum corresponds to pulse 1 on a new area on the ASW film.

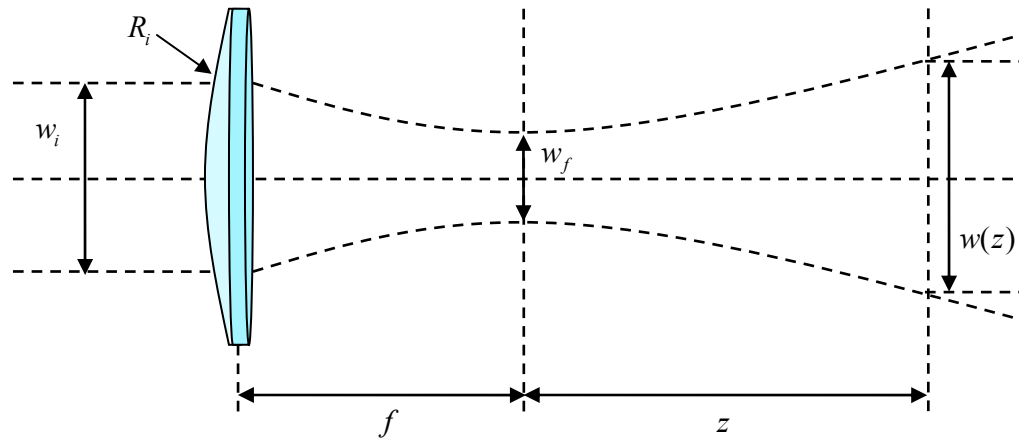


Figure 3.6 Parameters of a plano-convex lens with focusing length f of an incoming collimated Gaussian pulse with a $(1/e)$ diameter w_i . The diameter increases to $w(z)$.

The spectra are the temporal evolution of the desorbing plume as it travels through the ionizing region. The ions generated are extracted by a Coulombic force at a rate of 100 kHz, therefore a mass spectrum is recorded every 10 μs where the main peak is due to H_2O^+ . The extractions are collected for the duration of the plume ($\sim 200 \mu\text{s}$). As seen in Figure 3.7, the intensity of the signal corresponding to H_2O^+ increases with focusing optimization. The overall profile of the plume in Figures 3.7a, c, and d show that 20 μs after the radiation pulse, a significant amount of material arrives at the detector decaying by the second extraction. This decay is followed closely by another wave of ions with its maximum intensity arriving at a $\sim 50 \mu\text{s}$. On the other hand, an increase in overall ablated material is observed in Figure 3.7b. As the focal point nears the film, the energy is deposited and confined into a smaller area; therefore energy deposition becomes more effective allowing more H_2O molecules to desorb with higher translational energies.

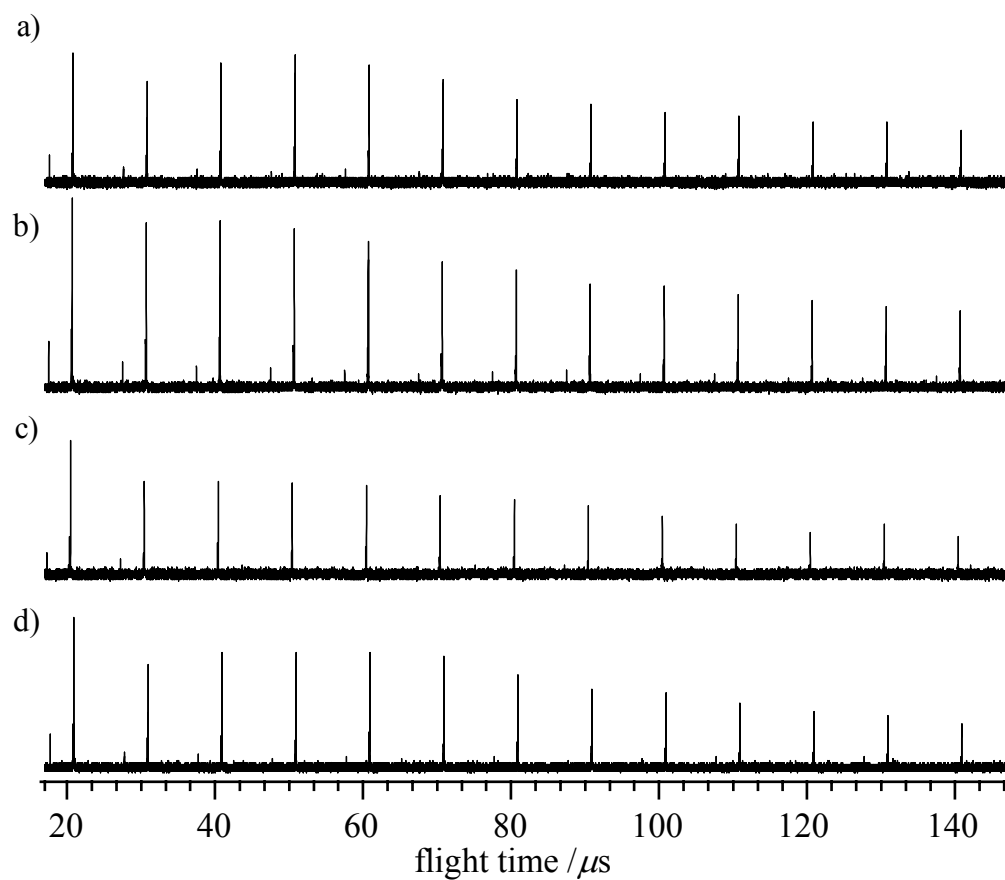


Figure 3.7 Temporal envelope of desorbed plume from a 400 ML ASW film irradiated with 2.3 mJ of IR energy. The major peaks are the H_2O^+ signal from each extraction at 100 kHz resulting in a mass spectrum every 10 μs for the duration of the plume. Spectra show the changes in the envelope after varying the distance between the substrate and a 50 cm CaF_2 focusing lens. Assuming that larger energy fluences result in molecules desorbing at earlier times, b) shows the optimum focusing distance at $47.90 + \sigma$ /cm with a) -0.15, b) 0.00, c) 0.25, and d) 0.75.

Furthermore, at lower lying levels of the H_2O^+ signal, emerging signals corresponding to protonated water clusters can be seen in the form of $(\text{H}_2\text{O})_n\text{H}^+$, where n corresponds to the number of water molecules present (Figure 3.8). Clusters have been observed by other groups and are attributed to a violent boiling of the ablated material under high laser fluences [24-28]. The evolution of these water cluster signals can be seen in Figure 3.8 during focusing optimization. As the fluence is increased by approaching the focal point of the radiation to the sample, clusters begin to appear in the first and second extractions. Similarly to the temporal profile in Figure 3.7b, optimization of the focusing shows the material arriving earlier in time.

Desorption of clusters at earlier times with increased fluence suggests that mechanical stress on the solid is also increased. This results in the ejection of water fragments in addition to monomers mainly observed in normal evaporation. The optimal focusing conditions are those showing the greatest signal intensity of monomer H_2O^+ and protonated clusters. The optimized focusing distance is at 47.90 cm from the center of the chamber.

To shed light on the velocities of the desorbed water molecules, the temporal profile from Figure 3.7c is transformed to the velocity domain and fitted with a combination of Maxwell-Boltzmann distributions at different translational temperatures (Equation 3.8) shown in Figure 3.9. The velocity distribution is obtained by multiplying the temporal profile, $f(t)$, by the Jacobian derived from Equation 3.6 for the transformation from the time domain to the velocity domain ($C \times t^2$), where C is a

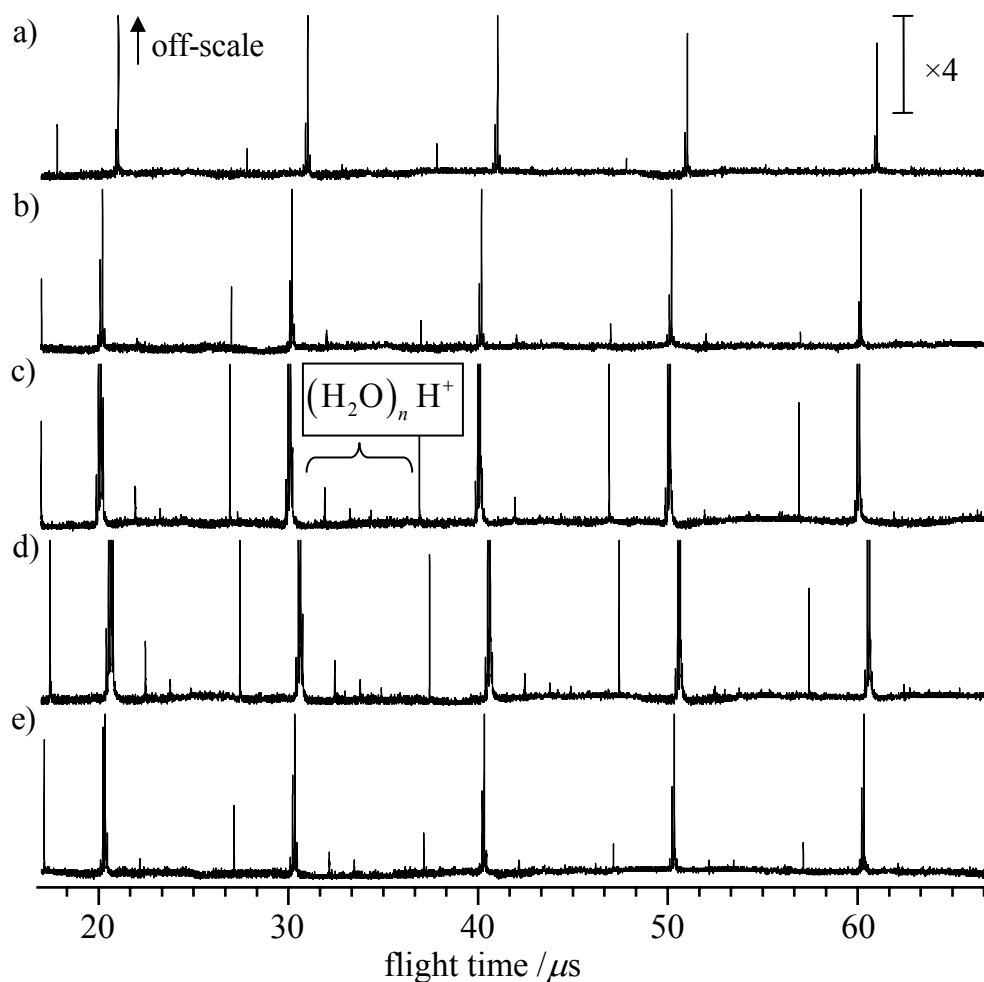


Figure 3.8 $(\text{H}_2\text{O})_n\text{H}^+$ cluster formation during the optimization of the focal point of S_2 radiation. Similar conditions as in Figure 3.7 but taken with $\times 4$ magnification. The larger peaks corresponding to H_2O^+ monomers are off-scale, while the smaller peaks are due to protonated water clusters showing $n = 2 - 4$ d) This spectrum shows the largest cluster intensity observed through the 3rd extraction. Focusing distance at $47.90 + \sigma$ /cm with a) -3.00, b) -2.00, c) -0.25, d) 0.00, and e) 0.50.

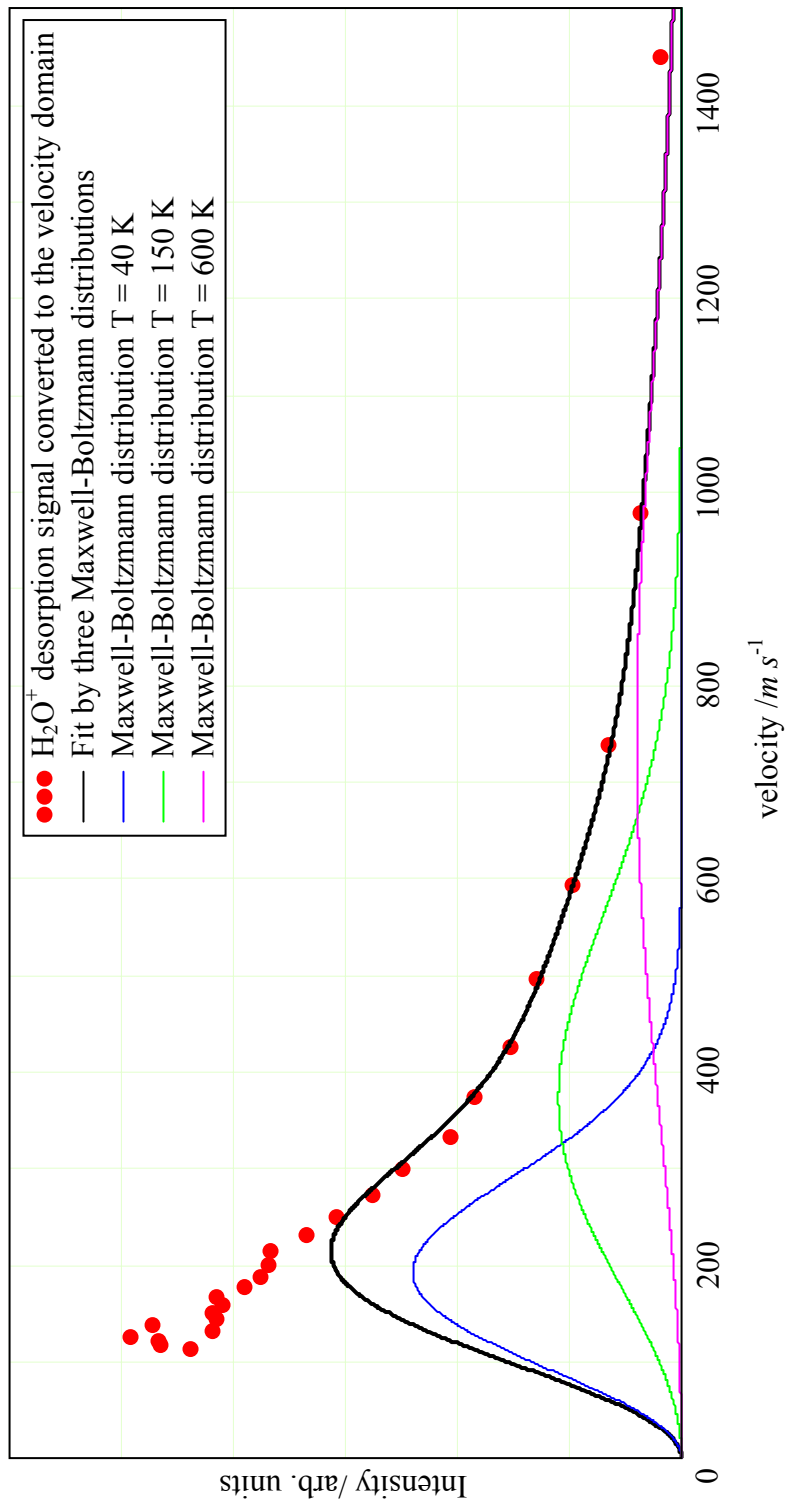


Figure 3.9 Transformation of the temporal profile shown in Figure 3.7b to the velocity domain. The water desorption signal is from pulse 1 on a 400 ML ASW film at $T \sim 100$ K. The solid black line represents the fit with a combination of three Maxwell-Boltzmann distributions at $T = 600$ K (purple), 150 K (green), and 40 K (blue).

constant and t is time. The velocity of each point was found by $v = d/t$, where d is the distance from the surface to the focusing point of the e -beam at the center of the ionizing region, $d \sim 12$ mm.

The linear combination of three Maxwell-Boltzmann distributions show that temperatures of $T = 600$ K, 150 K, and 40 K fit the experimental values. The transient times of molecules leaving the film at an initial temperature of $T = 100$ K span from fast (~ 20 μ s) to slow (~ 200 μ s) relative to the duration of the pulse (~ 10 ns) as is previously seen in the temporal profiles (Figure 3.7). The kinetic velocity for the slow components suggests that a cooling effect is responsible for the long tail in the temporal profile.

Laser induced desorption experiments for thick films have reported two desorption regimes, a fast and a slow, where the fast regime is correlated to heating of the water molecules to temperatures near their critical point, $T_c = 647$ K [26, 29]. The fast front boiling process of the desorption plume at $T = 600$ K in our experiments falls in the regime where fast heating can reach temperatures close to the critical temperature of water, T_c . The formation of water clusters is expected to occur *via* explosive boiling. This is generally considered to happen when surface temperatures reach $T_{PE} \sim 0.9T_c = 582$ K [26, 30]. Cooling by the substrate prevents the ejection of large clusters formed deep in the film. The origin of the clusters that are observed must be closer to the surface where bigger clusters ejected in the beginning are subject to further vaporization from the long nanosecond pulse. Continued cooling by the substrate during the duration of irradiation, along with molecular collisions upon expansion of the desorbed plume, decreases the translational temperature of the two colder regimes. The

Maxwell-Boltzmann distribution at the lowest temperature, $T = 40$ K, and the points not on the fit can be assumed to be influenced by the efficient thermal transport to the substrate. The desorption yield of ice is low such that a distribution is unable to fully describe any real physical processes. Further observations and discussion of the velocities of ejected material are provided in the next chapter.

In summary, the design of the Raman cell achieves a $\sim 4\%$ conversion efficiency of 1064 nm into 3424 cm^{-1} radiation. Operating the TOF-MS at high repetition rates monitors the density of the desorbed plume at the point of interaction with the e -beam as it travels through the ionization region after being ablated by infrared radiation. The focusing optimization of the S_2 radiation pulse is achieved by monitoring the changes in desorption velocities of water molecules and protonated water clusters from ASW thin films of ~ 400 ML as the focal point of the S_2 pulse nears the ASW film. The temporal evolution of the desorbing plume is transformed to the velocity domain by the use of the time-to-velocity Jacobian. Modeling of the resulting distribution in the velocity domain with a combination of Maxwell-Boltzmann distributions shows the variety and complexity for desorbing thin films where the substrate has a major effect. The three regimes shown here suggest that: one is near the critical temperature of water, dominated by the fast heating due to irradiation; the other two lower regimes are dominated by the efficient cooling of thin films by the substrate resulting in the quenching of processes deeper into the film and responsible for the long tail of the temporal profile.

3.4 Chapter References

1. N. R. Bowering, I. V. Fomenkov, D. C. Brandt, A. N. Bykanov, *et al.*, Journal of Micro-Nanolithography Mems and Moems. 8, 041504 (2009).
2. N. R. Farrar, D. C. Brandt, I. V. Fomenkov, A. I. Ershov, *et al.*, Microelectronic Engineering. 86, 509-512 (2009).
3. J. T. Walsh, T. J. Flotte, and T. F. Deutsch, Lasers in Surgery and Medicine. 9, 314-326 (1989).
4. F. E. Livingston, J. A. Smith, and S. M. George, Journal of Physical Chemistry A. 106, 6309-6318 (2002).
5. C. Focsa, B. Chazallon, and J. L. Destombes, Surface Science. 528, 189-195 (2003).
6. A. Krasnopoler and S. M. George, Journal of Physical Chemistry B. 102, 788-794 (1998).
7. F. E. Livingston, J. A. Smith, and S. M. George, Analytical Chemistry. 72, 5590-5599 (2000).
8. J. W. Williams and A. Hollaender, Physical Review. 42, 0379-0385 (1932).
9. C. V. Raman, Transactions of the Faraday Society. 25, 0781-0791 (1929).
10. K. S. Krishnan, Nature. 122, 961-962 (1928).
11. N. Bloember, American Journal of Physics. 35, 989 (1967).
12. W. R. Trutna and R. L. Byer, Applied Optics. 19, 301-312 (1980).
13. Z. P. Chu, U. N. Singh, and T. D. Wilkerson, Applied Optics. 30, 4350-4357 (1991).
14. L. Schoulepnikoff and V. Mitev, Pure and Applied Optics. 6, 277-302 (1997).
15. C. W. Wilkerson, E. Sekreta, and J. P. Reilly, Applied Optics. 30, 3855-3861 (1991).
16. A. D. Papayannis, G. N. Tsirikas, and A. A. Serafetinides, Applied Physics B- Lasers and Optics. 67, 563-568 (1998).

17. S. Malyk, *Transform and guest-host interactions in amorphous and crystalline ice*. Department of Chemistry. Los Angeles: University of Southern California (2009).
18. W. C. Wiley and I. H. McLaren, *Review of Scientific Instruments*. 26, 1150-1157 (1955).
19. F. M. Zimmermann and W. Ho, *Journal of Chemical Physics*. 100, 7700-7706 (1994).
20. F. M. Zimmermann and W. Ho, *Surface Science Reports*. 22, 127-247 (1995).
21. F. Claeysens, S. J. Henley, and M. N. R. Ashfold, *Journal of Applied Physics*. 94, 2203-2211 (2003).
22. L. V. Zhigilei and B. J. Garrison, *Applied Physics Letters*. 71, 551-553 (1997).
23. C. L. Tang, *Handbook of Optics*. 3rd ed. New York: McGraw-Hill (2009).
24. C. Focsa and J. L. Destombes, *Chemical Physics Letters*. 347, 390-396 (2001).
25. M. M. Martynyuk, *Combustion Explosion and Shock Waves*. 13, 178-191 (1977).
26. C. Mihean, M. Ziskind, B. Chazallon, C. Focsa, *et al.*, *Applied Surface Science*. 248, 238-242 (2005).
27. T. M. Orlando, A. B. Alkesandrov, and J. Herring, *Journal of Physical Chemistry B*. 107, 9370-9376 (2003).
28. P. Lorazo, L. J. Lewis, and M. Meunier, *Physical Review B*. 73, 134108 (2006).
29. K. Dreisewerd, *Chemical Reviews*. 103, 395-425 (2003).
30. A. Miotello and R. Kelly, *Applied Physics A-Materials Science & Processing*. 69, S67-S73 (1999).

Chapter 4: Amorphous Solid Water (ASW): Pulsed Ablation of ASW/CO₂ Thin Films

4.1 Introduction

It has been known for quite some time that material ablation can be achieved through the application of intense pulsed electromagnetic radiation to otherwise quiescent samples. Indeed, this is a phenomenon whose potential and proven usefulness have increased dramatically throughout the last few decades. Important applications currently abound in a number of diverse areas: medicine (*e.g.*, surgery, tissue destruction, notably cancer); materials growth and processing; cleaning; annealing; machining; analytical chemistry; nanoscience; astrophysics; and so on. Publications in the general area of laser-induced ablation are so diverse that a compendium of references given here would either be outrageously large or meaningless. Consequently, several books are listed that cover the area as a whole, [1-3] each providing an ample supply of references.

Notwithstanding the impressive technological developments, the identification and understanding of the underlying physical and chemical processes, including how they relate to one another, have proven elusive. This is hardly surprising in light of the complexity of the myriad energetic, heterogeneous, and transient environments in which ablation transpires.

Roughly speaking, starting materials can be divided into two groups: (i) covalent and ionic solids, and (ii) weakly bonded solids. The latter often involve water, whose role nearly always turns out to be subtler than anticipated. In the present paper, the

ablation of thin films comprised of either amorphous solid water (ASW) or (more often) ASW/CO₂ mixtures is examined experimentally. Pulsed infrared radiation (10 ns duration, 3424 cm⁻¹, < 2.7 mJ) excites the OH stretch vibration, which is converted to heat on a picosecond time scale [4]. The broad (and for all practical purposes structureless) OH stretch absorption features of ASW, crystalline ice, and liquid water ensure efficient photoexcitation in condensed phase samples whose character, in general, changes throughout the 10 ns pulse duration. Small water clusters, (H₂O)_{*n*}, that are produced by ablation can absorb photons from the same infrared pulse that creates them. This is subtle, as their absorption spectra differ markedly with *n* in the small-*n* regime, say, *n* ≤ 6 [5]. Note that clusters cool only by evaporation, as they are uncoupled from the substrate heat sink.

As mentioned above, the ASW/CO₂ system is important in astrophysics, *e.g.*, the outer reaches of our solar system and beyond [6-8]. It is also germane to clathrates: from the mechanisms involved in their formation, to their disruption. The most popular clathrate is that of methane [9]. However, CO₂ is also important, *e.g.*, its clathrate arises in the context of sequestration [10]. Recent research with ASW and ASW/CO₂ has attempted to determine the respective roles of sample morphology (including how it evolves as the temperature is increased), species segregation, explosive boiling (phase explosion), and other parameters [11-20]. Though a great deal has been learned it would take some imagination to judge these systems as "understood."

What sets the work reported herein apart from the majority of previous studies is the use of thin films. What is meant by "thin" in the present context is that the film

thickness is significantly smaller than the characteristic absorption depth of the incident radiation. The samples used in the present study are typically 400 monolayers (ML), corresponding to approximately 120 nm, whereas the $1/e$ absorption depth for polycrystalline ice at 3440 cm^{-1} is $\sim 800\text{ nm}$ [21]. For the 3424 cm^{-1} radiation and ASW samples used in the present study, the $1/e$ absorption depth is approximately the same, albeit slightly larger. Of course, for ASW/CO₂ films, the absorption depth is larger because the ASW is diluted by the CO₂. Thus, it is a safe assumption that the rate of energy deposition is rather uniform throughout the depth of ASW/CO₂ films of thickness, say, 400 – 500 ML.

The characteristic time for deposited energy to be removed by heat transfer to a thermally conducting substrate can be much smaller than the IR pulse duration. In the present study, the pulse duration exceeds the heat transfer time by at least an order of magnitude. This results in pronounced temperature gradients, making the film's *effective thickness* smaller than its physical thickness. In other words, despite the fact that the film absorbs radiation rather uniformly throughout its depth, the region that gives rise to water ablation is near the surface because the lower region is cooled efficiently by the substrate. This has a pronounced effect. For example, the amount of ablated material is more than an order of magnitude smaller than its counterpart from much thicker films, other things being equal [18, 21].

The use of thin films does not merely introduce novelty. Rather, it is possible to quench processes that would transpire at lower depths were thicker films are used. This can prove instrumental in furthering our understanding of the elementary processes that

transpire, *e.g.*, discerning the degree of participation of phenomena such as phase explosion and the heterogeneous nucleation of cavities [14, 22, 23]. Moreover, the use of ASW/CO₂ mixtures enables additional phenomena to be explored. For example, it will be shown that CO₂ can be liberated from much lower depths than the uppermost tens of monolayers of water that are removed with a single pulse.

Complementary, and to some extent competing, theoretical models have been put forward to reconcile the experimental observations [14, 22-32]. The ones most congruent with our perspective have used molecular dynamics (MD) simulations to explore the parameter space and phenomena [22, 29]. The groups of Garrison and Zhigilei have examined assiduously the ablation of organic solids [30-32]. They have made seminal contributions on both experimental and theoretical fronts.

Theoretical studies carried out in the group of Lewis and coworkers [22, 26, 27, 29] have likewise provided a valuable conceptual platform upon which to judge experimental results. For example, Lorazo *et al.* [26, 27] concentrated on strongly bound solids excited by short duration pulses, *e.g.*, silicon excited at 266 nm with 500 fs and 100 ps pulses. Despite the vast differences between such samples and the ASW and ASW/CO₂ systems under consideration here, we have benefited greatly from these studies, as discussed below. Likewise, Perez *et al.* [22] have examined molecular solids, which are assumed to have much larger absorption depths than the silicon system (4000 nm versus 5-10 nm, respectively), using nanosecond pulses. Again, despite important differences between the present study and the model calculations (*e.g.*, thin versus thick samples), we have benefited greatly.

In what follows, the experimental strategy and arrangement are described, including the novel application of a high repetition rate (up to 200 kHz) time-of-flight mass spectrometer (TOF-MS). This is followed by the results of a number of complementary measurements. Notably, this includes the demonstration of single infrared pulse capability. This is essential, as the application of a single infrared pulse in general induces irreversible changes throughout the sample. In other words, subsequent pulses interact with different samples than does the first pulse.

In the Discussion section, it is pointed out that segregation occurs in which CO₂ is released preferentially to H₂O. It is argued that phase explosion is, for the most part, quenched by the efficient removal of heat by the MgO substrate. As a result of this cooling, species that enter the gas phase do so in a sparse plume that is dominated by monomers and small water clusters that arise from what has been referred to as trivial fragmentation [25].

4.2 Experimental

The ablation of ASW and co-deposited ASW/CO₂ films has been studied experimentally using the arrangement shown schematically in Figure 4.1. The experiments have been carried out in an ultrahigh vacuum (UHV) chamber (base pressure 10⁻¹⁰ Torr) using a pulsed 3424 cm⁻¹ radiation source and a time-of-flight mass spectrometer (TOF-MS). The three-tier UHV chamber has been described previously in detail [11, 13, 16]. It is equipped for Fourier transform infrared (FTIR) spectroscopy,

temperature programmed desorption (TPD) [11], and the laser-initiated ablation experiments reported herein. The arrangement indicated in Figure 4.1 is discussed below.

A MgO(100) substrate was attached to a copper holder mounted at the end of a custom-made liquid nitrogen cooled cold finger cryostat (McAllister Technical Services). The MgO crystals (MTI Corporation) were cleaved on both sides in a dry nitrogen atmosphere, exposing (100) surfaces, and transferred immediately into the vacuum chamber. Typical dimensions of the MgO substrate were 1 mm × 10 mm × 10 mm. After the chamber reached the base pressure, the substrate was annealed to ~ 600 K in oxygen to remove oxygen vacancies and contaminants [11, 33].

A surface holder that had been used previously for FTIR and TPD experiments [13, 16] was modified to reduce thermal gradients across the substrate. Specifically, the substrate was attached to a thin copper plate (14 mm × 10 mm × 0.3 mm) and secured by folding the edges of the plate over it. A centered square opening (5 mm × 5 mm) was cut in the copper plate to allow transmission of the infrared radiation. The surface holder was attached to one of two electrically isolated copper blocks mounted on the cryostat cold finger. The cryostat design included the capability of x , y , and z translation and 360° rotation. Substrate temperatures down to ~ 100 K were achieved with liquid nitrogen alone and down to ~ 90 K by bubbling helium gas through the liquid nitrogen. The sample was resistively heated using a tantalum wire surrounded by ceramic sleeves cemented onto the back of the copper plate with a ceramic adhesive

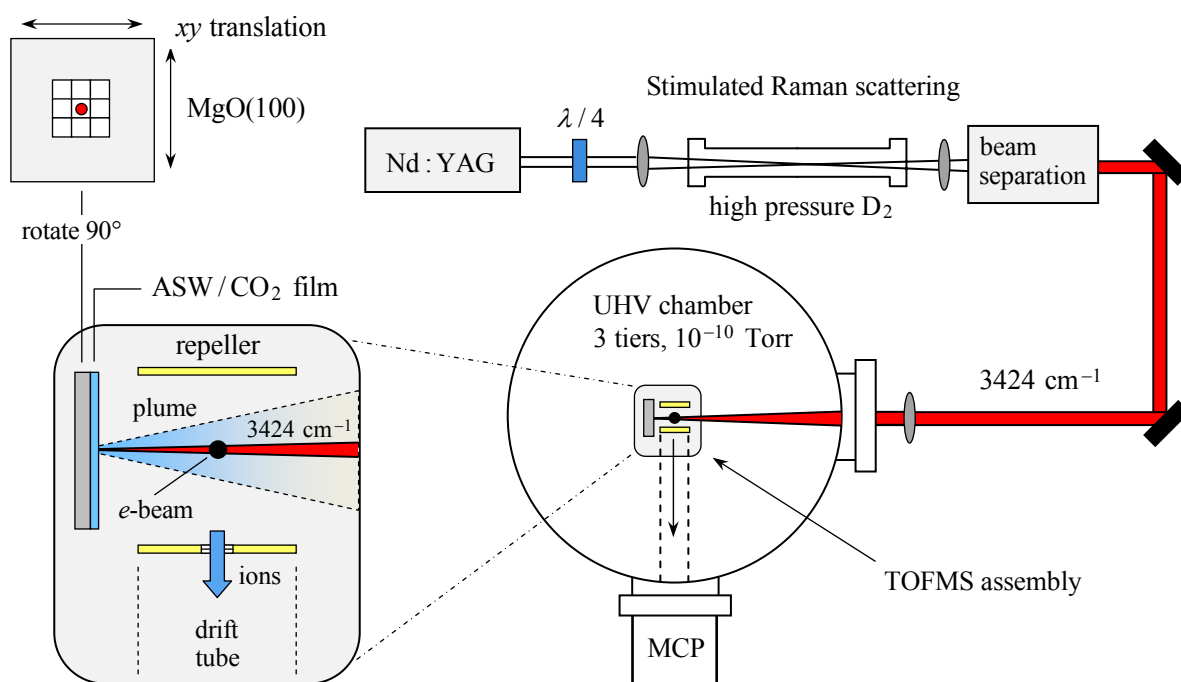


Figure 4.1 The UHV chamber is equipped with TOF-MS, FTIR, Auger, and TPD diagnostics. The TOF-MS arrangement is indicated schematically. The second Stokes line from stimulated Raman scattering in high-pressure D_2 gas (3424 cm^{-1}) excites the sample at normal incidence causing material to enter the gas phase. The electron beam (black dot) of the TOF-MS is brought to a focus 12 mm from the surface. It operates at repetition rates up to 200 kHz. Samples are irradiated in the nine areas indicated on the upper left (white squares) in order to achieve signal averaging while maintaining single-pulse conditions.

(Aremco 569). A chromel-alumel thermocouple was cemented directly to the substrate on the side opposite the copper block.

After the substrate was cooled to ~ 90 K, porous ASW and ASW/CO₂ films were grown by using background dosing. The dosing time was established using deposition rates that had been determined previously by comparing the integrated TPD intensity of a water film with that of a water monolayer [16]. Optima LC/MS-grade water (Fisher Scientific) was degassed by several freeze-pump-thaw cycles. H₂O and CO₂ (Gilmore Liquid Air, 99.99%) were introduced independently through precision leak valves. In this co-deposition mode, CO₂ molecules were embedded in the porous ASW film during its growth. Depending on substrate temperature, CO₂ sometimes aggregated on top of the film. The film was annealed at 112 K and then cooled to 90 K to remove any CO₂ that might have accumulated on top of the film, leaving only CO₂ trapped within the film [13].

In the experiments reported herein H₂O:CO₂ ratios of 4:1 and 3:1 were used. Such ratios are taken as upper limits in the sense that some of the deposited CO₂ may well re-enter the gas phase during a deposition cycle, and some of it finds its way to the surface, where it is removed at 112 K. We shall continue to refer to deposited samples using nomenclature such as 4:1, but with this caveat in mind. There is no reason to believe that the embedded CO₂ retains a Poisson nearest-neighbor spacing distribution. It is more likely that the deposited CO₂ is present to a significant extent in CO₂-containing pockets following sample preparation. For example, if one considers the nearest-neighbor statistics for high concentrations such as 25%, it is simply not possible to have a preponderance of CO₂ monomer.

The IR radiation was generated by using stimulated Raman scattering (SRS) in D₂ ($\nu = 2987 \text{ cm}^{-1}$) of the fundamental laser line (1064 nm) of a Q-switched Nd:YAG laser (Continuum NY81C, 800 mJ, 10 ns) operating at 10 Hz. Circularly polarized Nd:YAG laser radiation was directed into a 1.1 meter long cell filled with D₂ gas to a pressure of approximately 60 atm, resulting in $\sim 4\%$ photon conversion efficiency for second Stokes radiation, S₂ (3424 cm^{-1}). To minimize gas degradation, laser energy fluctuations, and window damage in the Raman cell, the 1064 nm pump energy was limited to $< 185 \text{ mJ}$, resulting in maximum S₂ energies of approximately 2.7 mJ [12]. The laser and second Stokes energies were monitored using a calibrated pyroelectric meter (Ophir) and/or a liquid nitrogen cooled, fast MCT detector (Cincinnati Electronics).

The various Stokes lines generated by SRS were separated using a 60° CaF₂ prism, such that only the S₂ radiation entered the UHV chamber through a CaF₂ window. The S₂ energy was attenuated with a set of microscope slides (Corning Inc.) calibrated by us. Prior to entering the chamber, the S₂ radiation repetition rate was reduced to 1 Hz by using a chopper (ThorLabs MC1000). It was focused with a 50 cm focal length CaF₂ lens to a diameter ($1/e$, near-Gaussian) of $\sim 0.5 \text{ mm}$ at the substrate.

Referring to Figure 4.1, the substrate was centered at the entry to the 0.5 m drift tube of the TOF-MS. The IR radiation was aligned such that its propagation vector \mathbf{k} was normal to the surface and orthogonal to the drift tube axis. The centermost region of the ejected plume propagated toward the center of the extraction plates (*i.e.*, in the direction of the incoming laser beam) where it was ionized with electrons having a mean energy of 70 eV. The electron beam was focused to a waist 12 mm from the surface. Ions were

pulse-extracted at 100 kHz. In other words, mass spectra were recorded at 10 μ s intervals. Signals persisted for as long as 300 μ s after the laser firing. This yielded the temporal evolution of the plume following a single IR pulse.

In order to carry out a number of single-pulse experiments on the same thin film, the focal point of the incident radiation was moved from one point to the next on the surface with each laser firing. A distance of \sim 1 mm between spots was sufficient to isolate results of different experiments on a single film because the film thickness (\sim 0.1 μ m) was much smaller than the focused IR diameter of \sim 0.5 mm. The deposited energy was rapidly transferred to the substrate, which was maintained at \sim 90 K, as opposed to lateral heat transfer to adjacent ASW. Note that ASW is a poor thermal conductor relative to crystalline MgO, or any of the 14 crystalline forms of ice [34]. To prevent irradiation of the surface holder, the innermost 3 mm \times 3 mm area was used (see inset in Figure 4.1). This allowed 9 experiments to be carried out with a single deposition.

Temporal profiles were recorded using a fast amplifier (SRS D-300 MHz) connected to an analog-to-digital converter (Gage CS 8500, 8 bit, 512k samples) with 2 ns resolution. Data processing and analyses were carried out using LabView programs (National Instruments) written for our specific experiments. Typically, the final spectrum consisted of the sum of "single-pulse TOF spectra" from the nine different spots on the substrate.

4.3 Results

The interaction of infrared radiation with amorphous thin film samples comprised of H₂O and CO₂ has been studied under both single-pulse and multiple-pulse conditions using the arrangement indicated in Figure 4.1. The IR frequency (3424 cm⁻¹) is slightly higher than the center of the broad absorption feature of the OH stretch fundamental in ASW [13, 16]. It nonetheless lies well within the roughly 400 cm⁻¹ full width at half maximum (FWHM) of this broad feature. The experimental results consist mainly of TOF mass spectra of the ejected plume of gaseous molecules and clusters following irradiation by single IR pulses. Irradiation using multiple pulses incident on the same spot is used mainly to underscore the virtue of achieving single-pulse capability.

Gas mixtures of H₂O and CO₂ were co-deposited on the MgO(100) surface at ~ 90 K in order to form porous ASW films with embedded CO₂ [13, 16]. As mentioned above, the films were annealed to approximately 112 K to remove surface-bound CO₂, and they were then cooled back to ~ 90 K. Films of 400 and 500 monolayers (ML) were used in the present study. Incident IR radiation is absorbed by the ASW, and the initial OH stretch excitation thus created is degraded rapidly to heat, *i.e.*, on a picosecond time scale [4, 35]. Heat is transported to the crystalline substrate on a time scale that is much shorter than the laser pulse duration. This relatively rapid heat transfer to the substrate eliminates, for all practical purposes, the possibility of material release into the gas phase following cessation of the IR pulse.

Referring to Figure 4.2, each panel (20 – 240 μs) displays the temporal evolution of the plume through a sequence of mass spectra recorded following a single laser firing.

The panels are normalized with respect to one another. Pronounced peaks are due to H_2O^+ ($m/e = 18$, black) and CO_2^+ ($m/e = 44$, red). Ions produced by the electron gun are extracted at a repetition rate of 100 kHz. In other words, the data shown in Figure 4.2 are comprised of series of mass spectra separated by 10 μs intervals. These series continue for the duration of the ejected plume, *i.e.*, $> 200 \mu\text{s}$ for the examples shown in Figure 4.2.

Columns (a) and (b) of Figure 4.2 show results for two series of consecutive pulses incident on the same substrate spot under different experimental conditions. The first pulse in each series (pulse 1) corresponds to the irradiation of an ASW/ CO_2 mixture having the original composition and morphology. Subsequent pulses probe films that have been modified as a consequence of the heat generated by irradiation with previous pulses. The two series in (a) and (b) show that even for low energy irradiation (*i.e.*, 1.0 and 1.2 mJ, respectively) sufficient thermal energy is implanted to disrupt the ASW host matrix, allowing CO_2 molecules to escape into the gas phase. At these energies water removal is less efficient for pulse 1. Referring to Figure 4.2c, no appreciable difference in its signal intensity was observed up to at least the first 10 pulses. On the other hand, embedded CO_2 is depleted significantly within the first 4 – 5 pulses for energies ~ 1 mJ, and as early as pulse 3 for 2.4 mJ (not shown). Figures 4.2a and b have initial $\text{H}_2\text{O}:\text{CO}_2$ concentration ratios of 4:1 and 3:1, respectively. Taking into account the higher ionization efficiency of CO_2 relative to H_2O and the fact that most of the H_2O^+ signal (black) derives from water monomer, we estimate that the amount of on-axis CO_2 in the plume liberated after the first pulse is larger than that of H_2O by factors of ~ 7 and ~ 2 in Figures 4.2a and b, respectively. For comparison,

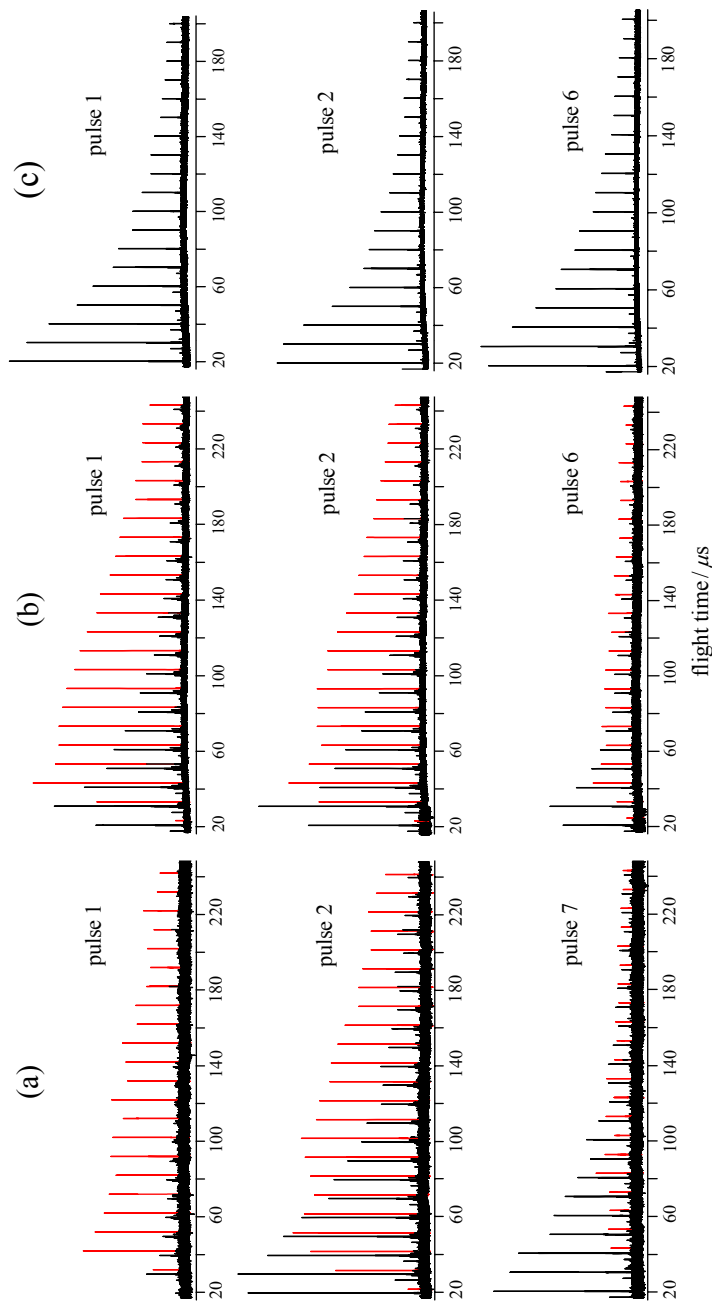


Figure 4.2 The TOF-MS is operating at 100 kHz, *i.e.*, spectra are recorded every 10 μs (see Figs. 4 and 5 for individual spectra). (a) 500 ML (20% CO_2), 1.0 mJ: The first laser pulse liberates much more CO_2 than H_2O . The second laser pulse liberates comparable amounts of CO_2 and H_2O . Pulse 7 liberates more H_2O than CO_2 . Keep in mind that the $\text{H}_2\text{O}:\text{CO}_2$ ratio for deposited material is 4:1. (b) 400 ML (25% CO_2), 1.2 mJ: The same general trend as in (a) is observed, though less dramatic. (c) 400 ML of H_2O (*i.e.*, no CO_2), 1.2 mJ.

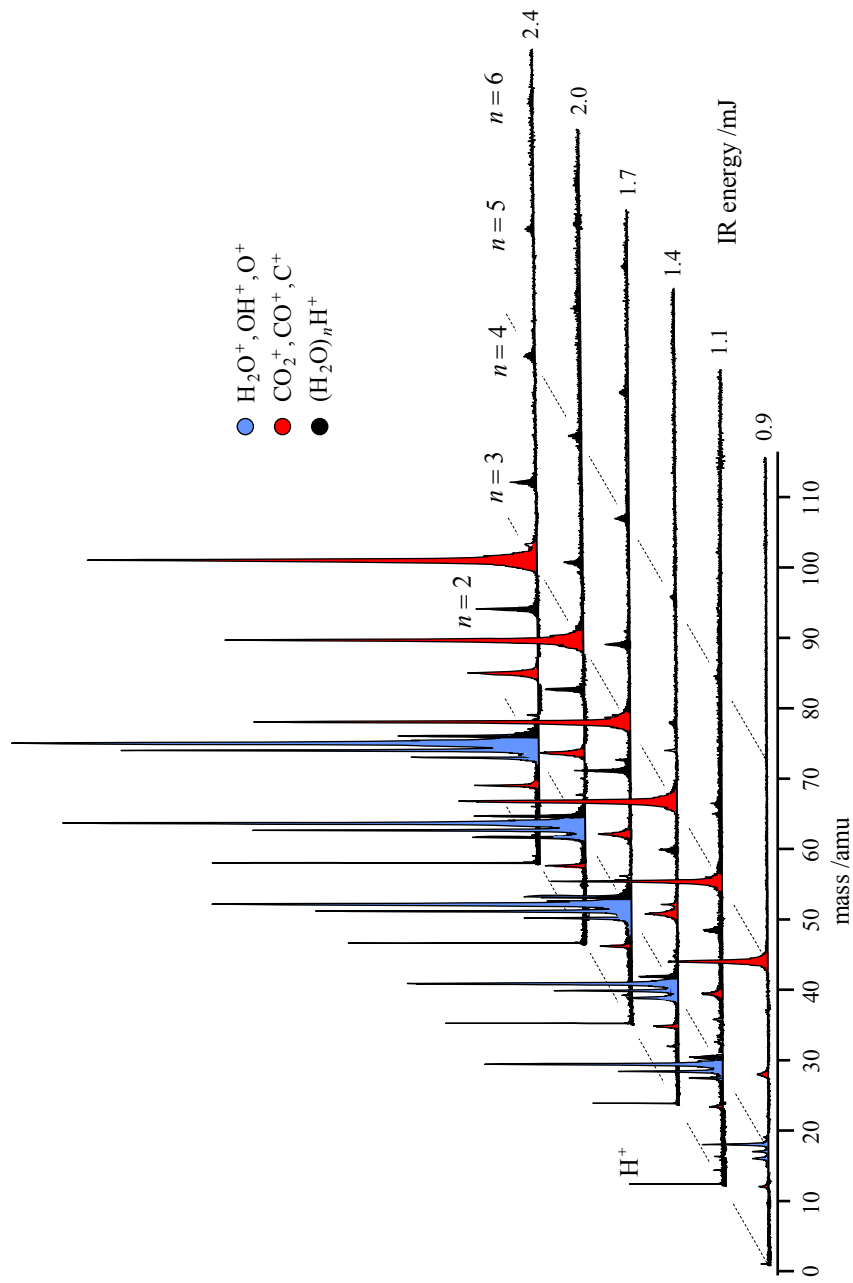


Figure 4.3 Mass spectra obtained under single-pulse conditions (400 ML, 25% CO_2) are presented for different IR energies. Peaks that derive from CO_2 , monomer H_2O , and H_2O clusters are color-coded (red, blue, and black, respectively). Though some of the blue signal undoubtedly arises from H_2O clusters, these contributions are small. The single-pulse data shown here were obtained by summing contributions from the first three extractions (*i.e.*, mass spectra) for each of the squares indicated in Figure 4.1.

Figure 4.2c displays the evolution of the plume from a film containing no CO₂ following irradiation with 1.2 mJ.

To demonstrate the presence of clustered material in the plume following irradiation of ASW/CO₂ films, the IR energy was varied throughout the range 0.9 – 2.4 mJ. Figure 4.3 shows mass spectra obtained under single-pulse conditions, but with signal averaging. To achieve signal averaging while maintaining single-shot conditions, we begin by summing the first three consecutive mass spectra recorded following a single pulse. This is then carried out for each of the 9 spots indicated on the upper left of Figure 4.1, and the data from these 9 spots are summed. Thus, data from 27 mass spectra are averaged, while maintaining single-pulse conditions.

Signals from protonated water clusters, (H₂O)_nH⁺ with n up to 9 have been observed (*vide infra*, Figure 4.5), as discussed below. Were the release of material into the gas phase is nothing more than evaporation at a well defined temperature, it would result in the release of H₂O and CO₂ monomers. The presence of clusters is in accord with the trivial fragmentation mechanism discussed by Perez *et al.* [22] and in the recent review by Lewis *et al.* [25]. Referring to Figure 4.3, signals due to H₂O monomer (blue), CO₂ (red), and H₂O-clusters (black) begin to appear at energies higher than ~ 0.9 mJ. At energies higher than 1.7 mJ, protonated water clusters with $n > 2$ are easily detected.

An expanded view of the H₂O cluster signals is shown in Figure 4.4, which displays results recorded after irradiating ASW/CO₂ mixtures with 2.4 mJ. Note that in this mass spectrum the H₂O⁺ and CO₂⁺ peaks are off-scale. Neutral [36] and even

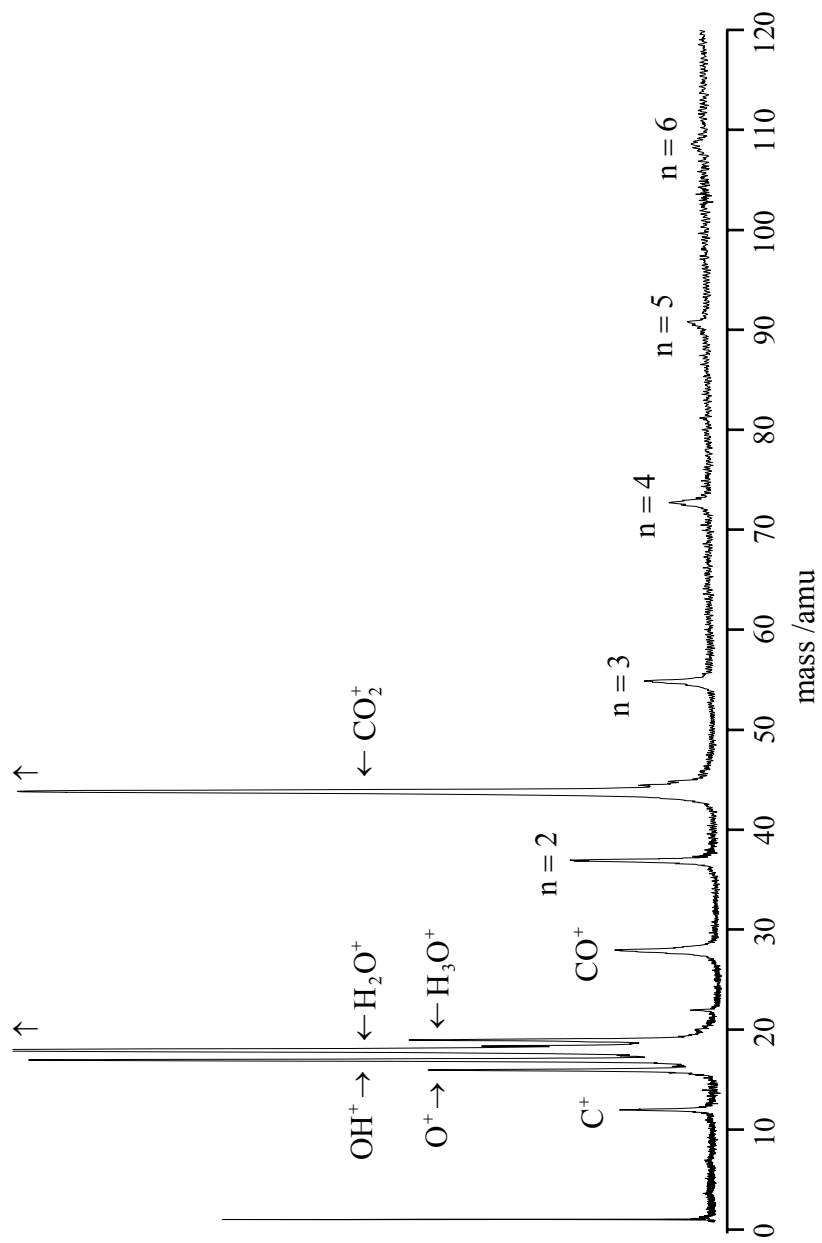


Figure 4.4 This spectrum highlights the presence of protonated water cluster ions. Note that the H_2O^+ and CO_2^+ peaks are off-scale. Conditions: 400 ML (25% CO_2), 2.4 mJ, average of 9 spots, 3 extractions for each spot.

ionized [19] clusters have been observed previously under high infrared fluence conditions. Such experiments display a variety of cluster sizes with a distribution that depends on irradiation conditions and detection methods. Our experiments show no evidence of ionized clusters. Only neutral clusters are produced, either with pure ASW or with ASW/CO₂ mixtures.

4.4 Discussion

4.4.1 Overview

Processes such as morphological change, phase transitions, transport and segregation of host and guest species, and heat flow in multi-component molecular solids have been, and remain, central to a broad range of scientifically and technologically important areas and related phenomena. Raising the temperature of a solid material by means of the absorption of pulsed radiation has matured as a means of furthering our understanding of the participating physical processes, as well as offering a broad range of opportunities in applied science. The present study focuses on pulsed ablation in ASW and ASW/CO₂ thin films (400 and 500 ML) atop a good thermal conductor, MgO(100). The above-mentioned processes have been studied in detail both theoretically and experimentally by a number of groups. Though most of the theoretical studies have focused on strongly bound solids, a number have addressed issues germane to molecular solids [14, 30-32] and, specifically, ASW and doped ASW films [34, 37-39]. Healthy debate notwithstanding, a reasonably coherent picture has emerged concerning the vigorous molecular-level activity that follows the pulsed excitation of solid materials

[22, 24, 25, 27]. We shall take the most recent papers from the group of Lewis and coworkers [22, 26, 27, 29] as providing up-to-date summaries of previous work, particularly the status of theoretical modeling, with the understanding that some fundamental points remain contested. Our position is congruent with a main theme of their work: molecular dynamics (MD) simulations capture the essence of the relevant physical processes. The perspective afforded by non-equilibrium thermodynamics, as valuable as it is in its own right, is enhanced through the graphic illustrations provided by the MD simulations.

The long (10 ns) pulse duration of the 3424 cm^{-1} radiation used in the present study makes it, for all practical purposes, impossible to separate temporally the deposition of OH-stretch vibrational excitation (which is rapidly converted to heat) from the resulting transport, segregation, ablation, etc. processes. Careful theoretical modeling of a relatively simple system (*i.e.*, silicon), using 266 nm pulses of duration 500 fs [27], 100 ps [27], and even longer [22], reveals regimes where ablation takes place. The samples examined in these simulations are thicker than the ones used in the present study in the sense that the distance over which radiation is absorbed is much smaller than the sample thickness, which is opposite our case.

In modeling silicon, short pulses such as 500 fs result in the deposition of energy on a time scale that is short relative to that of the subsequent dynamics. The topmost silicon layers are ejected into the gas phase, mainly as monomer, but with some small clusters appearing as well. Larger clusters emerge from lower depths via phase explosion. At the lowest depths, large voids appear and a liquid shell of material is

released from the sample [27]. This amazing phenomenon is in agreement with experimental observations of transient interference fringes following pulsed irradiation [40, 41]. On the other hand, in the nanosecond regime phase explosion is suppressed to a large extent, though it can still occur if there is sufficient inertial confinement [22].

As mentioned above, the ASW and ASW/CO₂ films used in the present study are substantially thinner than the silicon samples used in the theoretical simulations of Lewis and coworkers [22, 27]. Consequently, in the present study, heat flow to the substrate plays a major role. It is difficult to estimate a characteristic time for this heat transfer, given ASW's mysterious nature. Whereas crystalline MgO has well-defined, high thermal conductivity, the thermal conductivity of ASW is less than that of hexagonal and cubic ices [34].

If we take as a figure of merit one-half the film thickness d divided by the speed of sound v (*i.e.*, $\tau = d/2v$), and use $d = 100$ nm and $v = 500$ m s⁻¹, a resulting τ value of 100 ps is obtained. This is the time needed for a packet of acoustic phonons to move from the middle of the film to the substrate. It is much smaller than the 10 ns pulse duration. Alternatively, the time required for heat to diffuse from the middle of the film to the substrate is given by $\tau_{diff} = (d/2)^2 / 4D$, where D is the thermal diffusion coefficient [21]. Using the 273 K value of D suggested by Livingston *et al.* gives $\tau_{diff} \sim 500$ ps. Accounting for the larger value of D at lower temperatures (say, 150 – 200 K) this would drop by a factor of roughly two. In any case, heat transfer occurs on a time scale that is short relative to the laser pulse duration. On the basis of these crude estimates, we conclude that heat is removed efficiently by the substrate, and both phase explosion and

the heterogeneous nucleation of cavities are, to a large extent, quenched. In this regime, neutral clusters that emanate from the irradiated sample are of modest size, as expected on the basis of the trivial fragmentation mechanism [26, 27].

The existence of clustered material in the plume has been interpreted in a number of studies as a signature of phase explosion having taken place [8, 22, 24, 27, 36, 42, 43]. Under the present experimental conditions, though there may be some degree of explosive boiling, there is no reason to invoke phase explosion as a mechanism that plays an important role. When the present study commenced, we believed that increasing the laser fluence would result in the release of larger clusters as the system approached the phase explosion regime. It now seems that this is not the case. As the fluence is increased, irradiation of the topmost layers decomposes the material entering the gas phase into smaller units. This pushes the transition region between small species (monomers plus small water clusters) and larger clustered species to lower depths. At the same time, efficient heat removal by the substrate quenches these lower levels, thwarting the ejection of larger clusters.

It is noteworthy that irradiation of the same spot with successive pulses continues to yield gas phase product. The composition of the material that enters the gas phase changes with continued irradiation, specifically, the H₂O:CO₂ ratio increases. With the first few IR pulses, this change can be dramatic, as indicated in Figure 4.2a, pulses 1 and 7. Often it is less dramatic, as indicated in Figure 4.2b. However, the propensity to emit, with the first few pulses, a larger percentage of the CO₂ than is present in the freshly prepared film is robust. It has been observed in all of the experiments.

Even after ten or more pulses have been incident on the same spot, material is still ejected into the gas phase. In comparison, Livingston *et al.* [21] used comparable fluence, comparable photon energy, and even longer pulse durations. However, they used significantly thicker samples, *i.e.*, typically one to two orders of magnitude thicker than ours. The amount of material removed with a single pulse was ~ 600 nm. This exceeds by a factor of several the entire thickness of our samples, in stark contrast to the much smaller amount of material removed in the experiments reported herein. This difference is due to efficient cooling by the substrate.

4.4.2 Segregation

Now consider laser-induced segregation between water and CO₂. Because the samples are highly metastable, initiating segregation is easy, as it is energetically downhill. Our deposition temperature of 90 K is higher than the deposition temperatures used by Öberg *et al.*, who examined morphological changes throughout the range 25 – 70 K [17]. In the present study, we are blind to processes that transpire at these lower temperatures. Our samples might resemble those of Öberg *et al.* after they have increased the temperature to 70 K, *i.e.*, the highest temperature reported in their study. However, it is known that morphology is a sensitive function of sample preparation [44], so we leave open the relationship between our samples and those of Öberg *et al.*

The pulsed infrared radiation excites OH-stretch vibrations, which are degraded to heat on a picosecond time scale. Whatever temperature rise accrues (and despite its spatial variation and transient nature), it promotes segregation. Namely, metastable

ASW/CO₂ gives way to a more fully hydrogen-bonded network with concomitant release of CO₂.

The stability of the hydrogen-bonded water network (*i.e.*, with CO₂ contained in pockets or released into the gas phase) promotes the preferential release of CO₂ at modest levels of laser-induced agitation. A striking example is given in Figure 4.2a, where the majority of the released material is CO₂. Relatively little H₂O is released despite the fact that the H₂O:CO₂ ratio is 4:1 in the deposited sample. Figure 4.2a is extreme, but the propensity for preferential CO₂ release is robust. It has been observed in all of the experiments carried out in this study. There is no way to reconcile such behavior without invoking respective bonding stability.

On rare occasions, larger numbers of small protonated water cluster ions have been observed, both in pure ASW and mixed ASW/CO₂ samples. Figure 4.5 shows a mass spectrum for one such case. Though interesting, we do not yet have an explanation.

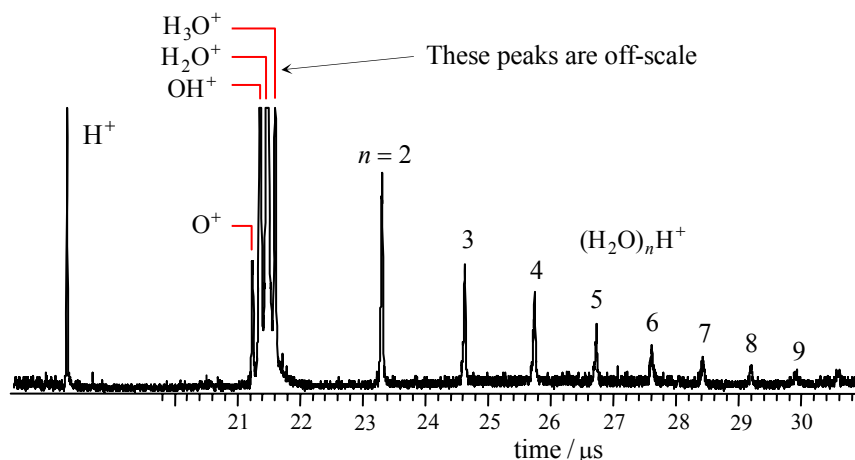


Figure 4.5 On rare occasions, large cluster signals are observed, *e.g.*, compare this single-shot spectrum to the one in Figure 4.4. The sample is 400 ML of ASW (*i.e.*, no CO₂). The IR energy is 1.7 mJ.

Whether such behavior is a signature of incipient phase explosion will be examined in the future.

4.4.3 Material Removal

We do not know the size distribution of the neutral water clusters that give rise to the protonated water cluster ions. However, in light of the efficient cooling brought about by the substrate, there is no reason to expect large clusters to be present in the plume [14, 25, 27, 31, 36]. On the contrary, modeling studies using thicker samples and shorter excitation pulses indicate that large clusters are formed well below the surface, with small clusters emanating from closer to the surface [27]. In the present experiments, efficient cooling by the substrate quenches the removal of material from far below the surface. With ASW samples, the fact that only a small amount of material is removed with each pulse is evidence that whatever happens below, say, several tens of monolayers does not result in material from this region entering the gas phase. Of course with ASW/CO₂ samples, CO₂ is released from further down.

Another process that reduces cluster size is the photoexcitation of clusters that enter the gas phase during a given infrared pulse and are still exposed to the radiation for the remainder of the pulse. In other words, suppose a cluster enters the gas phase within the first few ns of the 10 ns IR pulse duration. It is free to absorb photons for the remainder of the pulse. This will result in evaporation of H₂O molecules, causing the clusters to become smaller. This effect is convoluted with the blue shifts of the absorption spectra of clustered H₂O as the clusters get smaller. Consequently, laser-

induced cluster shrinkage will slow or even truncate because the absorption cross section becomes too small. Note that 3424 cm^{-1} lies on the high frequency side of the peak of the broad ASW absorption spectrum, whereas it lies on the low frequency side of the absorption spectra of small H_2O clusters [5, 21, 45].

In the work reported here, the amount of material that enters the gas phase is small compared to any of the results reported in the theoretical studies. In the latter, material is entrained such that different species assume the same forward (plume) velocity [14, 30-32]. We observe no such entrainment. Indeed, referring to Figure 4.2, it is clear that CO_2 and H_2O each have different velocity distributions.

The *extremely conservative* assumption that nothing is emitted into the gas phase after $1\ \mu\text{s}$ enables a speed distribution in the direction of the surface normal to be obtained using the data in Figure 4.2. In other words, efficient cooling of the film by the substrate ensures that nothing leaves the surface on the time scale of Figure 4.2. Though $1\ \mu\text{s}$ is short on the scale of Figure 4.2, it is very much longer than the τ and τ_{diff} values discussed earlier. Consequently, the assumption that material does not leave the surface after $1\ \mu\text{s}$ is safe, in the extreme. Figure 4.6 shows the resulting H_2O and CO_2 distributions obtained using the data in Figure 4.2b.

The significance of Figure 4.6 is that the amount of emitted material and the time interval over which it is emitted are such that H_2O and CO_2 do not assume a common speed along the plume axis. In other words, there is insufficient density to support an expansion of the kind seen in the theoretical studies of Lorazo *et al.* [26, 27]. This is in accord with our observation that a modest amount of material enters the gas phase as a

consequence of a single IR pulse. It also underscores the efficacy of the detection arrangement. Clearly, with thicker samples significantly higher single-shot S/N will be obtained. This has been verified in preliminary experiments in our laboratory and will be discussed at a later time.

It was noted earlier (Figure 4.2 and the surrounding discussion) that pulses of ~ 1 mJ liberated approximately the same amount of H_2O per pulse from pure ASW samples up to at least the tenth pulse. In this case, because the sample contains 400 ML of H_2O , less than 40 ML of H_2O is liberated per pulse. This upper bound is conservative—unreasonably so. If we examine further the respective amounts of on-axis CO_2 and H_2O , it is possible to obtain a smaller upper bound.

The amount of deposited CO_2 is ~ 100 ML in each of the ASW/ CO_2 samples used in the present study. Signals for CO_2 go to ~ 0 before pulse number 10. Assuming that all of the deposited CO_2 is released through the application of successive pulses, the amount of H_2O released per pulse can be estimated. Specifically, by using the 70 eV cracking patterns and the respective ionization cross sections, the amount of H_2O per pulse can be obtained. When this is carried out for columns (a) and (b) in Figure 4.2, it is found that 10 – 20 ML of H_2O are emitted into the gas phase with each pulse. The bottom line is that 10 ns pulses applied to samples of 400 – 500 ML remove only a small amount of water (10 – 20 ML) per pulse because of the efficient cooling by the substrate.

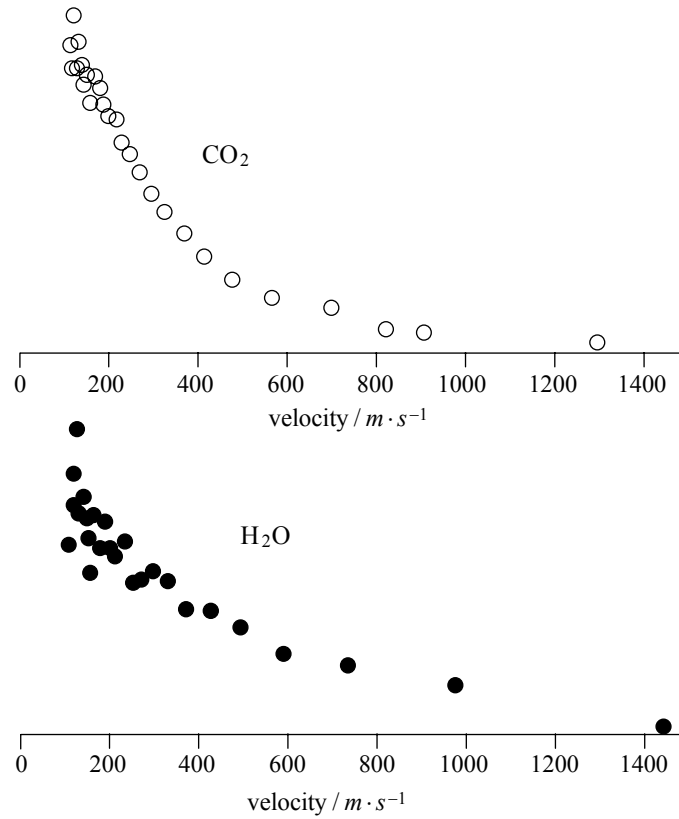


Figure 4.6 The data from Figure 4.2b, pulse 1 were converted from the time domain to the (on axis) velocity domain using the standard time-to-velocity Jacobian. Ablated CO₂ clearly travels more slowly than H₂O.

4.5 Summary

The above results and conclusions are summarized below, including comments about their significance and where we envision the work going in the near future.

- (1) Combining pulsed laser ablation with a high repetition rate (up to 200 kHz) time-of-flight mass spectrometer provides unique opportunities for studying thin films of ASW and doped ASW. Good S/N is achieved following irradiation with a single 3424 cm^{-1} pulse that excites the OH stretch vibration. This excitation is converted to heat on a picosecond time scale. Typically, individual TOF spectra spaced by $10\text{ }\mu\text{s}$ are recorded for $> 200\text{ }\mu\text{s}$ following single-pulse excitation. Single-pulse capability is essential, as the first pulse can alter the sample irreversibly, *e.g.*, endowing it with more crystalline character. Change is especially apparent with ASW/CO₂, where the first pulse alters dramatically the composition. Signal averaging is achieved by translating the substrate laterally to ensure that a fresh sample is exposed to each pulse.
- (2) For ASW:CO₂ samples deposited in 3:1 and 4:1 ratios, the release of material into the gas phase through the absorption of 3424 cm^{-1} photons is hardly surprising considering the high degree of metastability of the samples. In an earlier study, it was shown that a modest amount of CO₂ remains embedded in the water host as the temperature is raised from 90 K to 180 K (temperature programmed desorption), at which point all of the water is removed [13]. The CO₂ that remains as the temperature approaches 180 K

may be present in clathrate-type cages [46]. Analogous studies with ASW:CH₄, which is important because of its relationship to methane clathrate [9], will be carried out in the near future to achieve a better understanding of clathrate-type caging dynamics.

- (3) Small protonated water clusters are observed in the mass spectra. The size distribution of the neutral precursors is not known, though it is unlikely that significantly larger neutral clusters are involved. The presence of small clusters in the ejected plume is interpreted as evidence of the trivial fragmentation nature of the ablation, in which phase explosion is suppressed. On rare occasions cluster signals are substantial, which may reflect incipient phase explosion.
- (4) Thin films atop a crystalline MgO substrate are cooled through efficient heat transfer to the substrate that takes place concomitantly with irradiation. Consequently, many laser-induced processes that would transpire in thicker samples well below the surface (say hundreds of ML) are quenched — specifically, phase explosion and fragmentation via the heterogeneous nucleation of voids.

4.6 Chapter References

1. *Laser Ablation and Desorption*. Experimental Methods in the Physical Sciences, ed. J.C. Miller and R.F. Haglund. Vol. 30: Academic Press (1998).
2. *Laser-Induced Breakdown Spectroscopy*, ed. J.P. Singh and S.N. Thakur: Elsevier B.V. (2007).
3. C. R. Phipps, *Laser Ablation and its Applications*: Springer Science+Business Media LLC (2007).
4. J. J. Loparo, S. T. Roberts, and A. Tokmakoff, *Journal of Chemical Physics*. 125, 194521 (2006).
5. J. B. Paul, C. P. Collier, R. J. Saykally, J. J. Scherer, *et al.*, *Journal of Physical Chemistry A*. 101, 5211-5214 (1997).
6. P. Ehrenfreund, E. Dartois, K. Demyk, and L. d'Hendecourt, *Astronomy & Astrophysics*. 339, L17-L20 (1998).
7. P. Ehrenfreund, O. Kerkhof, W. A. Schutte, A. C. A. Boogert, *et al.*, *Astronomy & Astrophysics*. 350, 240-253 (1999).
8. J. D. Thrower, D. J. Burke, M. P. Collings, A. Dawes, *et al.*, *Astrophysical Journal*. 673, 1233-1239 (2008).
9. E. D. Sloan, *Nature*. 426, 353-359 (2003).
10. P. Dornan, S. Alavi, and T. K. Woo, *The Journal of Chemical Physics*. 127, 124510 (2007).
11. S. Hawkins, G. Kumi, S. Malyk, H. Reisler, *et al.*, *Chemical Physics Letters*. 404, 19-24 (2005).
12. S. Malyk, *Transform and guest-host interactions in amorphous and crystalline ice*. Department of Chemistry. Los Angeles: University of Southern California (2009).
13. S. Malyk, G. Kumi, H. Reisler, and C. Wittig, *Journal of Physical Chemistry A*. 111, 13365-13370 (2007).
14. L. V. Zhigilei, *Applied Physics A-Materials Science & Processing*. 76, 339-350 (2003).

15. R. Hodyss, P. V. Johnson, G. E. Orzechowska, J. D. Goguen, *et al.*, *Icarus*. 194, 836-842 (2008).
16. G. Kumi, S. Malyk, S. Hawkins, H. Reisler, *et al.*, *Journal of Physical Chemistry A*. 110, 2097-2105 (2006).
17. K. I. Oberg, E. C. Fayolle, H. M. Cuppen, E. F. van Dishoeck, *et al.*, *Astronomy & Astrophysics*. 496, 281-293 (2009).
18. F. E. Livingston, J. A. Smith, and S. M. George, *Journal of Physical Chemistry A*. 106, 6309-6318 (2002).
19. C. Focsa, B. Chazallon, and J. L. Destombes, *Surface Science*. 528, 189-195 (2003).
20. C. Mihean, M. Ziskind, B. Chazallon, E. Therssen, *et al.*, *Applied Surface Science*. 253, 1090-1094 (2006).
21. F. E. Livingston, J. A. Smith, and S. M. George, *Analytical Chemistry*. 72, 5590-5599 (2000).
22. D. Perez, L. J. Lewis, P. Lorazo, and M. Meunier, *Applied Physics Letters*. 89 (2006).
23. D. Bouilly, D. Perez, and L. J. Lewis, *Physical Review B*. 76, 184119 (2007).
24. A. Miotello and R. Kelly, *Applied Physics A-Materials Science & Processing*. 69, S67-S73 (1999).
25. L. J. Lewis and D. Perez, *Applied Surface Science*. 255, 5101-5106 (2009).
26. P. Lorazo, L. J. Lewis, and M. Meunier, *Physical Review Letters* 91 225502 (2003).
27. P. Lorazo, L. J. Lewis, and M. Meunier, *Physical Review B*. 73, 134108 (2006).
28. A. Miotello and R. Kelly, *Applied Physics Letters*. 67, 3535-3537 (1995).
29. D. Perez, L. K. Beland, D. Deryng, L. J. Lewis, *et al.*, *Physical Review B*. 77, 014108 (2008).
30. L. V. Zhigilei and B. J. Garrison, *Journal of Applied Physics*. 88, 1281-1298 (2000).

31. L. V. Zhigilei, P. B. S. Kodali, and B. J. Garrison, *Journal of Physical Chemistry B*. 102, 2845-2853 (1998).
32. L. V. Zhigilei, E. Leveugle, B. J. Garrison, Y. G. Yingling, *et al.*, *Chemical Reviews*. 103, 321-348 (2003).
33. M. Korolik, M. M. Suchan, M. J. Johnson, D. W. Arnold, *et al.*, *Chemical Physics Letters*. 326, 11-21 (2000).
34. G. P. Johari and O. Andersson, *Thermochimica Acta*. 461, 14-43 (2007).
35. S. Woutersen, U. Emmerichs, H. K. Nienhuys, and H. J. Bakker, *Physical Review Letters*. 81, 1106-1109 (1998).
36. C. Miheșan, M. Ziskind, B. Chazallon, C. Focsa, *et al.*, *Applied Surface Science*. 248, 238-242 (2005).
37. O. Andersson and H. Suga, *Physical Review B*. 65, 140201 (2002).
38. G. A. Slack, *Physical Review B*. 22, 3065-3071 (1980).
39. B. X. Wu, *Journal of Applied Physics*. 105, 053502 (2009).
40. K. Sokolowski-Tinten, J. Bialkowski, A. Cavalleri, D. von der Linde, *et al.*, *Physical Review Letters*. 81, 224-227 (1998).
41. C. Porneala and D. A. Willis, *Journal of Physics D: Applied Physics*. 42, 155503 (2009).
42. M. M. Martynyuk, *Combustion Explosion and Shock Waves*. 13, 178-191 (1977).
43. T. M. Orlando, A. B. Alkesandrov, and J. Herring, *Journal of Physical Chemistry B*. 107, 9370-9376 (2003).
44. K. P. Stevenson, G. A. Kimmel, Z. Dohnalek, R. S. Smith, *et al.*, *Science*. 283, 1505-1507 (1999).
45. F. Cholette, T. Zubkov, R. S. Smith, Z. Dohnalek, *et al.*, *Journal of Physical Chemistry B*. 113, 4131-4140 (2009).
46. L. C. Jacobson, W. Hujo, and V. Molinero, *Journal of Physical Chemistry B*. 113, 10298-10307 (2009).

Chapter 5: Future Experiments

The previous chapters have presented on the ablation of ASW and ASW/CO₂ thin films with pulses of 3424 cm⁻¹ radiation with nanosecond duration. The films have been several times thinner than the penetration depth of the IR photon in ASW, ~ 0.1 μm vs. ~ 0.8 μm. The MgO(100) crystal, on which the films are grown, plays a significant role in suppressing the ejection of H₂O and clusters near the surface. This chapter presents a more direct approach at undertaking studies of segregation, trivial fragmentation, phase explosions, and morphology changes that have been observed and described in this dissertation. By applying pulsed radiation with picosecond duration, the thermal pathways for heat transfer in the characteristic time scales through the host, ASW, and the substrate, MgO(100), are opened. The experimental advancements for the ablation and detection of material developed through these current studies will be expanded to investigate guest-host interactions using fast energy deposition. The experimental strategy for fast energy deposition directly to the host matrix, ASW, or indirectly, by vibrationally exciting the guest molecules, will be presented. Ablation with a high powered laser and the study of molecular transport will be the pivotal point in understanding the effect of guest molecules in the formation of aggregates and material removal through fragmentation and morphological changes.

5.1 Picosecond Energy Transfer

5.1.1 Resonant Ablation of ASW

Stimulated Raman scattering (SRS) of nanosecond (ns) length pulses has been applied throughout this dissertation for the generation of second Stokes (S_2 , 3424 cm^{-1}) radiation in a high-pressure gas cell of D_2 ($\nu = 2987 \text{ cm}^{-1}$) for the resonant ablation of ASW and its guest molecule, CO_2 . Similarly, SRS from a picosecond (ps) laser can also be an efficient method for obtaining S_2 radiation for the resonant ablation of ASW films. SRS of picosecond pulses in a gaseous medium has been reported primarily with the frequency shifting of UV laser pulses in H_2 and CH_4 , but has not been investigated to the same extent as SRS of nanosecond pulses [1-3].

The SRS from nanosecond pulses, described in Chapter 3, is referred to the steady-state condition where the laser pulse duration τ_p significantly exceeds the scattering dephasing time T_2 of the gaseous medium. T_2 is given by the Raman linewidth, $\Gamma_R = 1/(\pi T_2)$ and is proportional to the pressure of the gaseous medium at $P > 10 \text{ atm}$ [4]. The gain coefficient, α , for the steady-state is dependent on Γ_R where α is reproduced from Chapter 3 and given by

$$\alpha = \frac{\rho \cdot I_p}{\lambda_S (\lambda_S + \lambda_p) \Gamma_R} \quad (5.1)$$

where ρ represents the number density, I_p is the pump beam intensity, λ_S and λ_p are the Stokes and pump wavelengths. D_2 has a calculated linewidth of 70 MHz/atm resulting in $T_2 = 74 \text{ ps}$ for the parameters provided in Chapter 3 where the SRS of the fundamental beam from a Nd:YAG in 61.2 atm of D_2 resulted in a quantum conversion for S_2 of $\sim 4\%$.

Typically, steady-state conversion is achieved when $\tau_p > 20T_2$; otherwise it is said to be in a transient state. The transient state is characterized by the delay between the maxima of the pump and generated SRS pulses, the reduction of temporal width of the generated pulse, and the phase modulation of the propagating waves [5]. This results in broadening and deformation of the spectral shapes of the SRS pulses as well as self-focusing and optical breakdown.

Studies of first Stokes (S_1) generation of Raman scattered 1064 nm in D_2 are difficult to find [6], and no studies for the generation of S_2 were found. The threshold power for transient conditions, P_T , is assumed to be the steady-state threshold power, P_{ss} , multiplied by a factor F that is dependent on the ratio T_2 / τ_p . The steady state threshold is given by

$$P_{ss} = \frac{\lambda_s}{4\alpha} \left[1 + \left(1 + \frac{G\lambda_p}{\lambda_s \tan^{-1}(l/b)} \right)^{1/2} \right]^2 \quad (5.2)$$

where λ_s and λ_p are the wavelengths of the Stokes and pump respectively, α is the gain coefficient, G is the gain exponent needed to reach the threshold for Raman generation, b is the focusing distance in a Raman cell of length l . The ratio l/b denotes how tightly the beam is focused in the Raman cell. Hanna *et al.* calculated the threshold power for generating S_1 from scattering 1064 nm from the three most commonly used gaseous media in SRS: H_2 , D_2 , and CH_4 [6]. Further analysis and calculation of the threshold energy, E_T , given by $E_T = 1.06 \tau_p P_T$ for the generation of S_2 assuming a $\sim 1\%$ conversion, results in a threshold energy of ~ 4 mJ. For the steady state approximation with a 10 ns pulse, the calculated threshold energy is ~ 42 mJ. Experimentally, the threshold energy

in a Raman cell at $P \sim 50$ atm of D_2 was observed to be ~ 90 mJ by Malyk [7]. The values used with Equation 5.2 are summarized in Table 1. With the lower threshold energies calculated for the generation of Raman shifted light using a laser with 30 ps duration, efficient generation of S_2 seems promising. The Raman gas cell in Chapter 3 was taken to its limits to achieve $\sim 4\%$ conversion efficiency, mainly by limiting power to prevent thermal breakdown of the gas molecules and damage to the cell windows. The lower threshold calculated for S_2 and faster energy deposition into thin films of ASW open the opportunity for more efficient ablation by resonant irradiation of the host matrix.

Transient Threshold Energy Parameters	
E_T / mJ	~ 4
λ_S / m	2.92×10^{-6}
λ_p / m	1.064×10^{-6}
$\alpha / m W^{-1}$	3.7×10^{-12}
G	25
L / m	1.1
b / m	1

Table 5.1 Parameters and values used for the calculation of the threshold energy for a transient state.

5.1.2 Vibrational Excitation of Guest Molecules

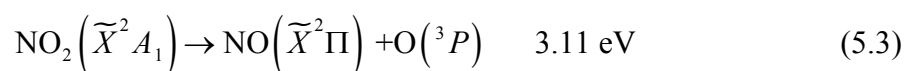
The second approach for fast energy deposition described in this chapter is the photoexcitation of guest molecules whose vibrational lifetimes decay thermally on the order of picoseconds. The energetic state of ASW has been shown in this dissertation to be influenced by whether CO_2 is trapped and by the explosive boiling of ASW together

with the ejection of protonated clusters upon irradiation. Although experimental observations have been made on the violent desorption of ASW, a thorough understanding of the mechanism for ablation and phase explosion through desorption of large fragments of ice is still a mystery.

Energy flow through heterogeneous mixtures can follow multiple pathways that make a reaction mechanism problem extremely difficult to explore. These pathways include (i) surface evaporation, where guest molecules percolate through the matrix and segregate promoting explosive behavior, (ii) substrate quenching, hence trapping any remaining guest molecules until the crystalline phase change or sublimation from the substrate, and (iii) laser ablation, where high laser fluence removes both matrix and guest molecules. We have shown that thermal conductivity, τ , in a crystalline substrate influences the study of these processes. τ is mediated primarily by phonon-phonon scattering traveling at the speed of sound in the crystalline medium. The discussion in Chapter 4 approximated that heat flow from the middle of a 100 nm ASW film to the substrate occurred at ~ 100 ps. This rapid heat transfer quenches processes occurring deeper into the film, while desorption and evaporation occur near the ASW-vacuum interphase. The quenching effect of the substrate and effective energy deposition on time-scales shorter than phonon processes can be used to monitor crystallization of ASW, desorption, and segregation dynamics of energetic amorphous mixtures by systematically inducing phase explosions in a controlled manner.

Phase explosions can be studied by further use of energetic thin films of ASW/CO₂ together with an additional molecule that can be vibrationally excited with a

pulse that is transparent to ASW or CO₂. NO₂ is a molecule that has been extensively studied in our group [8-14]. Nitrous oxides (NO_x) have atmospheric significance because they are pollutants resulting from combustion and are also generated from photodissociation under UV radiation in the troposphere, stratosphere and polar ice caps. This is, however, not a study of NO₂; rather NO₂ will be used as a source for fast energy deposition. Photodissociation of NO₂ has been reported in argon matrix isolation experiments when irradiated with $\lambda < 450$ nm [15].



However, photolysis of NO₂ was studied with a Xenon arc lamp (350 – 450 nm) over long periods of time (0.5 – 43 hrs) or with the fourth harmonic from a Nd:YAG [15, 16]. On the other hand, NO₂ has a continuous absorption at 532 nm that provides fluorescence in the red and infrared. The NO₂ molecule is electronically excited to the A²B₂ state and then relaxes to a highly vibrationally excited ground electronic state. Deak *et al.* reports that the shortest vibrational lifetime of the NO₂ stretch fundamental is ~15 ps and the longest ~ 50 ps for the O-N-O bend, in the irradiation of nitromethane with IR-Raman measurements [17]. Relaxation of the vibrational energy heats up the surrounding medium at least two times faster than the heat is removed by the substrate.

Energy deposition through relaxation of highly vibrationally excited guest molecules, such as NO₂, could initiate a phase explosion depending on the location of the bulk molecules. If gaseous CO₂ is also doped in addition to NO₂, it may promote a phase explosion by lowering the energy threshold. High concentrations of NO₂ readily form N₂O₄, shown by the equilibrium equation:



To prevent N_2O_4 formation, a low starting point for the concentration of NO_2 is suggested. FTIR spectroscopy may be used to determine the state of the NO_2 by monitoring the appearance of the asymmetric stretch of N_2O_4 at 1303 cm^{-1} [18]. The $S/N = 1$ can be achieved for absorptions as small as $\Delta I/I \sim 2 \times 10^{-5}$ where the absorption for a certain intensity, I , is given by $\Delta I/I = \sigma \rho l$ where σ is the absorption cross section, ρ is the number density, and l is the sample thickness. For a 400 ML film of ASW/ CO_2 /(2%) NO_2 that is deposited onto MgO(100) substrate at 90 K where 1 ML is $\sim 5 \times 10^{14}$ molecules cm^{-2} and the NO_2 absorption cross section is $\sigma_{\text{NO}_2} = 1.46 \times 10^{-19} \text{ cm}^2/\text{molecule}$ at 532 nm [19], the absorption results in $\Delta I/I \sim 6 \times 10^{-4}$. Hence, detection by FTIR can be achieved for low concentrations of NO_2 . Similarly, for irradiation, there are 2.7×10^{15} photons in a conservative 1 mJ/pulse, corresponding to $\sim 4 \times 10^{18}$ photons cm^{-2} . Therefore, by comparison to σ_{NO_2} it can be expected that photoexcitation with a 532 nm pulse and detection by TOF-MS will yield excellent S/N upon experimental optimization.

An increase in efficient energy deposition in the already energetic ASW/ CO_2 film, discussed in Chapter 4, can provide a better control of material removed through irradiation of heterogeneous mixtures with picosecond pulses. Irradiation with S_2 radiation allows for energy to be deposited by vibrationally exciting the host matrix, ASW. On the other hand, irradiation with 532 nm allows for the vibrational excitation of NO_2 trapped in the ASW matrix. Both methods generate heat through the relaxation of

their vibrations in times < 50 ps, whereas the high thermal conductivity of crystalline MgO(100) yields heat transfer rates > 100 ps. With this available energy, studies once reserved to thick films of ASW or unattainable high laser fluences can be explored, such as molecular transport across boundaries, coexistence of metastable phases, depth-profiling of the ice films through consecutive radiation pulses, surface/bulk diffusion, trapping and release of gas, segregation of molecules and induced phase explosions generating protonated clusters, and surface material ejection (lift-off) into the gas phase.

5.2 Experimental Strategy

The proposed experimental strategy is to generate a 3424 cm^{-1} picosecond radiation source by pumping 1064 nm light into the current stimulated Raman scattering apparatus with a 30 ps mode locked Nd:YAG laser system (Ekspla Ltd. PL2143C) already in our laboratory for direct excitation of the ASW matrix. The fundamental beam can be frequency doubled to generate 532 nm and be used for molecular excitation of $\text{NO}_2 (\tilde{X}^2 A_1)$ guest molecules in the ASW/ CO_2 film. Figure 5.1 shows a general representation of the source for generating $S_2 (3424\text{ cm}^{-1})$ radiation by SRS and the path of the 532 nm light, bypassing the Raman cell. For detailed description of the optics, refer to chapter 3 of this dissertation.

The 30 ps fundamental beam of the Ekspla is used to pump the SRS in a high pressure D_2 Raman cell. The Ekspla can produce energies of ~ 100 mJ at 1064 nm, ~ 50 mJ at 532 nm, and ~ 20 mJ at 266 nm. The resulting shifted beams are spatially

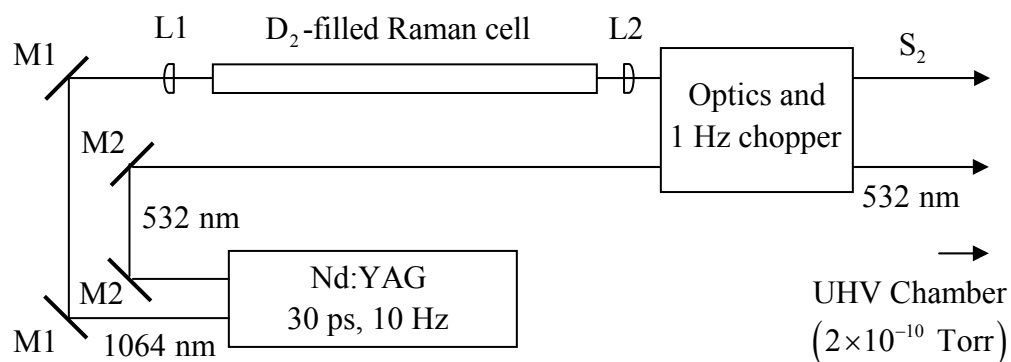


Figure 5.1 Experimental diagram of mode-locked Nd:YAG system for stimulated Raman scattering (SRS) and second harmonic generation. For complete details of the optics for SRS refer to Figure 3.3 in Chapter 3. The fundamental is guided to a high-pressure Raman cell filled with D_2 . Resulting Stokes and anti-Stokes are separated to isolate S_2 (3424 cm^{-1}) and reduce its repetition rate. Similarly, the 532 nm pulse is guided to the optical chopper and its repetition reduced. S_2 and 532 nm at 1 Hz repetition rate are guided into the UHV chamber.

separated as previously describe. The repetition rate of S_2 or 532 nm pulses is reduced to 1 Hz for single pulse desorption of ASW films. The resulting S_2 or 532 nm pulses are guided to the UHV chamber (base pressure 2×10^{-10} Torr) where the ASW film and guest molecules are grown at 90 K on MgO(100) by background vapor deposition. Ablated material is recorded and analyzed with a time-of-flight mass spectrometer (TOF-MS).

The experimental procedure outlined in Chapters 2 and 3 for the generation of nanosecond length pulses of 3424 cm^{-1} radiation by stimulated Raman scattering in a high pressure D_2 gas cell applies to this approach in the picosecond regime. There are some concepts that must be taken into account in the difference between nanosecond and picosecond SRS that will be outlined here.

Few experimental reports have been made in Raman scattering of femtosecond and less in picosecond pulses [5, 20-22]. Changes in the temporal characteristics of the

resulting beams are often observed in H₂ and CH₄. The SRS in CH₄ using 560 fs pulses established competing processes for SRS conversion and an increase in pump energy lead to self focusing and stretching of the pulse duration to 2.4 ps [23]. An increase of the spectral bandwidth has also been observed from 70 cm⁻¹ to 210 cm⁻¹ in the SRS of H₂ with femtosecond pulses of a Ti:sapphire laser [24, 25]. Additional non-linear effects observed have been multiphoton ionization and a reduced backscattering of S₁, a very common and prominent effect in nanosecond SRS.

Laser pulses that are proportionate to the time-scale for the energy transfer and transport properties of the film may open the possibility for investigations of the trivial fragmentation phenomena and molecular lift-off but also allow studies on the morphological changes and molecular transport across amorphous-crystalline phases. Figure 5.2 displays only a small fraction of studies that can be accomplished with a picosecond pulse. All of the examples shown below correspond 400 ML of ASW doped with 25% CO₂ and 2% NO₂.

Heterogeneous mixtures allow for trapped molecules to stimulate the desorption process. Films remain “thin” in the sense that both frequency pulses can penetrate further than the thickness of the film (~ 120 nm). Thermal flow occurs along the *k*-vector of the pulse and into the MgO, creating a gradient that stimulates mobility of the CO₂/NO₂ molecules. Fundamental questions pertaining to these studies are: Would the irradiation allow for guests to form aggregates and explosively desorb? At the end of the 30 ps pulse, would the substrate quench any further mobility, entrapping any remaining guests? How would this differ if instead of S₂ light was used, 532 nm ablated the film?

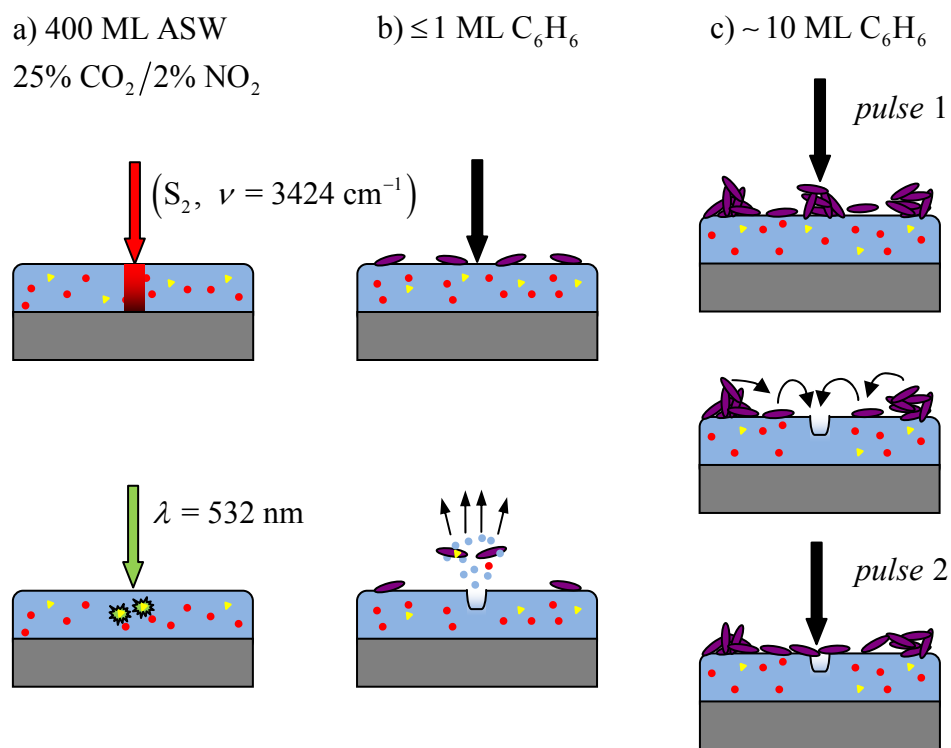


Figure 5.2 Representation of ASW doped with CO₂ (red dots) and NO₂ (yellow triangles) on a MgO(100) substrate for the study of a) fast heat transfer with picosecond pulsed laser ablation with matrix-resonant second Stokes, S₂ ($\nu = 3424 \text{ cm}^{-1}$), and guest-resonant visible (532 nm) pulses; b) segregation of guest molecules and “lift-off” of planar C₆H₆ on top of ASW film through induced phase explosions; c) depth-profiling and diffusion of C₆H₆ across the surface with consecutive pulses. Black arrows are used to denote uncertainty as to which method of ablation is best for the task.

How would the difference in distribution of radiation absorbents, H₂O vs. NO₂, affect ablation? If stacked structures are grown, e.g. MgO(100):ASW/NO₂:ASW only or MgO(100):ASW/NO₂:ASW/CO₂, would irradiation with 532 nm promote desorption originating deep into the film? There are many fundamental questions that can be asked with this system. Ultimately, the knowledge gained from this will provide a better understanding on the processes for phase explosion and the ejection of aggregates into the gas phase.

Another compelling model for the explosive boiling and its applications is to use the energy harnessed in the explosion to transfer large molecules by placing them on top of the amorphous mixture as shown in Figure 5.2b and c. Previous studies of temperature programmed desorption of C₆H₆ atop ASW or SiO₂ surfaces showed that an increase in C₆H₆ coverage tends to create islands rather than wet the surface as seen Figure 5.2b and c [26, 27]. Utilizing the impulsive power of desorbed aggregates formed during a phase explosion, molecules such as C₆H₆ or larger biomolecules may be able to experience a “lift-off” and eject into the gas phase. It is expected that coupling this process with a mass spectrometer and low energy ionization would result in an enhancement of the parent ion. By only implanting energy into the matrix, the ejected molecules will have little internal energy and less fragmentation will occur.

5.3 Conclusion

In sum, the results of this work have opened many possibilities for future studies of amorphous materials and their interactions with guest molecules. The rapid heat transfer into the crystalline MgO(100) substrate has been seen to quench processes occurring deep into the film. Energy deposition in the picosecond time-scale may enable one to trigger large scale phase explosions through direct and indirect heating of the host matrix by OH resonant irradiation or excitation of guest molecules and/or their aggregates. By improving the efficiency of energy deposition, material removal near the substrate is also enhanced. In order to gain a more fundamental understanding of these processes, a faster method for heat deposition is required, in which the time scale must be comparable to the heat transfer into the substrate.

Lower energy fluences may trigger desorption and explosive boiling. Achieving this at low fluences will allow for the irradiation of larger areas on the film where FTIR spectroscopy can be used to study the absorbed material and the morphology changes in the ASW film. Observations of clustered material with TOF-MS could give insight into the desorption mechanism for direct and indirect heating of the film. Such observations could provide a better understanding to the desorption at ~ 40 K reported in Chapter 3, but also the feature at ~ 150 K most commonly found in thick samples of ice.

The energy released through the explosive boiling of the film may be used to “lift off” larger molecules into the gas phase from the top of the film with minimal heating of their internal degrees of freedom, thereby decreasing the amount of fragmentation leading to TOF-MS studies. The projects proposed here are specific to ASW and guest

molecules CO₂ and NO₂, but a number of other heterogeneous mixtures can be used, as well as host matrices. With this, one hopes that the future generations of PhD students, who are about to embark in this exciting and daunting project, gain a deeper understanding of desorption and explosion mechanisms of not just water but metastable materials and their mixtures with the technologies implemented herein.

5.4 Chapter References

1. R. L. Carman, F. Shimizu, C. S. Wang, and Bloembergen, *Physical Review A*. 2, 60 (1970).
2. N. Morita, L. H. Lin, and T. Yajima, *Applied Physics B-Photophysics and Laser Chemistry*. 31, 63-67 (1983).
3. N. J. Everall, J. P. Partanen, J. R. M. Barr, and M. J. Shaw, *Optics Communications*. 64, 393-397 (1987).
4. C. W. Wilkerson, E. Sekreta, and J. P. Reilly, *Applied Optics*. 30, 3855-3861 (1991).
5. Y. Uesugi, Y. Mizutani, S. G. Kruglik, A. G. Shvedko, *et al.*, *Journal of Raman Spectroscopy*. 31, 339-348 (2000).
6. D. C. Hanna, D. J. Pointer, and D. J. Pratt, *Ieee Journal of Quantum Electronics*. 22, 332-336 (1986).
7. S. Malyk, *Transform and guest-host interactions in amorphous and crystalline ice*. Department of Chemistry. Los Angeles: University of Southern California (2009).
8. G. A. Brucker, S. I. Ionov, Y. Chen, and C. Wittig, *Chemical Physics Letters*. 194, 301-308 (1992).
9. S. I. Ionov, G. A. Brucker, C. Jaques, Y. Chen, *et al.*, *Abstracts of Papers of the American Chemical Society*. 204, 134 (1992).
10. I. Bezel, P. Ionov, and C. Wittig, *Journal of Chemical Physics*. 111, 9267-9279 (1999).
11. P. Ionov and C. Wittig, *Abstracts of Papers of the American Chemical Society*. 209, 262 (1995).
12. P. I. Ionov, I. Bezel, and C. Wittig, *Femtochemistry*. 143-146 (1996).
13. S. I. Ionov, H. F. Davis, K. Mikhaylichenko, L. Valachovic, *et al.*, *Journal of Chemical Physics*. 101, 4809-4818 (1994).
14. C. Wittig and S. I. Ionov, *Journal of Chemical Physics*. 100, 4714-4715 (1994).

15. D. L. Cocke, J. A. G. Gomes, J. L. Gossage, K. Y. Li, *et al.*, *Applied Spectroscopy*. 58, 528-534 (2004).
16. S. Hiraoka, K. Shibuya, and K. Obi, *Journal of Molecular Spectroscopy*. 126, 427-435 (1987).
17. J. C. Deak, L. K. Iwaki, and D. D. Diott, *Journal of Physical Chemistry A*. 103, 971-979 (1999).
18. H. Rieley, D. P. McMurray, and S. Haq, *Journal of the Chemical Society-Faraday Transactions*. 92, 933-939 (1996).
19. C. S. Dulcey, T. J. Mcgee, and T. J. Mcilrath, *Chemical Physics Letters*. 76, 80-84 (1980).
20. V. Krylov, A. Kalintsev, A. Rebane, D. Erni, *et al.*, *Generation, Amplification, and Measurement of Ultrashort Laser Pulses Iii*. 2701, 24-30 (1996).
21. V. Krylov, A. Rebane, A. Kalintsev, D. Erni, *et al.*, *Nonlinear Spectroscopy and Ultrafast Phenomena*. 2797, 8-12 (1996).
22. V. Krylov, A. Rebane, U. Wild, D. Erni, *et al.*, *Nonlinear Spectroscopy and Ultrafast Phenomena*. 2797, 2-7 (1996).
23. C. Jordan, K. A. Stankov, G. Marowsky, and E. J. Cantosaid, *Applied Physics B-Lasers and Optics*. 59, 471-473 (1994).
24. V. Krylov, A. Rebane, O. Ollikainen, D. Erni, *et al.*, *Optics Letters*. 21, 381-383 (1996).
25. V. G. Bepalov, D. I. Staselko, V. N. Krylov, A. Rebane, *et al.*, *Optics and Spectroscopy*. 82, 384-389 (1997).
26. J. D. Thrower, D. J. Burke, M. P. Collings, A. Dawes, *et al.*, *Astrophysical Journal*. 673, 1233-1239 (2008).
27. J. D. Thrower, M. P. Collings, F. J. M. Rutten, and M. R. S. McCoustra, *Journal of Chemical Physics*. 131 (2009).

Bibliography

- L. J. Allamandola, S. A. Sandford, A. G. G. M. Tielens and T. M. Herbst, *Astrophysical Journal*. 399, 134-146 (1992).
- L. J. Allamandola, S. A. Sandford and G. J. Valero, *Icarus*. 76, 225-252 (1988).
- O. Andersson and H. Suga, *Physical Review B*. 65, 140201 (2002).
- C. A. Angell, *Annual Review of Physical Chemistry*. 55, 559-583 (2004).
- C. A. Angell, *Science*. 267, 1924-1935 (1995).
- C. A. Angell, *Annual Review of Physical Chemistry*. 34, 593-630 (1983).
- P. Ayotte, R. S. Smith, K. P. Stevenson, Z. Dohnalek, *et al.*, *Journal of Geophysical Research-Planets*. 106, 33387-33392 (2001).
- R. A. Baragiola, In *Water in Confining Geometries*, V. Buch and J.P. Devlin, Eds.; Springer: Berlin (2003).
- J. A. Barker and R. O. Watts, *Chemical Physics Letters*. 3, 144-145 (1969).
- A. Bar-Nun, G. Herman, D. Laufer and M. L. Rappaport, *Icarus*. 63, 317-332 (1985).
- A. Bar-Nun, I. Kleinfeld and E. Kochavi, *Physical Review B*. 38, 7749-7754 (1988).
- S. Berkenkamp, M. Karas and F. Hillenkamp, *Proceedings of the National Academy of Sciences of the United States of America*. 93, 7003-7007 (1996).
- V. G. Bepalov, D. I. Staselko, V. N. Krylov, A. Rebane, *et al.*, *Optics and Spectroscopy*. 82, 384-389 (1997).
- I. Bezel, P. Ionov and C. Wittig, *Journal of Chemical Physics*. 111, 9267-9279 (1999).
- N. Bloembergen, *American Journal of Physics*. 35, 989 (1967).
- A. C. A. Boogert, T. L. Huard, A. M. Cook, J. E. Chiar, *et al.*, *Astrophysical Journal*. 729, 92 (2011).
- A. C. A. Boogert, K. M. Pontoppidan, C. Knez, F. Lahuis, *et al.*, *Astrophysical Journal*. 678, 985-1004 (2008).

- D. Bouilly, D. Perez and L. J. Lewis, *Physical Review B*. 76, 184119 (2007).
- N. R. Bowering, I. V. Fomenkov, D. C. Brandt, A. N. Bykanov, *et al.*, *Journal of Micro-Nanolithography Mems and Moems*. 8, 041504 (2009).
- G. A. Brucker, S. I. Ionov, Y. Chen and C. Wittig, *Chemical Physics Letters*. 194, 301-308 (1992).
- V. Buch and J. P. Devlin, In *Water in Confining Geometries*, V. Buch and J.P. Devlin, Eds.; Springer: Berlin (2003).
- V. Buch, J. P. Devlin, I. A. Monreal, B. Jagoda-Cwiklik, *et al.*, *Physical Chemistry Chemical Physics*. 11, 10245-10265 (2009).
- D. J. Burke and W. A. Brown, *Physical Chemistry Chemical Physics*. 12, 5947-5969 (2010).
- E. F. Burton and W. F. Oliver, *Proceedings Royal Society*. A153, 166-172 (1935).
- R. L. Carman, F. Shimizu, C. S. Wang and Bloembergen, *Physical Review A*. 2, 60 (1970).
- A. Cavalleri, K. Sokolowski-Tinten, J. Bialkowski, M. Schreiner, *et al.*, *Journal of Applied Physics*. 85, 3301-3309 (1999).
- Q. Chang, H. M. Cuppen and E. Herbst, *Astronomy & Astrophysics*. 458, 497-505 (2006).
- M. Chaplin. *Water Structure and Science*. 2011; Available from: <http://www.lsbu.ac.uk/water/>.
- F. Cholette, T. Zubkov, R. S. Smith, Z. Dohnalek, *et al.*, *Journal of Physical Chemistry B*. 113, 4131-4140 (2009).
- Z. P. Chu, U. N. Singh and T. D. Wilkerson, *Applied Optics*. 30, 4350-4357 (1991).
- F. Claeyssens, S. J. Henley and M. N. R. Ashfold, *Journal of Applied Physics*. 94, 2203-2211 (2003).
- D. L. Cocke, J. A. G. Gomes, J. L. Gossage, K. Y. Li, *et al.*, *Applied Spectroscopy*. 58, 528-534 (2004).
- M. P. Collings, M. A. Anderson, R. Chen, J. W. Dever, *et al.*, *Monthly Notices of the Royal Astronomical Society*. 354, 1133-1140 (2004).

- Continuum, *Operation and Maintenance Manual for the NY80 Series Laser*. Santa Clara: (1991).
- J. C. Deak, L. K. Iwaki and D. D. Diott, *Journal of Physical Chemistry A*. 103, 971-979 (1999).
- L. B. Dhendecourt, L. J. Allamandola and J. M. Greenberg, *Astronomy & Astrophysics*. 152, 130-150 (1985).
- Z. Dohnalek, R. L. Ciolli, G. A. Kimmel, K. P. Stevenson, *et al.*, *Journal of Chemical Physics*. 110, 5489-5492 (1999).
- Z. Dohnalek, G. A. Kimmel, R. L. Ciolli, K. P. Stevenson, *et al.*, *Journal of Chemical Physics*. 112, 5932-5941 (2000).
- P. Dornan, S. Alavi and T. K. Woo, *Journal of Chemical Physics*. 127, 124510 (2007).
- K. Dreisewerd, *Chemical Reviews*. 103, 395-425 (2003).
- C. S. Dulcey, T. J. Mcgee and T. J. Mcilrath, *Chemical Physics Letters*. 76, 80-84 (1980).
- P. Ehrenfreund, E. Dartois, K. Demyk and L. d'Hendecourt, *Astronomy & Astrophysics*. 339, L17-L20 (1998).
- P. Ehrenfreund, O. Kerkhof, W. A. Schutte, A. C. A. Boogert, *et al.*, *Astronomy & Astrophysics*. 350, 240-253 (1999).
- N. J. Everall, J. P. Partanen, J. R. M. Barr and M. J. Shaw, *Optics Communications*. 64, 393-397 (1987).
- N. R. Farrar, D. C. Brandt, I. V. Fomenkov, A. I. Ershov, *et al.*, *Microelectronic Engineering*. 86, 509-512 (2009).
- J. L. Finney, A. Hallbrucker, I. Kohl, A. K. Soper, *et al.*, *Physical Review Letters*. 88, 225503 (2002).
- C. Focsa, B. Chazallon and J. L. Destombes, *Surface Science*. 528, 189-195 (2003).
- C. Focsa and J. L. Destombes, *Chemical Physics Letters*. 347, 390-396 (2001).
- J. A. Ghormley, *Journal of Chemical Physics*. 46, 1321 (1967).
- N. Giovambattista, H. E. Stanley and F. Sciortino, *Physical Review E*. 72, 031510 (2005).

- S. Gogoll, E. Stenzel, M. Reichling, H. Johansen, *et al.*, *Applied Surface Science*. 96-8, 332-340 (1996).
- P. Griffiths and J. A. De Haseth, *Fourier Transform Infrared Spectrometry*. New York: John Wiley and Sons, Inc. (1986).
- M. S. Gudipati, J. P. Dworkin, X. D. F. Chillier and L. J. Allamandola, *Astrophysical Journal*. 583, 514-523 (2003).
- D. C. Hanna, D. J. Pointer and D. J. Pratt, *Ieee Journal of Quantum Electronics*. 22, 332-336 (1986).
- S. Hawkins, G. Kumi, S. Malyk, H. Reisler, *et al.*, *Chemical Physics Letters*. 404, 19-24 (2005).
- S. A. Hawkins, *Fourier transform infrared spectroscopy and temperature programmed desorption of water thin films on the MgO (100) surface*. Department of Chemistry. Los Angeles: University of Southern California (2004).
- H. Herzog, B. Eliasson and O. Kaarstad, *Scientific American*. 282, 72-79 (2000).
- S. Hiraoka, K. Shibuya and K. Obi, *Journal of Molecular Spectroscopy*. 126, 427-435 (1987).
- P. V. Hobbs, *Ice Physics*. Oxford: Claderon Press (1974).
- L. K. Hodgson, *Photodissociation, molecule-surface collision-induced dissociation and direct adsorbate photolysis of nitrous molecules*. Department of Chemistry. Los Angeles: University of Southern California (1993).
- R. Hodyss, P. V. Johnson, G. E. Orzechowska, J. D. Goguen, *et al.*, *Icarus*. 194, 836-842 (2008).
- T. Ikeda-Fukazawa, K. Fukumizu, K. Kawamura, S. Aoki, *et al.*, *Earth and Planetary Science Letters*. 229, 183-192 (2005).
- P. Ionov and C. Wittig, *Abstracts of Papers of the American Chemical Society*. 209, 262 (1995).
- P. I. Ionov, I. Bezel and C. Wittig, *Femtochemistry*. 143-146 (1996).
- S. I. Ionov, G. A. Brucker, C. Jaques, Y. Chen, *et al.*, *Abstracts of Papers of the American Chemical Society*. 204, 134 (1992).

- S. I. Ionov, H. F. Davis, K. Mikhaylichenko, L. Valachovic, *et al.*, *Journal of Chemical Physics*. 101, 4809-4818 (1994).
- D. S. Ivanov and L. V. Zhigilei, *Physical Review Letters*. 91, 105701 (2003).
- L. C. Jacobson, W. Hujo and V. Molinero, *Journal of Physical Chemistry B*. 113, 10298-10307 (2009).
- S. L. Jacques, *Proceedings of Laser-Tissue Interaction VIII*, ed. S.L. Jacques. Vol. 2975: SPIE Proceedings Series (1997).
- P. Jenniskens, S. F. Banham, D. F. Blake and M. R. S. McCoustra, *Journal of Chemical Physics*. 107, 1232-1241 (1997).
- P. Jenniskens and D. F. Blake, *Science*. 265, 753 (1994).
- G. P. Johari and O. Andersson, *Thermochimica Acta*. 461, 14-43 (2007).
- G. P. Johari, A. Hallbrucker and E. Mayer, *Nature*. 330, 552-553 (1987).
- C. Jordan, K. A. Stankov, G. Marowsky and E. J. Cantosaid, *Applied Physics B-Lasers and Optics*. 59, 471-473 (1994).
- M. Karas, *Fundamental Processes in Sputtering of Atoms and Molecules (SPUT 92)*, ed. P. Sigmund. Vol. p 623. Copenhagen: Det Kongelige Danske Videnskabernes Selskab (1993).
- M. Karas, D. Bachmann, U. Bahr and F. Hillenkamp, *International Journal of Mass Spectrometry and Ion Processes*. 78, 53-68 (1987).
- M. Karas, D. Bachmann and F. Hillenkamp, *Analytical Chemistry*. 57, 2935-2939 (1985).
- M. Karas and R. Kruger, *Chemical Reviews*. 103, 427-439 (2003).
- G. A. Kimmel, N. G. Petrik, Z. Dohnalek and B. D. Kay, *Physical Review Letters*. 95, 166102 (2005).
- G. A. Kimmel, K. P. Stevenson, Z. Dohnalek, R. S. Smith, *et al.*, *Journal of Chemical Physics*. 114, 5284 (2001).
- C. Knez, M. Moore, S. Travis, R. Ferrante, *et al.*, *Iau: Organic Matter in Space*. 4, 47-48 (2008).

- R. Knochenmuss and R. Zenobi, *Chemical Reviews*. 103, 441-452 (2003).
- W. Koechner, *Solid-State Laser Engineering*. New York: Springer (2006).
- M. Korolik, M. M. Suchan, M. J. Johnson, D. W. Arnold, *et al.*, *Chemical Physics Letters*. 326, 11-21 (2000).
- A. Krasnopolter and S. M. George, *Journal of Physical Chemistry B*. 102, 788-794 (1998).
- K. S. Krishnan, *Nature*. 122, 961-962 (1928).
- V. Krylov, A. Kalintsev, A. Rebane, D. Erni, *et al.*, *Generation, Amplification, and Measurement of Ultrashort Laser Pulses Iii*. 2701, 24-30 (1996).
- V. Krylov, A. Rebane, A. Kalintsev, D. Erni, *et al.*, *Nonlinear Spectroscopy and Ultrafast Phenomena*. 2797, 8-12 (1996).
- V. Krylov, A. Rebane, O. Ollikainen, D. Erni, *et al.*, *Optics Letters*. 21, 381-383 (1996).
- V. Krylov, A. Rebane, U. Wild, D. Erni, *et al.*, *Nonlinear Spectroscopy and Ultrafast Phenomena*. 2797, 2-7 (1996).
- G. Kumi, *Fourier transform infrared studies of guest-host interactions in ice* Department of Chemistry. Los Angeles: University of Southern California (2007).
- G. Kumi, S. Malyk, S. Hawkins, H. Reisler, *et al.*, *Journal of Physical Chemistry A*. 110, 2097-2105 (2006).
- D. Laufer, E. Kochavi and A. Barnun, *Physical Review B*. 36, 9219-9227 (1987).
- L. J. Lewis and D. Perez, *Applied Surface Science*. 255, 5101 - 5106 (2009).
- F. E. Livingston and S. M. George, *Journal of Physical Chemistry A*. 106, 5114-5119 (2002).
- F. E. Livingston and S. M. George, *Journal of Physical Chemistry A*. 105, 5155-5164 (2001).
- F. E. Livingston, J. A. Smith and S. M. George, *Journal of Physical Chemistry A*. 106, 6309-6318 (2002).
- F. E. Livingston, J. A. Smith and S. M. George, *Analytical Chemistry*. 72, 5590-5599 (2000).

- J. J. Loparo, S. T. Roberts and A. Tokmakoff, *Journal of Chemical Physics*. 125, 194521 (2006).
- P. Lorazo, L. J. Lewis and M. Meunier, *Physical Review B*. 73, 134108 (2006).
- P. Lorazo, L. J. Lewis and M. Meunier, *Physical Review Letters*. 91 225502 (2003).
- S. Malyk, *Transform and guest-host interactions in amorphous and crystalline ice*. Department of Chemistry. Los Angeles: University of Southern California (2009).
- S. Malyk, G. Kumi, H. Reisler and C. Wittig, *Journal of Physical Chemistry A*. 111, 13365-13370 (2007).
- C. Manca, C. Martin and P. Roubin, *Chemical Physics*. 300, 53-62 (2004).
- M. M. Martynyuk, *Combustion Explosion and Shock Waves*. 13, 178-191 (1977).
- M. Matsumoto, S. Saito and I. Ohmine, *Nature*. 416, 409–413 (2002).
- J. A. Mcmillan and S. C. Los, *Nature*. 206, 806 (1965).
- K. M. Menten, C. M. Walmsley, C. Henkel, T. L. Wilson, *et al.*, *Astronomy & Astrophysics*. 169, 271-280 (1986).
- C. Menzel, K. Dreisewerd, S. Berkenkamp and F. Hillenkamp, *International Journal of Mass Spectrometry*. 207, 73-96 (2001).
- C. Mihean, M. Ziskind, B. Chazallon, C. Focsa, *et al.*, *Applied Surface Science*. 248, 238-242 (2005).
- C. Mihean, M. Ziskind, B. Chazallon, E. Therssen, *et al.*, *Applied Surface Science*. 253, 1090-1094 (2006).
- T. J. Millar and D. A. Williams, *Dust and Chemistry in Astronomy*. The Graduate Series in Astronomy, ed. T.J. Millar and D.A. Williams. Bristol: Institute of Physics Publishing (1993).
- J. C. Miller and R. F. Haglund, *Laser Ablation and Desorption*. Experimental Methods in the Physical Sciences, ed. J.C. Miller and R.F. Haglund. Vol. 30: Academic Press (1998).
- A. Miotello and R. Kelly, *Applied Physics A-Materials Science & Processing*. 69, S67-S73 (1999).
- A. Miotello and R. Kelly, *Applied Physics Letters*. 67, 3535-3537 (1995).

- N. Morita, L. H. Lin and T. Yajima, *Applied Physics B-Photophysics and Laser Chemistry*. 31, 63-67 (1983).
- R. W. Nelson, R. M. Thomas and P. Williams, *Rapid Communications in Mass Spectrometry*. 4, 348-351 (1990).
- E. Nordhoff, A. Ingendoh, R. Cramer, A. Overberg, *et al.*, *Rapid Communications in Mass Spectrometry*. 6, 771-776 (1992).
- G. Natesco and A. Bar-Nun, *Icarus*. 175, 546-550 (2005).
- K. I. Oberg, E. C. Fayolle, H. M. Cuppen, E. F. van Dishoeck, *et al.*, *Astronomy & Astrophysics*. 496, 281-293 (2009).
- K. I. Oberg, R. T. Garrod, E. F. van Dishoeck and H. Linnartz, *Astronomy & Astrophysics*. 504, 891-U828 (2009).
- K. I. Oberg, H. Linnartz, R. Visser and E. F. van Dishoeck, *Astrophysical Journal*. 693, 1209-1218 (2009).
- K. I. Oberg, E. F. van Dishoeck and H. Linnartz, *Astronomy & Astrophysics*. 496, 281-293 (2009).
- K. I. R. Oberg, E. F. van Dishoeck, H. Linnartz and S. Andersson, *Astrophysical Journal*. 718, 832-840 (2010).
- T. M. Orlando, A. B. Alkesandrov and J. Herring, *Journal of Physical Chemistry B*. 107, 9370-9376 (2003).
- A. D. Papayannis, G. N. Tsirikas and A. A. Serafetinides, *Applied Physics B-Lasers and Optics*. 67, 563-568 (1998).
- Y. Park, D. Y. Kim, J. W. Lee, D. G. Huh, *et al.*, *Proceedings of the National Academy of Sciences of the United States of America*. 103, 12690-12694 (2006).
- J. B. Paul, C. P. Collier, R. J. Saykally, J. J. Scherer, *et al.*, *Journal of Physical Chemistry A*. 101, 5211-5214 (1997).
- D. Perez, L. K. Beland, D. Deryng, L. J. Lewis, *et al.*, *Physical Review B*. 77, 014108 (2008).
- D. Perez and L. J. Lewis, *Physical Review Letters*. 89, 255504 (2002).
- D. Perez, L. J. Lewis, P. Lorazo and M. Meunier, *Applied Physics Letters*. 89 (2006).

- C. R. Phipps, *Laser Ablation and its Applications*: Springer Science+Business Media LLC (2007).
- K. M. Pontoppidan, A. C. A. Boogert, H. J. Fraser, E. F. van Dishoeck, *et al.*, *Astrophysical Journal*. 678, 1005-1031 (2008).
- C. Porneala and D. A. Willis, *Journal of Physics D: Applied Physics*. 42, 155503 (2009).
- C. V. Raman, *Transactions of the Faraday Society*. 25, 0781-0791 (1929).
- K. H. Rieder, *Surface Science*. 118, 57-65 (1982).
- H. Rieley, D. P. McMurray and S. Haq, *Journal of the Chemical Society-Faraday Transactions*. 92, 933-939 (1996).
- K. Rottger, A. Endriss, J. Ihringer, S. Doyle, *et al.*, *Acta Crystallographica Section B-Structural Science*. 50, 644-648 (1994).
- N. J. Sack and R. A. Baragiola, *Physical Review B*. 48, 9973-9978 (1993).
- S. A. Sandford and L. J. Allamandola, *Journal of Astrophysics*. 355, 357-372 (1990).
- L. Schoulepnikoff and V. Mitev, *Pure and Applied Optics*. 6, 277-302 (1997).
- M. G. Seats and S. A. Rice, In *Water: A comprehensive treatise*, F. Franks, Ed.; Plenum Press: New York (1982).
- A. M. Shaw, *Astrochemistry: From Astronomy to Astrobiology*. 1st ed. Chichester: Wiley (2005).
- Sheikh, II and P. D. Townsend, *Journal of Physics E-Scientific Instruments*. 6, 1170-1170 (1973).
- J. P. Singh and S. N. Thakur, *Laser-Induced Breakdown Spectroscopy*, ed. J.P. Singh and S.N. Thakur: Elsevier B.V. (2007).
- D. A. Skoog and J. L. Leary, *Principles of Instrumental Analysis*. Fort Worth: Harcourt Brace College Publishers (1992).
- G. A. Slack, *Physical Review B*. 22, 3065-3071 (1980).
- E. D. Sloan, *Nature*. 426, 353-359 (2003).
- B. C. Smith, *Fourier Transform Infrared Spectroscopy*. Boca Raton: CRC Press (1996).

- R. S. Smith, Z. Dohnalek, G. A. Kimmel, G. Teeter, *et al.*, In *Water in Confining Geometries*, V. Buch and J.P. Devlin, Eds.; Springer: Berlin (2003).
- R. S. Smith, C. Huang, E. K. L. Wong and B. D. Kay, *Surface Science*. 367, L13-L18 (1996).
- R. Smoluchowski, *Science*. 201, 809-811 (1978).
- K. Sokolowski-Tinten, J. Bialkowski, A. Cavalleri and D. von der Linde, *Ultrafast Phenomena XI*. 63, 316-318 (1998).
- K. Sokolowski-Tinten, J. Bialkowski, A. Cavalleri, D. von der Linde, *et al.*, *Physical Review Letters*. 81, 224-227 (1998).
- K. G. Standing and W. Ens, *Methods and Mechanisms for Producing Ions from Large Molecules*. NATO ASI Series, ed. K.G. Standing and W. Ens. Vol. 269. New York: Plenum Press (1991).
- K. P. Stevenson, G. A. Kimmel, Z. Dohnalek, R. S. Smith, *et al.*, *Science*. 283, 1505-1507 (1999).
- M. M. Suchan, *Molecules-surface interactions in HCl/MgO and Water/MgO Systems*. Department of Chemistry. Los Angeles: University of Southern California (2001).
- G. Tammann, *Annalen Der Physik*. 3, 161-194 (1900).
- G. Tammann, *Annalen Der Physik*. 2, 1-31 (1900).
- C. L. Tang, *Handbook of Optics*. 3rd ed. New York: McGraw-Hill (2009).
- J. D. Thrower, D. J. Burke, M. P. Collings, A. Dawes, *et al.*, *Astrophysical Journal*. 673, 1233-1239 (2008).
- J. D. Thrower, M. P. Collings, F. J. M. Rutten and M. R. S. McCoustra, *Journal of Chemical Physics*. 131, 244711 (2009).
- A. G. G. M. Tielens, *The Physics and Chemistry of the Interstellar Medium*. 1st ed. The Graduate Series in Astronomy. Cambridge: Cambridge University Press (2001).
- A. G. G. M. Tielens, A. T. Tokunaga, T. R. Geballe and F. Baas, *Astrophysical Journal*. 381, 181-199 (1991).
- B. Toftmann, M. R. Papantonakis, R. C. Y. Auyeung, W. Kim, *et al.*, *Thin Solid Films*. 453-54, 177-181 (2004).

- R. J. Trumpler, *Publications of the Astronomical Society of the Pacific*. 42, 214-227 (1930).
- W. R. Trutna and R. L. Byer, *Applied Optics*. 19, 301-312 (1980).
- Y. Uesugi, Y. Mizutani, S. G. Kruglik, A. G. Shvedko, *et al.*, *Journal of Raman Spectroscopy*. 31, 339-348 (2000).
- E. F. van Dishoeck, *Annual Review of Astronomy & Astrophysics*. 42, 119-167 (2004).
- D. von der Linde and K. Sokolowski-Tinten, *Applied Surface Science*. 154, 1-10 (2000).
- V. Wakelam, I. W. M. Smith, E. Herbst, J. Troe, *et al.*, *Space Science Reviews*. 156, 13-72 (2010).
- J. T. Walsh, T. J. Flotte and T. F. Deutsch, *Lasers in Surgery and Medicine*. 9, 314-326 (1989).
- M. S. Westley, R. A. Baragiola, R. E. Johnson and G. A. Baratta, *Nature*. 373, 405-407 (1995).
- W. C. Wiley and I. H. McLaren, *Review of Scientific Instruments*. 26, 1150-1157 (1955).
- C. W. Wilkerson, E. Sekreta and J. P. Reilly, *Applied Optics*. 30, 3855-3861 (1991).
- J. W. Williams and A. Hollaender, *Physical Review*. 42, 0379-0385 (1932).
- C. Wittig and S. I. Ionov, *Journal of Chemical Physics*. 100, 4714-4715 (1994).
- J. Woodall, M. Agundez, A. J. Markwick-Kemper and T. J. Millar, *Astronomy & Astrophysics*. 466, 1197-U1203 (2007).
- S. Woutersen, U. Emmerichs, H. K. Nienhuys and H. J. Bakker, *Physical Review Letters*. 81, 1106-1109 (1998).
- B. X. Wu, *Journal of Applied Physics*. 105, 053502 (2009).
- J. H. Yoo, S. H. Jeong, R. Greif and R. E. Russo, *Journal of Applied Physics*. 88, 1638-1649 (2000).
- X. J. Yu and H. S. Kwok, *Journal of Applied Physics*. 93, 4407-4412 (2003).
- R. Zallen, *The Physics of Amorphous Solids*. New York: John Wiley and Sons, Inc. (1983).

- L. V. Zhigilei, *Applied Physics a-Materials Science & Processing*. 76, 339-350 (2003).
- L. V. Zhigilei and B. J. Garrison, *Journal of Applied Physics*. 88, 1281-1298 (2000).
- L. V. Zhigilei and B. J. Garrison, *Applied Physics Letters*. 74, 1341-1343 (1999).
- L. V. Zhigilei and B. J. Garrison, *Applied Physics Letters*. 71, 551-553 (1997).
- L. V. Zhigilei, P. B. S. Kodali and B. J. Garrison, *The Journal of Physical Chemistry B*. 102, 2845-2853 (1998).
- L. V. Zhigilei, E. Leveugle, B. J. Garrison, Y. G. Yingling, *et al.*, *Chemical Reviews*. 103, 321-348 (2003).
- F. M. Zimmermann and W. Ho, *Surface Science Reports*. 22, 127-247 (1995).
- F. M. Zimmermann and W. Ho, *Journal of Chemical Physics*. 100, 7700-7706 (1994).